JIMMA UNIVERSITY
JIMMA INSTITUTE OF TECHNOLOGY
SCHOOL OF GRADUATE STUDIES
FACULTY OF MECHANICAL ENGINEERING
SUSTAINABLE ENERGY ENGINEERING STREAM

NUMERICAL ANALYSIS OF HEAT TRANSFER ENHANCEMENT IN THE PARABOLIC TROUGH SOLAR COLLECTOR USING TWISTED TAPE WITH PERFORATED PLATE AND NANOFLUIDS

A Thesis Submitted to the School of Graduate Studies of Jimma University in Partial Fulfillment of the Requirements for the Degree of Master of Science in Sustainable Energy Engineering.

By

Amanuel Abye Ambelie

August 2023

Jimma, Ethiopia

JIMMA UNIVERSITY
JIMMA INSTITUTE OF TECHNOLOGY
SCHOOL OF GRADUATE STUDIES
FACULTY OF MECHANICAL ENGINEERING
SUSTAINABLE ENERGY ENGINEERING STREAM

NUMERICAL ANALYSIS OF HEAT TRANSFER ENHANCEMENT IN THE PARABOLIC TROUGH SOLAR COLLECTOR USING TWISTED TAPE WITH PERFORATED PLATE AND NANOFLUIDS

A Thesis Submitted to the School of Graduate Studies of Jimma University in Partial Fulfillment of the Requirements for the Degree of Master of Science in Sustainable Energy Engineering.

Advisor: Dr. L. Syam Sundar (Ph.D.)

Co-Advisor: Mr. Tarekegn Limore (MSc.)

August 2023

Jimma, Ethiopia

DECLARATION

I, the undersigned, declare that the thesis entitled **"Numerical Analysis of Heat Transfer Enhancement in the Parabolic Trough Solar Collector Using Twisted Tape with Perforated Plate and Nano Fluids"** is my original work and has not been presented by any other person for an award of degree in this or any other University, and all sources of materials used for the thesis have been properly acknowledged.

Amanuel Abye	_____	_____
Candidate	Signature	Date

This is to certify that the above statement made by the candidate is correct to the best of our knowledge and belief. This has been submitted for examination with our approval.

Dr. L. Syam Sundar (Ph.D.)	L. Syam Sundar	Sep. 10, 2023
Advisor	Signature	Date

Mr. Tarekegn Limore (MSc.)	_____	_____
Co-advisor	Signature	Date

The thesis has been submitted for the examination with my approval as University advisor.

APPROVAL

As members of the Examining Board of the Final MSc. Open Defence, We certify that we have read and evaluated the Thesis Prepared by: Amanuel Abye entitled: Numerical Analysis of Heat Transfer Enhancement in the PTSC using Twisted Tape Using with Perforated Plate and Nanofluids. We recommend that it be accepted as fulfilling the Thesis requirement for the Degree of Master of Science in Sustainable Energy Engineering.

Dr. L. Syam Sundar (Ph.D.)	L. Syam Sundar	Sep. 10, 2023
Advisor	Signature	Date
Mr. Tarekegne Limore (MSc.)		
Co-advisor	Signature	Date
Dr. Desta G. Tewolde (Ph.D.)	Desta G. Tewolde	Sep. 10,2023
Internal Examiner	Signature	Date
Dr. Addisu Bekele		Sep. 06, 2023
External Examiner	Signature	Date
Mr. Tarekegn Limore (MSc.)		
SEE chair	Signature	Date

The submission of the Thesis' final copy to the Council of Graduate Studies (CGS) via the Departmental Graduate Committee (DGC) of the candidate's main Department is necessary for the Thesis's final approval and acceptance.

ABSTRACT

Solar energy is the most plentiful energy source on the planet, with around 1 kilowatt per square meter (kW/m^2) of solar radiation reaching the earth's surface in clear conditions when the sun is near the zenith. This thesis's major goal is to investigate the numerical analysis of heat transfer enhancement in the PTSC employing twisted tape with perforated plates and nanofluid. The Tonatiuh ray tracing software is used to generate an optical model of the PTSC. A binary file containing the results of the ray-traced analysis is exported to MATLAB for further processing. Through surface and curve fitting to the data, the distribution of heat flux on the absorber tube's outer surface is determined. For the ANSYS Fluent Computational Fluid Dynamics (CFD) code, user-defined functions (UDFs) are made using the fitting relations. In ANSYS Fluent, the UDFs are employed for the boundary conditions and thermo-physical properties of nanofluid to solve fluid flow as well as heat transfer to the heat transfer fluid in the absorber tube. Because of their excellent thermal conductivity, water-ZrO_2 nanofluids at a concentration ratio of $(i.e. \phi = 0\%, \phi = 0.2\%, \phi = 0.6\%, and\ \phi = 1\%)$ are used in this work to enhance heat transfer. The flow inside the absorber tube was a fully developed and steady-state turbulent flow. Using CFD and k–ε RNG turbulence model with enhanced wall treatment, the hydrodynamic and heat transfer coefficients are determined using the finite volume method. The SIMPLE algorithm is used in the pressure velocity coupling approach, and a second-order upwind scheme is used for discretization. The thermal effects of using water-ZrO_2 nanofluid with different concentrations with perforated plates and twisted tape inserts are investigated. Pitch ratios (l/D) = 12.78 and 23.32 of the perforated plate (PP) and the twisted tapes (TT) with twist ratios of (y/w) = 4, 5, and 6 are inserted into the centre of the stream. The Reynolds number covered is in the range of 4000 to 10000 for the turbulent flow of ZrO_2 nanofluid in the absorber tube. The investigation demonstrates that the combination of TT and PP for the Nusselt number, friction factor, and thermal performance factor is in the range of 132.39% to 321.37%, 232.13% to 551.58%, and 1.25 to 2.256, respectively over the plain tube. The highest thermal performance factor in the order of 2.256 over a plain tube was obtained for the integrated device consisting of the TT with (y/w) = 4 and PP with (l/D) = 12.78 at a concentration of 1% water-ZrO_2 nanofluid and at a Reynolds number of 7000.

Keywords: *PTSC, Ray tracing, Heat flux distribution, Twisted tape, Twist ratio, Perforated plate, Pitch ratio, Heat transfer enhancement.*

ACKNOWLEDGMENT

First and foremost, I want to express my gratitude to Almighty God for his unwavering love and support. Being here would be impossible without his assistance and advice. I'd like to thank my adviser, Dr. L. Syam Sundar (Ph.D.), and my co-advisor Mr. Tarekegn Limore (MSc.), for their invaluable assistance, unending guidance, patience, and valuable feedback during this thesis work.

I'd like to express my sincere gratitude to Prof. Dr. A. Venkata Ramayya (Ph.D.) for his encouragement throughout the completion of this work. I am also grateful to all faculty members and staff of the Jimma Institute of Technology and the Faculty of Mechanical Engineering.

Last but not least, I want to express my gratitude to my family and friends for their unwavering support and motivation throughout my life, as well as for their critical advice and inspiration. This Master Thesis is heartily dedicated to my mother, Melkamie Ambelu, who made everything possible and impossible to see this dream come true.

TABLE OF CONTENTS

LIST OF FIGURES

LIST OF TABLES

ACRONYMS

CFD	Computational Fluid Dynamics
CSP	Concentrated Solar Power
DNI	Direct Normal Irradiation
EW	East West
HTF	Heat Transfer Fluid
LCR	Local Concentration Ratio
LFC	Linear Fresnel Collector
MCRT	Montey Carlo Ray Tracing
MWCNT	Multi-walled carbon nanotube
NREL	National Renewable Energy Laboratory
NS	North South
Nu	Nusselt Number
PP	Perforated Plate
PR	Pitch Ratio
PT	Plain Tube
PTC	Parabolic Trough Collector
PTR	Parabolic Tube Receiver
PTSCs	Parabolic Trough Solar Collector (s)
RNG	Re-Normalization Group
SPM	Single Phase Model
SWFS	Solid Work Flow Simulation
TT	Twisted Tape
UDF	User Defined Function
UDFs	User Defined Functions
3D	Three Dimensional
ZrO_2	Zirconium oxide

NOMENCLATURE

Ap	Aperture area (m^2)
Ar	Area of the receiver (m^2)
C_p	Specific heat (kJ/kg K)
C_r	Concentration ratio
d_{ci}	Glass envelope inner diameter (m)
d_{co}	Glass envelope outer diameter (m)
d_{ri}	Absorber inside diameter (m)
d_{ro}	Absorber outside diameter (m)
F	Focal length (m)
f	Friction factor
h	Convection heat transfer coefficient (W/m^2 K)
k	Thermal conductivity (W/m K)
K	Incident angle modifier
L	Collector length (m)
p	Pitch length (m)
$\dot{m}$	Mass flow rate (kg/s)
Pr	Prandtl number
q''	Heat flux (W/m^2)
Re	Reynolds Number
T_{in}	Inlet fluid temperature (K)
Tr	Twist ratio
u_{in}	Fluid inlet velocity (m/s)
w_a	Aperture width (m)

GREEK LETTERS

α	Receiver absorptance
ε_c	The emissivity of the glass envelope
ε_r	The emissivity of the absorber tube
τ	Glass cover transmittance
ρ_c	Mirror reflectance
ρ	Density (kg/m^3)
η	Thermal performance
μ	Dynamic viscosity (mPa.s)
I	Turbulence intensity
I_b	Direct solar beam radiation
θ_z	Zenith angle (^{o})
φ	The circumferential angle of the receiver (^{o})
ϕ	The concentration ratio of water-ZrO_2 nanofluid

SUBSCRIPTS

f	Base fluid
in	Inlet
out	Outlet
p	Plain Tube
p	Nanoparticle

CHAPTER 1

INTRODUCTION

1.1 Background

Solar energy is the most plentiful source of energy on the planet, with around 1 kilowatt per square meter (kW/m^2) of solar radiation reaching the earth's surface in clear conditions when the sun is near the zenith. Solar energy consists of two types of radiation: a beam or direct radiation that comes directly from the sun and diffuse radiation that travels to the earth after being dispersed by the atmosphere in all directions [1].

The energy at temperatures greater than those attained by incident solar radiation on the earth's surface is required for many contemporary purposes. To attain high temperatures, solar energy is focused on collectors, which gather and concentrate solar radiation onto a smaller receiving surface. The two main categories of solar energy converters are solar PV panels and solar thermal collectors. Solar thermal collectors immediately convert the sun's rays into useful heat, in contrast to PV panels, which transform solar energy into electricity. The heat produced by the collector after the sun's beams have been converted to it may be applied to many industrial processes [1, 2]. Concentrated solar power (CSP) is one of the most promising clean energy technologies for lowering the environmental impact of electricity generation. In CSP systems, collectors are used to focus sunlight on a specific region. The production of electricity and heat may then be conducted using this concentrated energy. Linear Fresnel collector (LFC), Parabolic dish (PD), parabolic trough collector (PTC) and central tower (CT) are four distinct, reasonably advanced CSP devices. The parabolic dish and the central tower are point-focus systems, while linear Fresnel and the parabolic trough collectors are line-focus systems [2–4].

The Parabolic Trough Collector (PTC) represents one of these four systems that are the most developed and sophisticated in terms of CSP technology. It comprises a circular cylinder receiver and a parabolic cross-sectional cylindrical concentrator that is situated parallel to the parabola's focus line. Direct sun energy is reflected onto a receiving tube by the parabola's focal line. The receiving tube's outer surface, which focuses on direct solar radiation, is smaller than the collecting aperture area. In its linear focus receiver, the parabolic trough concentrator (PTC) transforms solar energy into thermal energy. All focus points at each cross-sectional position of the concentrator

are combined to form the focal line, which is where the beam radiation is reflected. To increase its absorptivity, the receiver tube is selectively coated [1, 3, 4].

To mitigate potential convective heat losses, it is often housed inside a glass tube. To continuously maintain the trough aperture towards the sun, the trough assembly follows the sun along a single axis. The focal axis of the trough is often positioned parallel to either the east-west direction or the north-south direction [1, 3].

In this work, a combination of turbulator insertion with nanofluid has been studied. Therefore, the utilization of the insertion of twisted tapes and a perforated plate in different twist arrangements and pitch ratios is proposed as an enhancement method in this work. Numerical analyses were conducted to investigate the heat transfer enhancement using water-ZrO_2 nanofluid in a twisted tape and a perforated plate inserted in a tube with circumferentially non-uniform heat flux.

1.1.1 Ethiopia's energy potential

Significant energy-generated resources are available in Ethiopia, mostly in the form of hydroelectric power, wind, geothermal, biomass, and solar energy. Nonrenewable energy resources, particularly natural gas, and coal are abundant in the country. While traditional biomass consumption presently dominates the energy industry, other sources of energy such as hydropower and the remainder of the renewable energy sources have the potential to provide the country with significant economic growth opportunities [4, 5].

1.1.2 The potential of solar energy

Solar power is non-polluting, limitless, as well as risk-free. It produces no hazardous emissions even when converted to electricity using solar or thermodynamic facilities. As a consequence, renewable energy sources have become increasingly important in the development of energy policy. Several countries have implemented inducement programs to encourage energy production and grid interconnection while minimizing environmental impact [6, 7].

Ethiopia has an abundance of solar energy potential. However, about 1% of this potential has been achieved thus far. According to recent data compiled by the energy system management and development follow-up core process, solar photovoltaic energy has generated more than 35 MWh in the last 6 years, which is more than 6MW greater than the installed capacity. Government and non-governmental groups have erected solar thermal water heaters with a total energy production

of 299 MWh and ten water pumps with a pumping installed capacity of 10 kW in various sections of the country [2, 5].

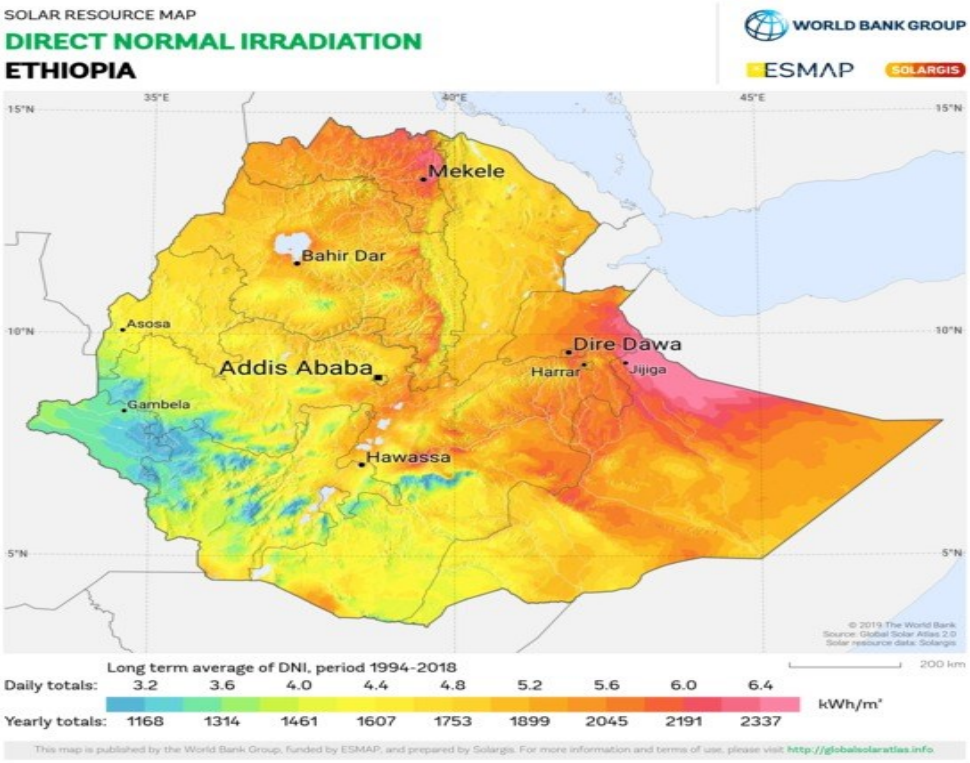

Figure 1.1: Direct normal irradiation (https://solargis.com/maps-and-gisdata/download/Ethiopia).

Ethiopia is one of the countries near the equator where greater sun radiation abounds, resulting in good conditions for solar energy utilization. As a result, parabolic solar trough power generation systems may become an option for power generation in the country [5, 7].

1.2 PTSC components

The parabolic trough, absorber/receiver tube, working fluid, and glass cover are the four essential parts of a parabolic trough collector.

1.2.1 The parabolic trough

To focus the incoming sunlight on the parabolic mirror's focal line, where the absorber tube is situated, sheet metal is bent into a parabola form. Typically, the parabolic mirror's surface reflectivity exceeds 0.9. The parabolic trough is defined by three factors. These are the aperture width, length of the trough, and focal length of the reflector surface. The parabolic trough is

supported by a sturdy framework. The construction uses a one-axis tracker to follow the Sun. It has been discovered that a PTSC should be oriented North-South (NS) with sun tracking in the East-West direction for the greatest effectiveness [8]. Larger mirrors can produce higher temperatures. On the other side, greater wind load and vibration are produced by the bigger parabolic mirror surface area. Therefore, to accommodate the growing wind stress, larger mirrors need stronger frames.

A PTSC power plant's parabolic mirrors may also cast shadows on one another. As a result, the space between them needs to be set up appropriately. Figure 1.2 provides a photo of the Noor 1 CSP plant to illustrate the significance of the PTSC line spacing.

Figure 1.2: The power plant for Noor CSP [9].

1.2.2 The absorber tube

At the parabolic mirror's focal line, an absorber tube is positioned. Stainless steel is frequently used as the tube material. On the tubes outside, a selective coating with low emissivity and high absorptivity is applied. Figure 1.3 displays the absorber tube with a glass cover.

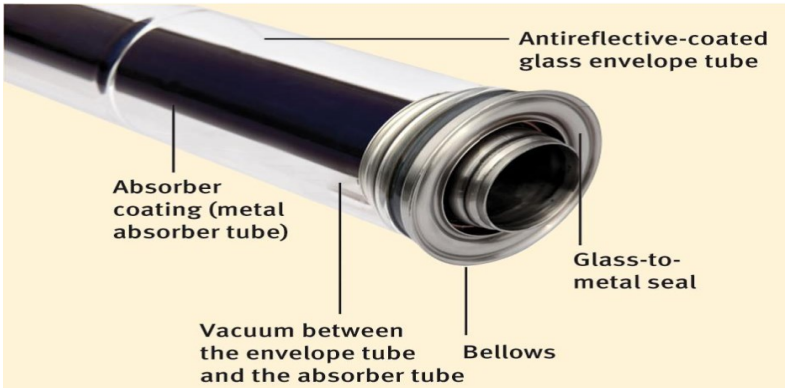

Figure 1.3: The absorber tube with the glass cover [10].

1.2.3 The glass cover

The glass cover reduces heat losses from the absorber tube through convection and long-wavelength radiation. To reduce heat loss from natural convection, the area between the glass cover and the absorber tube is vacuumed. In the visible and UV spectra, the glass cover has a very high transmissivity rating of 0.96 on average. By producing a greenhouse effect, it selectively reflects part of the infrared light that the absorber tube emits [3].

1.2.4 The working fluid

A mixture of liquids (water, ethylene glycol, propylene glycol, or oil) and particles is known as a nanofluid. These solids are nanometer-sized (less than 100 nm) particles, such as metallic (Ag, Au, and Cu) metallic oxides (TiO2, SiO2, CuO, Al2O3, ZrO2), or carbon (diamond, graphite, CNT, fullerene, graphene). A liquid might consist of many fluids or be made up of just one basic fluid. With or without the use of dispersants, the resultant mixture produces a suspension of colloidal particles under stable circumstances. The composition of ZrO2 nanofluids of various sizes is shown in Figure 1.4 [11].

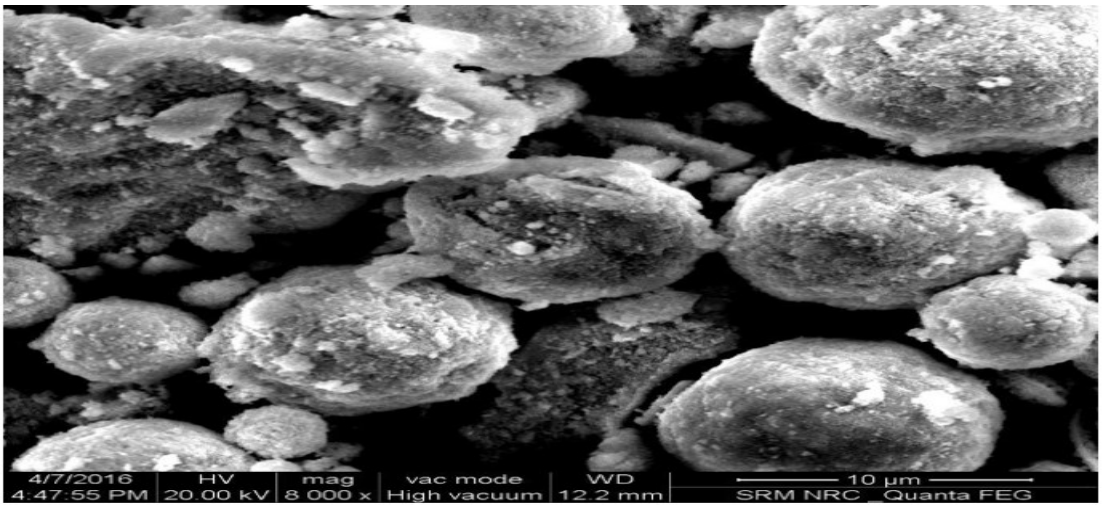

Figure 1.4: The configuration of ZrO_2 nanofluids with different dimensions [12].

1.2.4.1 Application of Nanofluids in Solar Energy

One of the most significant components of solar conductors is the working fluid, which plays a key role in PTSC heat transmission. Since the commencement of solar energy use, there have been several attempts to improve the thermal conductivity of the working fluid. The research on the use of nanofluids in PTSC may be classified in several ways. The first categorization may be built on the numerous different types of nanoparticles used in research [13].

The nanoparticles are divided into two categories:

1. Metallic nanoparticles like Au, Al, Zn, Cu, and Fe.
2. Non-metallic nanoparticles such as CeO_2, ZnO, TiO_2, Fe_2O_3, SiO_2, carbon nanotubes (CNT), and multiwall carbon nanotubes (MWCNT).

In Figure 1.5, it is apparent that Al_2O_3 is the most widely used nanoparticle among researchers, accounting for 41% of studies. Other commonly used nanoparticles include CuO, TiO2, and others. At various volumetric concentrations ranging from 0.01-6% or weight percentages ranging from 0.1-20 wt%, both metallic and non-metallic nanoparticles may be disseminated into the base fluid [13].

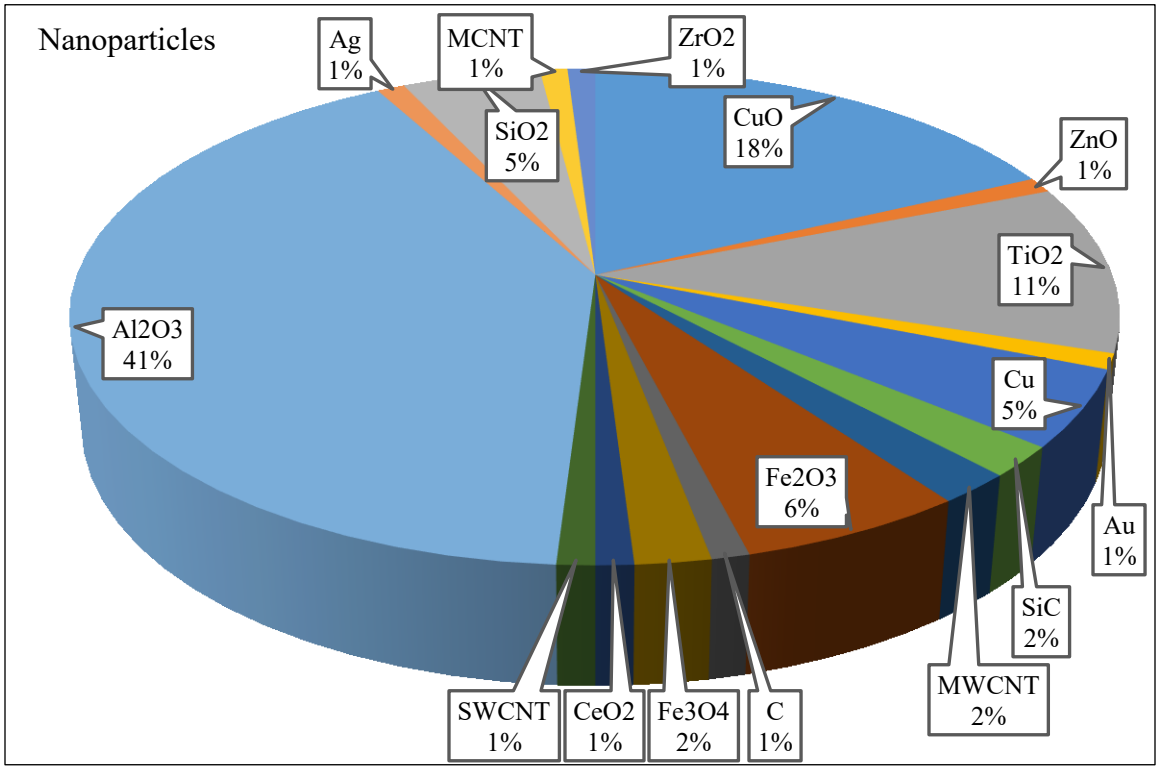

Figure 1.5: Various nanoparticles have been used in investigations on PTSC augmentation utilizing nanofluids [13].

Another way to understand nanofluids is to explore the various base fluids in which the nanoparticles are distributed. So far, four major kinds of base fluid have been used:

1. Ethylene glycol (EG)
2. Water
3. Molten salts (such as 60% $NaNO_3$–40% KNO_3)
4. Oils (such as Therminol-VP-1, Thermal oils, Dowtherm-A, Synthetic oils, etc.)

1.3 Statement of the problem

Energy consumption in Ethiopia rises in lockstep with the country's gross domestic GDP. Increased usage of publicly available solar energy resources is one possible means of overcoming the energy problem [14]. Ethiopia has plenty of sunshine all year thanks to its proximity to the equator. In Ethiopia, the yearly average daily radiation hitting the ground is around 5.2 kWh/m^2 /day. The yearly average radiation statistics for the country are expected to be 4.5 kWh/m^2/day in July and 5.55 kWh/m^2/day in February and March [15]. Because of the wide range of applications of PTSCs, enhancing their performance is a key priority for researchers all around the world. To improve the thermal performance of PTSCs, researchers have used innovative designs, corrugated channels, turbulators, and nanofluids. As a result, this paper presents using twisted tape with a perforated plate and water-ZrO_2 nanofluid as a heat transfer fluid to improve heat transfer performance in the absorber tube. Because of their excellent thermal conductivity, nanofluids as absorber fluids are a useful way to improve heat transfer in solar applications.

1.4 Objectives of the study

1.4.1 General objective

The main objective of this work is to study the numerical analysis of heat transfer enhancement in the PTSC using twisted tape with perforated plates and nanofluids.

1.4.2 Specific objectives

The following specific objectives are performed to achieve the general objective of this work:

- To model the PTSC geometry using Tonatiuh software for preparing the Monte Carlo Ray Tracing method (MCRT).
- To analyze the heat flux distribution around the absorber tube and simulate the performance of the absorber tube using ANSYS Fluent software.
- To optimize the heat transfer enhancement in the absorber tube using twisted tape with a perforated plate insert and ZrO_2 nanofluids at different concentration ratios.
- To validate this work with another work from the literature.

1.5 Significance of the study

One of the most pressing challenges in the country is energy. The country has a high need for energy, and the government relies on a variety of energy sources to supply this demand. This study increased heat transmission in the absorber tube by utilizing the system's turbulators as well as the nanofluid. The study's findings examine solar energy as an ecologically beneficial option for power generation and large-scale water heating, and it is a step toward reducing dependency on foreign fuels. The study benefits a variety of sectors by lowering costs associated with gasoline and other high-cost energy sources. This, in turn, generates energy possibilities for both industry and the country.

1.6 Scope of the study

This study's numerical simulation relies on the meteorological data of the Ethiopian solar source, in the Somalia region. This study focuses on the enhancement of heat transfer in the parabolic trough solar collector employing twisted tape with perforated plates inserted in addition to water-ZrO_2 nanofluids. ANSYS FLUENT 19.2 is used to analyze the CFD simulation for the internal flow of fluid in PTSC. The nanofluid of water-ZrO_2 at four concentrations ratio $(\text{i. e. } \phi = 0\%, \phi = 0.2\%, \phi = 0.6\%, \text{and } \phi = 1\%)$ will be selected and their performances are compared with each other.

CHAPTER 2

LITERATURE REVIEW

2.1 Review the performance of a parabolic trough solar collector

The modelling and simulation of the PTSC technology have been developed and executed by several researchers. Hong et al. [16] investigated the thermal and flow characteristics of a parabolic trough solar collector. The heat transfer fluid chosen was Cu-water nanofluid. The Nusselt number increased as Cu nanoparticle concentration rose (Nu). Additionally, the impact of Cu nanoparticle addition on heat transfer enhancement increased significantly as the Reynolds number dropped. The function of forced convection superseded that of conduction as the Reynolds number grew. Furthermore, it was shown that the thermal efficiency is improved while using Cu nanoparticles, also the pressure drop increased marginally. The impact of changes in direct beam irradiation on the performance of solar collectors was investigated. Nu rose by up to 8.6 %, 9.78 %, and 11.43 % when normal direct radiation increased from 900 to 1100 W/m^2 at Reynolds numbers of 10^4, 10^5, and 10^6, respectively, leading to improvements in thermal efficiency of 3.87 %, 3.82 %, and 2.04 %. In Ghasemi and Ranjbar [17] Al_2O_3-water and CuO-water nanofluids are employed in the research. Using a finite volume approach, CFD is employed to determine hydro dynamically and heat transport coefficients. For varied heat flux circumstances, this analysis is done using the k–RNG turbulence model. The performance of parabolic troughs in terms of heat transfer and hydrodynamics is addressed to the volume fraction (ϕ) of nanofluids. Nanofluids enhance the heat transfer capabilities of parabolic trough collectors as compared to pure water. For both nanofluids, the average friction factor and Nusselt number rise as the volume proportion of nanoparticles increases. Furthermore, adding Al_2O_3 and CuO water nanoparticles (at a concentration of 3% each) improves heat transmission by 28% and 35%, respectively.

Ekiciler et al. [18] investigated the 3D heat transfer in the turbulent flow and flow characteristics of hybrid nanofluids in a PTSC. Working fluids include Ag–MgO/Syltherm 800, Ag TiO_2/Syltherm 800, and Ag–ZnO/Syltherm 800 hybrid nanofluids with volume fractions of nanoparticles of 1%, 2%, 3%, and 4%. Thermal efficiency, a key feature of PTC, increases as the volume fraction of nanoparticles increases and decreases as the Reynolds number increases. An

Ag-MgO/Syltherm 800 hybrid nanofluid with a volume percentage of 4.0% nanoparticles is the most effective working fluid for the PTSC receiver.

Okonkwo et al. [19] improved the effectiveness of the operation of the readily accessible LS-2 solar collector by raising the coefficient of convective heat transfer inside the absorber tube. Al_2O_3, Fe_3O_4, and CuO nanoparticles were tested in pressurized water, supercritical CO_2, Therminol VP-1, and Therminol VP-1 with CuO, Al_2O_3, and Fe_3O_4 nanoparticles in pressurized water, Therminol VP-1, supercritical CO_2, and Therminol VP-1 with Al_2O_3, Fe_3O_4, and CuO nanoparticles in pressurized water. The effect of a converging-diverging tube with sine geometry is also examined since this geometry increases the receiver's turbulent flow and heat transfer surface.

Subramani et al. [20] studied the addition of a TiO_2/DI-H_2O (De-Ionized water) nanofluid to a parabolic trough solar collector to improve its efficiency (PTSC). Under turbulent flow regimes, test samples containing nanofluids at concentrations of 0.05 %, 0.1 %, 0.2 %, and 0.5% were compared to deionized water (the basis fluid) at various flow rates ($2950 \leq Re \leq 8142$). When TiO_2 nanofluids were used instead of the base fluid, the convective heat transfer coefficient increased by 22.76 %. The volume concentration of 0.2 % TiO_2 nanofluid (0.0667 kg/s of mass flow rate) provided the greatest efficiency increase in the PTSC by 8.66 % higher than the water-based collector. As a consequence, it was determined that the energy absorbed parameter was 9.5 % greater than the basic fluid.

Sokhansefat et al. [21] Investigated the impact of the concentration of Al_2O_3 particles in synthetic oil on the heat transfer rate from the absorber tube and was also examined. At operational temperatures of 300 K, 400 K, and 500 K, different nanoparticle concentrations (0.5% in volume) were utilized in this study.

According to Siavashi et al. [22], increasing the volume percentage of Cu nanoparticles to 0.015 enhances thermal efficiency, with a 12% rise in Nu and a 1.2% increase in the scenario with $Gr = 10^7$. In addition, Nu and f are up to 10.6 and 5 times greater for collectors with receiver tubes half-porous, than for collectors with receiver tubes non-porous respectively. Furthermore, for whole-porous receiver tubes, these ratios are generally enhanced to 25 and 30, respectively. As a result, the use of porous receiver tubes has a major impact on the performance of PTCs.

Alnaqi et al. [23] conducted a study using two twisted tapes to assess the numerical impact and thermal-hydraulic performance of parabolic trough solar collectors (PTSCs). The coolant employed was a hybrid nanofluid consisting of MgO-MWCNT (80%:20%) and thermal oil. They

employed a two-phase model for their numerical analysis. The study investigated the parameters of geometrical effects, Reynolds numbers (Re), twisted tape width and rotation direction, and nanoparticle volume percentage on the hydrothermal characteristics of the PTSC. The LCRW model, with a turbulator diameter of 15 mm and filled with nanofluid at a specified nanoparticle level, was examined. A volume fraction of 2% for Re < 30,873, was recommended as the optimal PTSC, whereas for Re > 30,873, the LWRC model with a 15 mm diameter of turbulators filled with a volume fraction of 2% nanoparticle of nanofluid was suggested.

Bellos et al. [24] are currently investigating two primary strategies in their research: the utilization of nanofluids as working fluids and the implementation of flow turbulators, specifically inserts, internal fins, or tube dimples. The objective of their study is to offer a comprehensive overview of previous research conducted on this subject matter, along with a numerical assessment of the most commonly employed thermal enhancement algorithms. Specifically, they compare the performance of 6% CuO oil-based nanofluids to that of internal rectangular fins in the absorber, as well as the combined utilization of both approaches. The analysis is conducted using a validated CFD model within SolidWorks Flow Simulation, considering various temperature ranges of the fluid. Based on the final findings, the use of nanofluids enhances thermal efficiency by 0.76%, internal fins improve it by 1.10%, and the combination of these approaches results in a 1.54% improvement.

Bellos et al. [25] conducted a systematic investigation to determine whether centrally positioned or eccentrically positioned inserts result in greater thermal enhancement. They employed a computational fluid dynamics (CFD) model within SolidWorks Flow Simulation for validation of their study. The research also involved evaluating the increase in usable heat output and the demand for pumping work, using exergy and overall efficiency parameters. The study considered different scenarios of working fluid using Syltherm 800, a flow rate of 100 L/min, and an intake temperature of 600 K. Additionally, the inlet temperature was varied from 450 to 650 K, and the diameter of the inserts was explored up to 50 mm.

Reddy and Satya Narayana [26] focused on investigating the turbulent flow and heat transfer capabilities of Therminol oil VP-1 using a three-dimensional (3D) parabolic trough solar collector (PTSC) equipped with a porous finned receiver featuring circular, trapezoidal, triangular, and square corrugations. They utilized the CFD software ANSYS Fluent and employed the k-RNG model with the standard wall function approach. The performance of the PTSC was evaluated

using a Single-Phase-Model (SPM) under varying solar irradiation, flow velocities, and heat loss conditions. Their findings indicated that the inclusion of trapezoidal porous inserts in the absorber tube of the solar trough receiver increased the Nusselt number by up to 13.80% at a mass flow rate of 6.41 kg/s while experiencing a pressure loss of only 1.7 kPa [27].

Reddy et al. [28] statistically examined a square-shaped porous finned receiver and a (3D) PTSC in turbulent flow and heat transfer using Therminol oil VP-1. The performance of PTSCs was evaluated using geometrical characteristics, concentration ratios, and flow rates. The Nusselt number was increased by 17.5 % due to the square porous inserts in the PTSC's absorber tube while creating a pressure decrease of 2.0 kPa.

In a study by Soo Too and Benito [29], the effect of utilizing porous foam, dimpled tube, twisted tape insert, and helical coil/wire insert in a PTSC filled with diverse operational flows was evaluated analytically. They found that tubes with deeper protrusions on the interior surface have a higher PEC than plain tubes and tubes that have undergone various modification processes.

Bellos et al. [30] investigate numerical heat transfer enhancement of PTSCs fitted with converging-diverging absorber tubes employing Solid Works Flow Simulation (SWFS) software. To find the most efficient model, they looked at energy and exergy efficiencies. According to their findings, the energy efficiency of PTSC is increased by roughly 4.6 % using a converging-diverging absorber tube.

Bellos et al. [31] Investigated the multi-criteria assessment of internally finned absorber tubes in the PTSC. Internal longitudinal rectangular fins were produced in the evacuated tube of the PTSC under study. This project's main objective was to look at how fins affected the PTSC's hydrothermal performance. They found that, as compared to the smooth scenario, the best model's use of fins boosts the collector's thermal efficiency by 0.82%.

Ahmed and Natarajan [32] Investigated a PTSC with internal toroidal rings, and the heat transfer improvement under the fully developed turbulent fluid flow was numerically studied. To model the setup, they employed the turbulence model realizable k-ε model with improved wall treatment. They found that the average Nusselt number could be improved by 3.7% and the energy efficiency could be raised by 2.3% when the toroidal rings inside the receiver tube were used.

Shaker et al. [33] Investigated, the thermal effects of innovative flange-shaped turbulators employing a nanofluid of Al_2O_3-Syltherm oil with varying concentrations are examined to enhance the performance of a linear parabolic collector. For the simulation, ANSYS-FLUENT-18.2

commercial software with turbulence model of realizable $k - \varepsilon$ two-equation was used. According to the findings, it was discovered that raising the nanoparticle's volume percentage (to 5%) and the quantity of fluid's heat transfer coefficient (h) increase as the turbulators leads to an increase, which in turn results in the creation of a uniform temperature in the absorber. For instance, the turbulators increasing from 10 to 15 sets raises the value of h by around 8.5% at an input temperature of 350 K and a flow rate of 4.5 kg/s. On the other hand, the findings show that by rearranging the turbulators, the collector's ability to transmit heat can be improved by 1% for an input temperature of 550 K, 3.5% for 450 K, and 5% for 350 K.

Figure 2.1: The linear parabolic collector geometry [33].

Eiamsa-ard et al. [34] conducted a study to examine the effects of twisted tape (TT) swirl generators and circular-ring turbulators (CRT) on heat transmission, thermal performance factors, and pressure drop characteristics in a round tube. In the heated part of the tube, they employed both CRT and TT. Three twist ratios of the TT (y/w = 3, 4, and 5) and three pitch ratios of CRT (l/D = 1.0, 1.5, and 2.0) were studied. The working fluid for the experiment was air, and uniform wall heat flux conditions were maintained with Reynolds numbers ranging from 6000 to 20000. According to the experimental results, the combined TT and CRT exhibited significantly higher thermal performance factor, friction factor, and heat transfer rate compared to using CRT alone. Across the considered range, the tubes incorporating both devices showed a mean thermal performance, Nusselt number, and friction factor that were 6.3%, 25.8%, and 82.8% higher than those of tubes using CRTs alone respectively. The device with the combined l/D of 1.0 for the CRT and 3.0 for the TT has the maximum thermal performance factor (1.42).

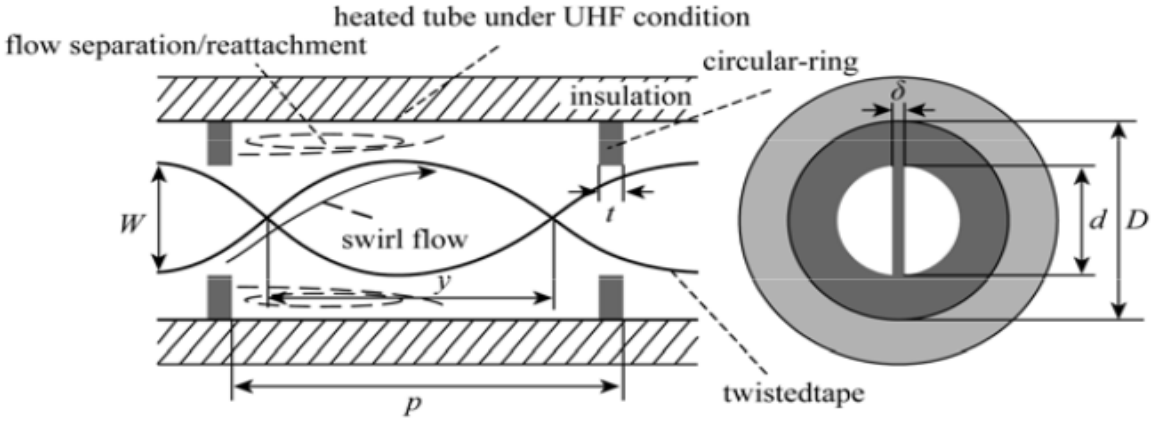

Figure 2.2: Diagram of a tube with enhancement devices [34].

He et al. [35] Conducted a study in which they examined the flow and heat transfer of CuO-water nanofluid in a tube using both single-phase and two-phase (mixed) models. The simulations were performed in the turbulent flow regime at various Reynolds numbers ranging from 3000 to 36,000. The researchers analyzed the impact of employing CuO-water nanofluid on the Nusselt number, friction factor, and performance assessment criterion. They found that the two-phase mixture model provided more accurate results compared to the single-phase model. The study revealed that a tube with a single twisted tape achieved a maximum performance efficiency coefficient of 2.18 when using the two-phase model with a Reynolds number of 36,000 and a solid concentration of 4%. However, when using two twisted tapes under the same conditions, the tube achieved a slightly lower maximum performance efficiency coefficient of 2.04. Therefore, from the perspective of thermal-fluid dynamics, the usage of one twisted tape is preferable.

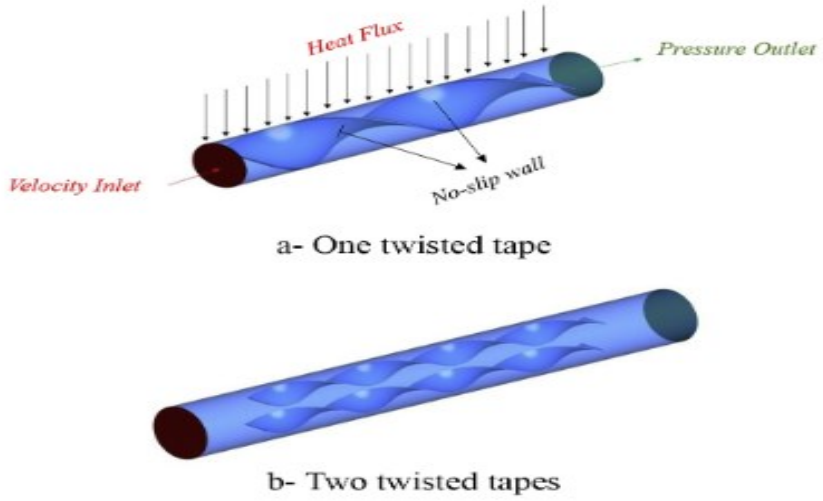

Figure 2.3: a), One twisted tape b), Two twisted tapes of boundary conditions [35].

Table 2.1: An overview of the literature on the use of turbulators to improve the performance of PTSC.

Ref.	Title	Geometry	Method	Study outcomes
[36]	Impact of different configurations of porous disc receivers on the performance of solar parabolic trough concentrators.	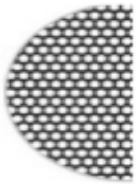	CFD	In comparison to a tubular receiver operating at a mass flow rate of 0.5 kg/s, the heat transfer rate of a porous disc receiver showed an increase of 221 W/m and 13.5%. Additionally, for water and Therminol oil-55, the heat transfer rate increased by 575 W/m and 31.4% with a pumping penalty of 0.074 W/m.
[37]	Improving heat transfer in air-filled tubular absorbers for concentrated solar thermal applications.		Model	This study revealed that tubes with deeper protrusions on their inner walls outperform plain tubes and tubes with various enhancement methods in terms of overall heat transfer and pressure drop.
[38]	Investigating entropy generation and heat transfer in a PTR utilizing wall-detached twisted tape inserts.		CFD	The findings demonstrate a significant improvement in heat transfer performance of approximately 169% compared to a receiver with a plain absorber tube. Additionally, there was a reduction in the absorber tube circumferential temperature differential by up to 68% and a 10% increase in thermal efficiency. As the twist ratio increases and the width ratio decreases, the ideal Reynolds number also increases. The study observed the highest decrease in entropy generation rate, which was approximately 58%.

[39]	A numerical investigation of the thermal impact of porous rings on the performance of parabolic trough collectors.	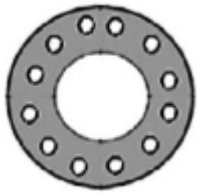	CFD	The results suggest that putting porous rings into an absorber tube improves the heat transfer properties of solar parabolic trough collectors. The heat transfer characteristic rises as the distance between porous rings decreases, whereas the Nusselt number decreases as the porous rings of the inner diameter increase.
[31]	Evaluating parabolic trough collectors with internally finned absorbers using multiple criteria.	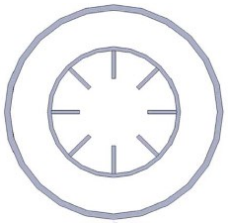	SolidWorks Flow Simulation	In general, increasing the length and thickness of the rings leads to higher thermal enhancement but also increases pressure losses. The enhancement of thermal efficiency, represented by the Nusselt number, concerning the increase in pressure drop or friction factor, is evaluated using various methods.
[40]	Modification of mesoporous silica with copper nanoparticles for the development of hybrid nanofluids.	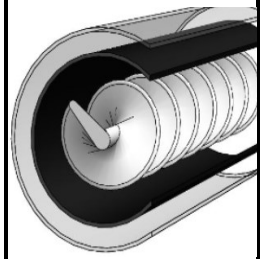	CFD	The application of the turbulators to the investigated PTSC was shown to have a considerable impact on the improvement of energy efficiency. In various Reynolds numbers, adding nanoparticles increased the average Nusselt number inside the receiver tube. It was also discovered that increasing nanoparticle volume concentrations improves heat transmission regularly.

[41]	Investigation of the thermal and hydraulic performance, as well as the economic viability, of a PTSC filled with an oil-based hybrid nanofluid and equipped with a finned rod turbulator.	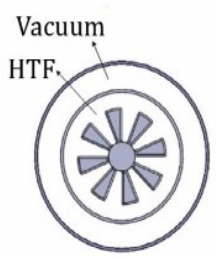	CFD	The results indicate that using a finned rod turbulator is effective for Reynolds numbers (Re) below 12,000, but it should not be employed for higher Re values as it negatively impacts the overall hydrothermal performance of the parabolic trough solar collector (PTSC). Furthermore, the new shape can save 14% on material utilization, according to the economic study.
[42]	Enhancement of heat transfer in the receiver's tube of a parabolic trough solar collector through the use of hybrid nanofluids and conical turbulators.	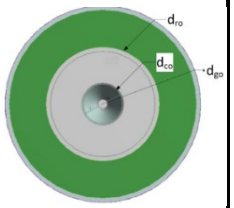	CFD	Replacing pure Syltherm oil with Ag-SWCNT/Syltherm oil and incorporating conical turbulators resulted in a 233.4% increase in thermal performance. The evaluated performance criteria ranged from 0.91 to 82. Thermodynamic efficiency improved by 11.5%, while energy efficiency improved by 18.2%. The entropy generation rate saw a significant reduction of 42.7%, and the ratio decreased by 33.7%.
[43]	Numerical examination of the impact of curved turbulators on the exergy efficiency of solar collectors incorporating two-phase hybrid nanofluids.	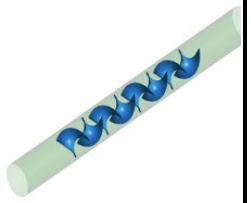	CFD	The findings also indicate that increasing Re enhances the exergy efficiency for both curvatures of turbulators. However, an increase in the lateral ratio of the curved turbulators leads to a drop in exergy efficiency. For both turbulator curvatures, when Re is increased from 4000 to 18000, with a lateral ratio of 14 mm and a volume fraction of 3%, the exergy efficiency improves by 23.26%. Conversely, exergy efficiency decreases as the lateral ratio increases. For example, with a constant

				volume fraction of 3% and Re = 18000, increasing the lateral ratio from 14 to 20 mm results in an 18.87% decrease in exergy efficiency.
[44]	Computational fluid dynamics (CFD) analysis of the thermal and hydraulic properties of a circular tube with twisted tape inserts.	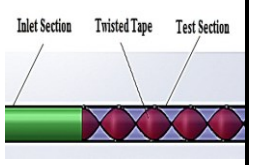	CFD	Based on numerical data, the twisted tape tube with different tape length ratios demonstrates superior thermo-hydraulic performance compared to the smooth tube. A full-length tape insert in the tube exhibits higher enhancement efficiency than one with a shorter tape. The average difference between the current anticipated CFD findings and the previously available Nu and f experimental data is 9%.
[23]	Investigation of the hydrothermal effects of utilizing two twisted tape inserts in a (PTSC) filled with MgO MWCNT /thermal oil hybrid nanofluid.		CFD	For a Reynolds number (Re) of 30,873, the suggested optimal (PTSC) configuration is the LCRW model, equipped with a turbulator diameter of 15 mm, and filled with a nanofluid containing a nanoparticle volume fraction of 2%. On the other hand, for Re values greater than 30,873, the LWRC model with the same turbulator diameter and nanofluid volume fraction is recommended as the optimum PTSC configuration.
[45]	Multi-semi-twisted tape	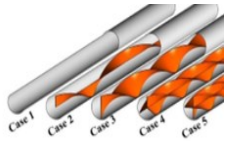	CFD	The number of swirl flow streams grows as the number of semi-twisted tapes increases, resulting in an increase in the local Nusselt number as well as the friction factor.

2.2 Criteria for Performance Enhancement

According to the previous literature study, heat transfer augmentation is accompanied by an increase in pressure drop. A drawback of thermal augmentation systems is higher pressure drop since it necessitates more pumping effort, which drives up operational expenses as well as pumping system investment costs. In this direction, proper criteria must be used to evaluate the increase in pressure drop. These criteria must account for both the pressure penalty and the thermal increase in comparison to the corresponding reference instance. For nanofluid cases, the operation with pure base fluid and with inserts or geometric changes, the use of a smooth absorber must be selected as the reference case.

The main concept is to employ criteria that comprise one thermal enhancement metric such as the heat transfer coefficient or the Nusselt number, and the thermal efficiency and one pressure loss parameter such as friction factor, pumping effort or pressure drop. For the overall evaluation of each approach, several parameters of these combinations are discovered in the literature. The most common criteria in the literature are listed below [24].

2.2.1 The criteria for flow performance

The friction factor ratio (f/fp) and the Nusselt number ratio (Nu/Nup) are used in these criteria, which focus on the fluid behaviour rather than the collector. These requirements may be more appropriate for heat transfer applications rather than solar collectors. These criteria are an attempt to explore the thermal increase of the heat transfer coefficient under various operating situations.

When the pumping work is constant, the performance evaluation criterion (PEC) is the most commonly used standard [24, 46].

This criterion is applied in situations where the pressure drop and flow rate are constant. This criterion may be described as making several problematic assumptions, notably for the nanofluid assessment (it implies that the thermal characteristics of the assessed and reference instances are similar) [24, 46, 47]:

PEC I - Same conditions for the pumping work

$$\eta_I = \frac{\left(Nu/Nu_p\right)}{\left(f/f_p\right)^{1/3}} \quad \text{..... (2.1)}$$

PEC II - Same conditions for the pressure drop

$$\eta_{II} = \frac{\left(Nu/Nu_p\right)}{\left(f/f_p\right)^{1/2}} \quad \text{..... (2.2)}$$

PEC III - Same conditions for the volumetric flow rate

$$\eta_{III} = \frac{\left(Nu/Nu_p\right)}{\left(f/f_p\right)} \quad \text{..... (2.3)}$$

So these parameters have values of more than one, the flow is deemed to have improved, and a larger amount of any of them implies greater improvement. The first criterion (η_I) considers the rise of the friction factor with a small value due to the tiny power "1/3", whereas the final one (η_{III}) focuses on the friction factor.

Figure 2.4 depicts the thermal improvement requirements geometrically. It is vital to note that the criteria η_{III} is a highly rigorous and challenging criterion to satisfy ($\eta_{III} > 1$), and it should only be utilized in circumstances when there is an urgent requirement for small-pressure drop growth. In general, the η_I is the most commonly used criterion in literature research, and it is a criterion that quickly reveals improvement if the Nusselt number increases [18, 24, 46].

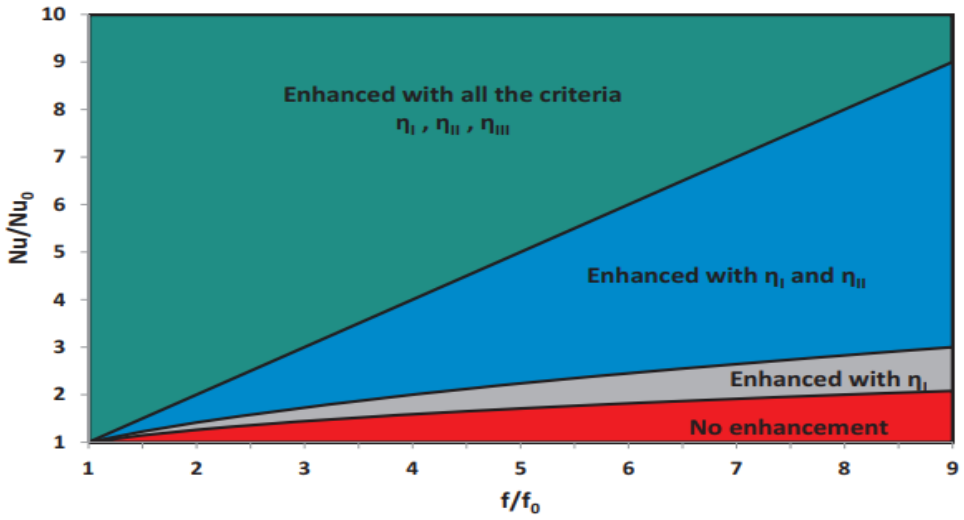

Figure 2.4: Geometrical criteria for the thermal enhancement performance [24].

2.3 Research gap

The literature suggests that because of the wide range of applications for PTSCs, enhancing their performance is a key priority for researchers all around the world. To improve the thermal properties of PTSCs, researchers have used innovative designs, corrugated channels, turbulators, and nanofluids. Many of these approaches, however, have the disadvantage of increasing the flow pressure drop. As a result, the hydrothermal efficacy of the PTSC has to be examined to assess the true efficiency of these approaches. Furthermore, energy studies can provide a useful perspective for designing more efficient thermal systems, such as PTSCs.

To fill such a gap this thesis presents a new absorber tube geometry with inserts of different twist tape ratios and the pitch ratio of the perforated plate arrangement is investigated for the heat transfer enhancement in the receiver tube. Further heat transfer is enhanced by using a tube with insertion and water-ZrO_2 nanofluid at different concentration ratios also investigated.

To the best of my understanding, there is no other work in the research that employs this twisted tape with perforated plate and water-ZrO_2 nanofluids enhancement techniques.

CHAPTER 3

METHODOLOGY

3.1 Description of the study area

Jigjiga town, which serves as the regional capital of Ethiopian Somalia, is situated in the Fafan zone, 675 kilometres from Addis Ababa and a little closer to Hargeyssa, the port of Somalia. Astronomically speaking, it is situated at 9°30' N latitude and 42°50' E longitude. It is located 1646 meters above sea level.

NASA will provide the measured worldwide solar radiation statistics. Since NASA Surface Meteorology and Solar Energy (SSE) has data on solar radiation measurements taken from space and recorded globally, see Appendix Table A 1 for details.

Among the Ethiopian cities, Jigjiga has an industrial core. As a result of the great potential of the location, solar power (electricity) will be one of the promising powers employed for communities as well as industry.

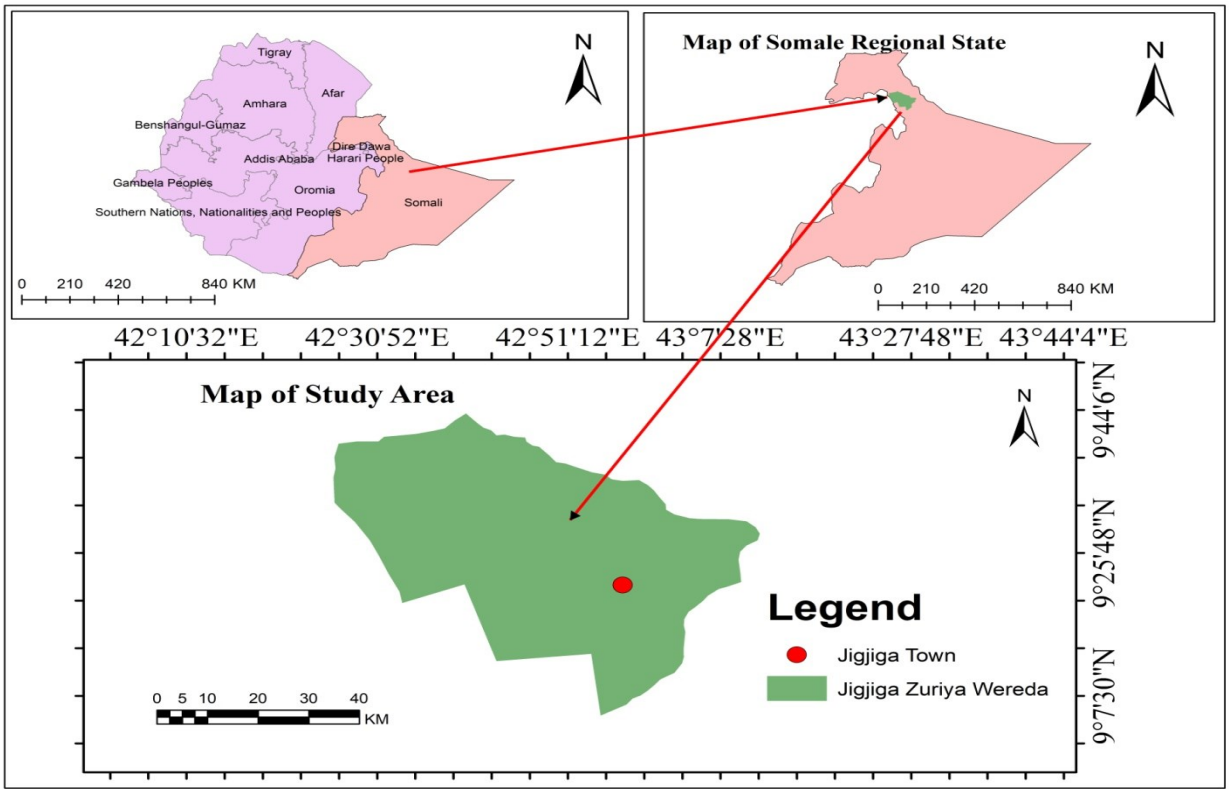

Figure 3.1: Map of the study area.

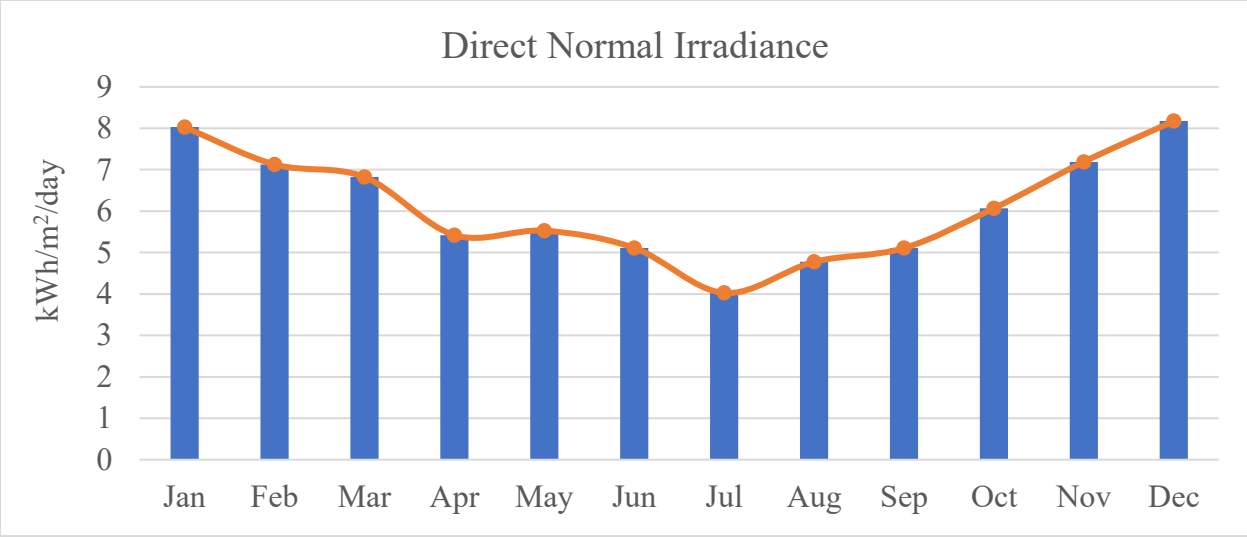

Figure 3.2: Monthly average direct normal irradiation (2017-2021 G.C).

(Source: https://power.larc.nasa.gov/data-access-viewer)

Figure 3.2: shows the monthly average direct normal radiation on the horizontal surface was minimal in July (4.026 kWh/m^2/day) and maximum in December (8.174 kWh/m^2/day). The average beam radiation throughout the year was considered for this simulation purpose (i.e. DNI of 6.114 kWh/m^2/day) see Appendix Table A1 for details.

3.2 Model description

In this section, the modelling of a PTSC is described in detail. First, Tonatiuh is employed to develop the PTSC module. Second, MATLAB is implemented to post-process data from the Tonatiuh simulation. Thirdly, to get the non-uniform distribution of heat flux in the receiver tube, user-defined functions (UDFs) are developed for the ANSYS Fluent program using post-processed data from MATLAB. The ANSYS Fluent software's PTSC module is then created, and UDFs are added to the already-existing fluent modelling. This optical modelling of the PTSC module is created using Tonatiuh v2.2.4. It is being developed with assistance from the National Renewable Energy Laboratory (NREL) from the University of Texas at Brownsville (UTB) and the National Renewable Energy Center of Spain (CENER) [48].

Tonatiuh models all the solar systems that use sunlight as a source of energy and runs simulations using the MCRT approach. In the beginning, SolTrace was intended to be employed for optical modelling. Afterwards, Tonatiuh was selected because of its user-friendly interface as well as ease of usage. It should be noted that one may input the component's properties (such as

reflectivity, aperture width, absorptivity, diameter, azimuth, etc.) and simultaneously observe the 3D model of the thing. With SolTrace, this can't be viable. Additionally, Tonatiuh employs a hierarchy of trees (see Figure 3.3) comparable to CAD software, which makes the model's layout extremely structured as well as user-friendly.

PTSC LS2 type was selected for the present work due to several practical and computational investigations available in the literature. Based on Bellos et al. [24], a mathematical model of a solar PTSC was created utilizing the parabola frame of an aperture area and the focus of an absorber tube shown in Table 3.1.

Table 3.1: Specification of solar PTSC [24]

Parameters	Sym	Dim	Parameters	Sym	Dim
Collector length	L	7.8 m	Cover emittance	ε_c	0.9
Collector width	w_a	5.0 m	Cover transmittance	τ	0.95
Focal distance	f	1.84 m	Receiver emittance	ε_r	0.2
Concentration ratio	C_r	22.74	Receiver absorptance	α	0.96
Receiver inner diameter	d_{ri}	0.066 m	Mirror reflectance	ρ_c	0.93
Receiver outer diameter	d_{ro}	0.07 m	Aperture area	Ap	39 m^2
Cover inner diameter	d_{ci}	0.109 m	Incident angle	θ	0°
Cover outer diameter	d_{co}	0.115 m	Direct normal irradiance	I_b	509.65 W/m^2

3.2.1 Tonatiuh geometry creation

Since it resembles CAD software, Tonatiuh's user interface is incredibly friendly for beginners. Figure 3.3 depicts Tonatiuh's overall outlook using a PTSC module.

Tonatiuh was used to design the whole PTSC system. One-axis trackers are mounted above the reflectors and receivers to follow the sun's path concurrently. A PTSC system with single-axis tracking travels east to west with the sun. See Appendix A to D for details of this PTC model.

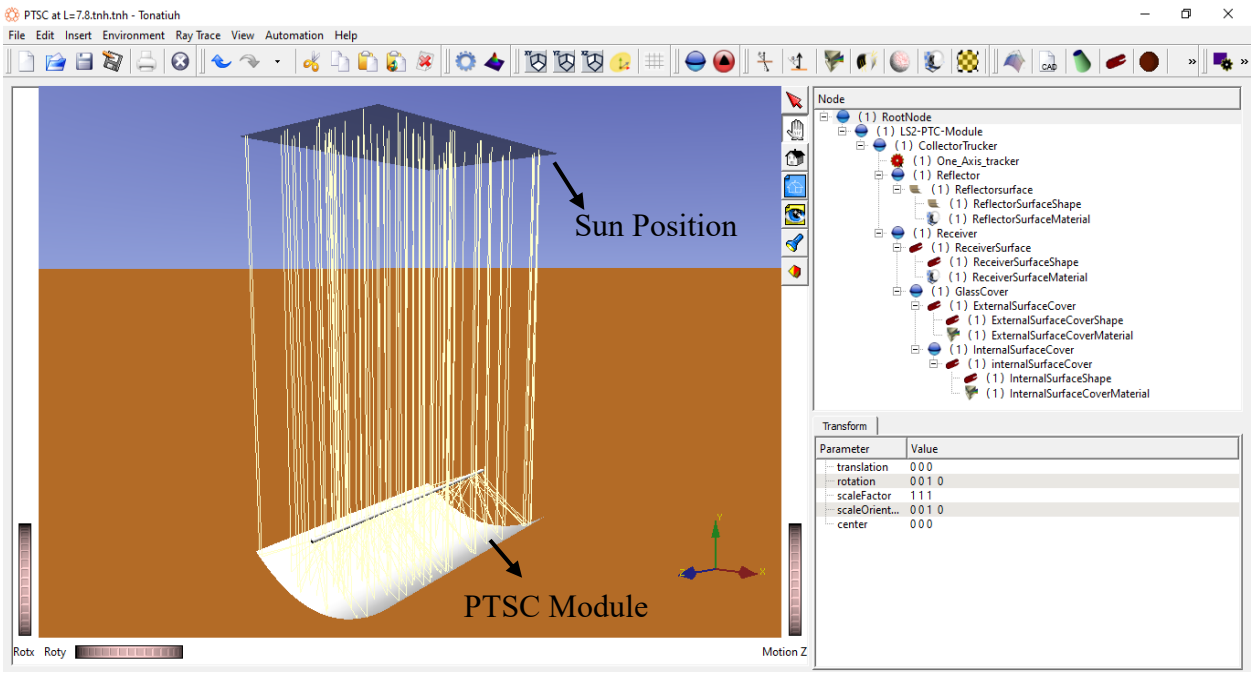

Figure 3.3: Overall view of Tonatiuh via the PTSC component.

3.2.2 Positioning a PTSC with a single-axis tracking system

The North-South (N-S) axis is the length of the PTSC system. In Tonatiuh, the N-S axis serves as the z-axis. Due to this providing the highest efficiency for a PTSC of the system, this N-S orientation was selected for this thesis [49]. Table 3.2 defines the Tonatiuh coordinate system. The orientation of the PTSC system is shown in Figure 3.4.

Table 3.2: A Tonatiuh's PTSC module coordinates

PTSC coordinates	Location
+x	East
-x	West
+z	South
-z	North

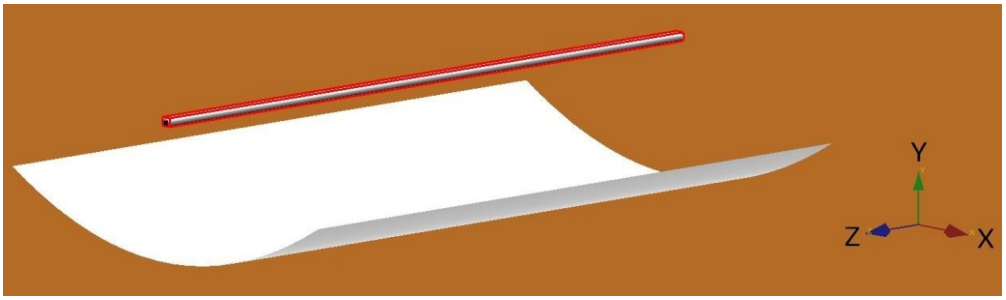

Figure 3.4: Position for the PTSC technology.

3.2.3 The number of rays

The total number of beams should be established before the tracing of ray simulations can begin, following the definition of PTSC geometry and the introduction of the Sun definition. Tonatiuh employs the MCRT technique, a stochastic strategy. To precisely calculate the total solar irradiation on the surface of the absorber tube, it is necessary to ensure that the number of rays employed is adequate. The number of rays is calculated using the SEGS LS-2 PTSC, which has a span of 7.8 m. Table 3.3 gives the overall power for a range of ray numbers on the absorber tube.

Table 3.3: The overall power on the absorber tube for various numbers of rays

Number of rays	Power absorbed by the absorber tube (W)
1000000	14578.1
2500000	14576.7
5000000	14577
7500000	14576.8
10000000	**14576.7**
15000000	14577

It is determined from Table 3.3 that 10 million beams will be enough for the optical analysis.

3.3 Use MATLAB for post-processing the absorber tube data

Post-processing the Tonatiuh simulated results and applying them as boundary conditions in the ANSYS Fluent software is one of the more complex aspects of this thesis. Because the tracing ray data is stored in a binary file, no other application may be used to see it. To access the source code file generated by the simulation result of Tonatiuh, MATLAB R2018a is employed. The binary file is used to extract each photon's precise position. In the receiver tube, spatial discretization applied in the direction radially is first carried out using a 2D code. The 2D code created for the ANSYS Fluent model is ultimately used to create user-defined functions (UDFs). See Appendix E and F for details.

3.3.1 Surface discretization of the receiver tube in 2D

Similar to all other research in the literature, the outer layer of the absorber tube is solely discretized in the radial direction. Zero incidence angles can be discretized in this method. The x-

direction represents the radial direction, whereas the z-direction represents the axial one. The outer layer of the receiver tube is split into four sections in the MATLAB code.

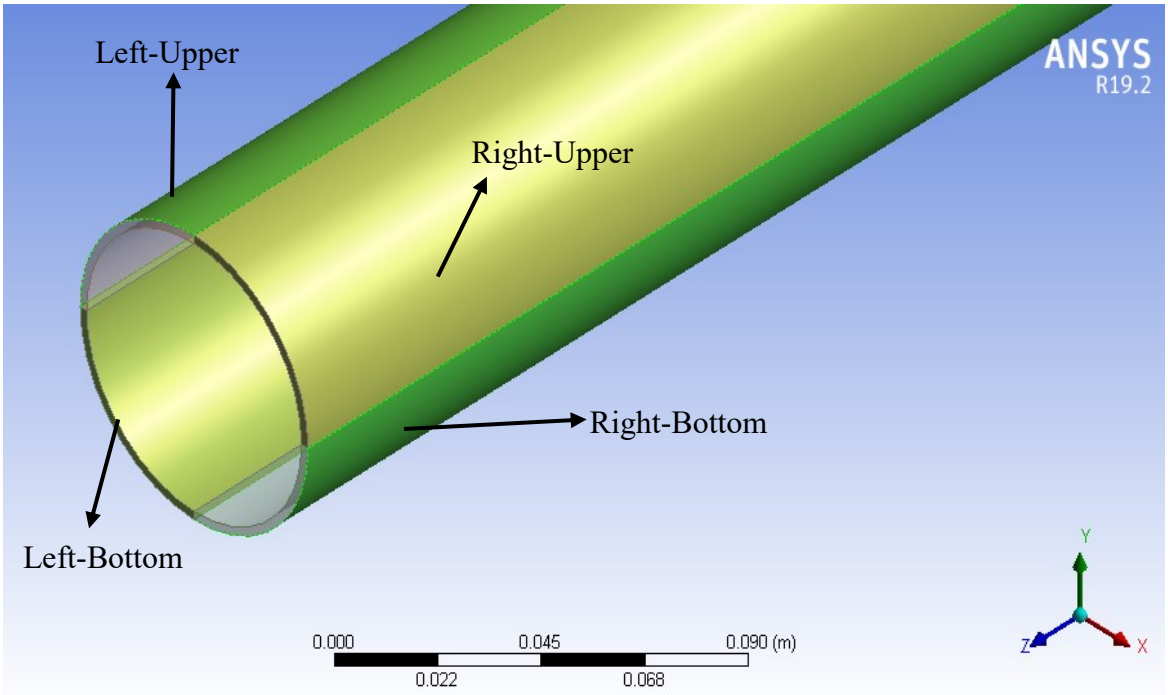

Figure 3.5: The absorber tube's outer surface is separated into four sections.

In comparison to "right-upper" and "left-upper" boundaries, which represent the absorber tube sections closest to a parabolic mirror, "left-bottom" and "right-bottom" surfaces receive a substantially larger heat flux. The absorber tube exterior surface is segmented into 360 strips in an angular (circumferential) orientation, ranging from 0 to 360 degrees with a 1-degree increment. One photon's strength and each photon's precise position are known. Each strip's energy is determined. The MATLAB code for the 2D discretization method is in Appendix F.

The curve fitting tool in MATLAB is then applied. Curve fitting is done in a piecewise function. The range from 0 to 0.035 m for the absorber tube outer surfaces is separated into 3 sub-intervals (Right Upper, Left Upper, Right Bottom, and Left-Bottom). APPENDIX G explains piecewise curve-fitting for the PTSC module's "Right-Upper" surfaces employing a zero-degree angle of incident.

3.3.2 Developing the absorber tube User-Defined Functions (UDFs)

The curve fit is used for 2D discretization. The right upper, left upper, right bottom and left bottom surfaces of the absorber tube are defined by polynomial equations in UDFs. These polynomial equations are the third or fourth order, and the sole independent variable is "x".

The UDFs are created using ANSYS Fluent's "DEFINE_PROFILE" function. "Notepad" is used to write the UDFs code and save it as a ".c" extension. After creating the UDFs for ANSYS Fluent to recognize them as C files. The discretization of the UDF's two-dimensional techniques for the PTSC section utilizing a 0° angle of incidence is seen in Appendix H. An overview of the procedure software used is shown in Figure 3.6.

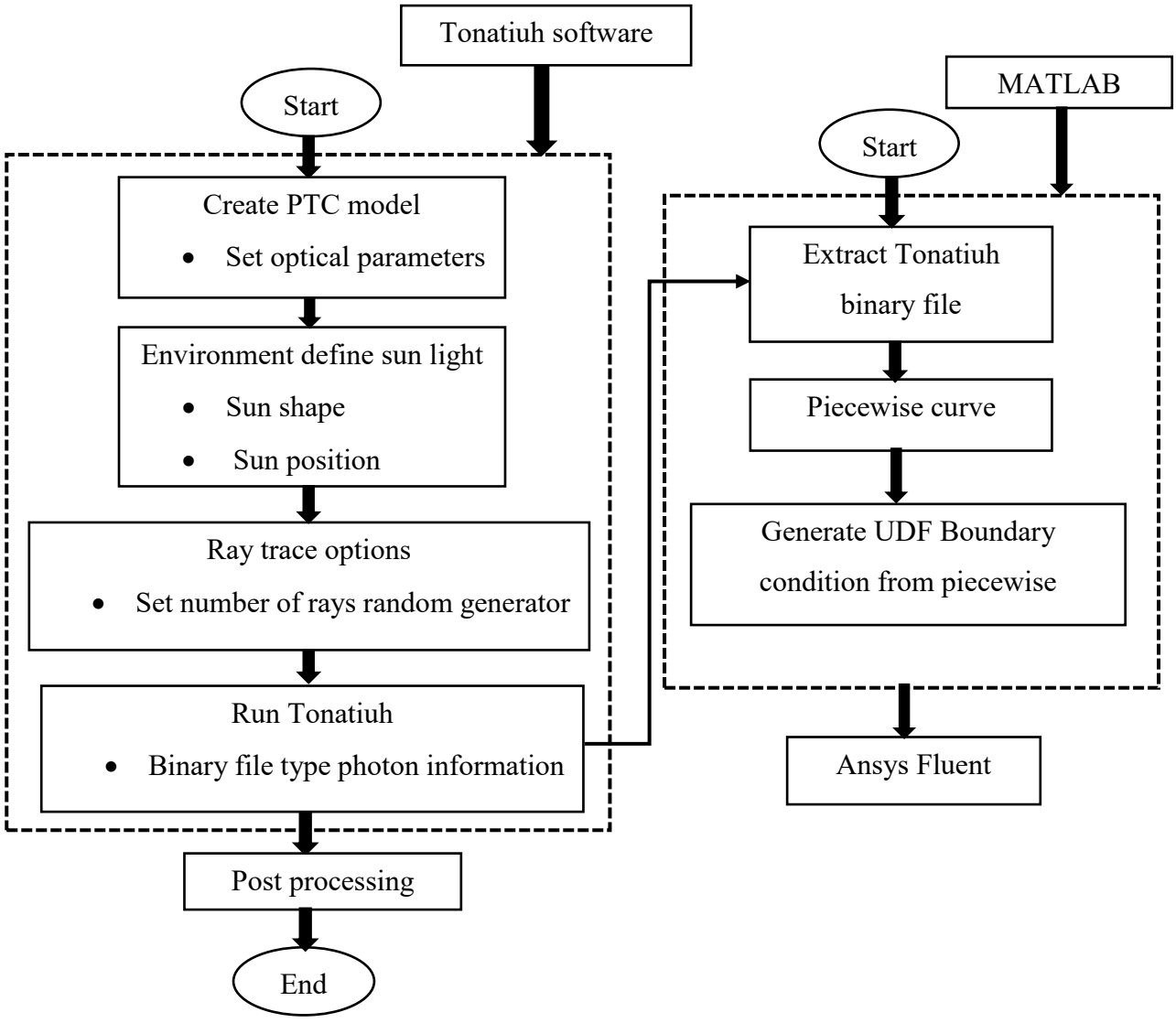

Figure 3.6: The overall flow chart of the simulation analysis.

CHAPTER 4

MODELING AND ANALYSIS

The notion of computational fluid dynamics and its application to the current study are discussed in this chapter. The physics necessary to solve the parabolic trough solar collector using this technique is also presented. This chapter also examines numerous assumptions used in the model to save computing costs. Following that, this part describes how to set up a simulation in ANSYS Fluent and conduct the calculations. As shown in Figure 4.1 the analysis was carried out in three steps using the CFD ANSYS FLUENT 19.2.

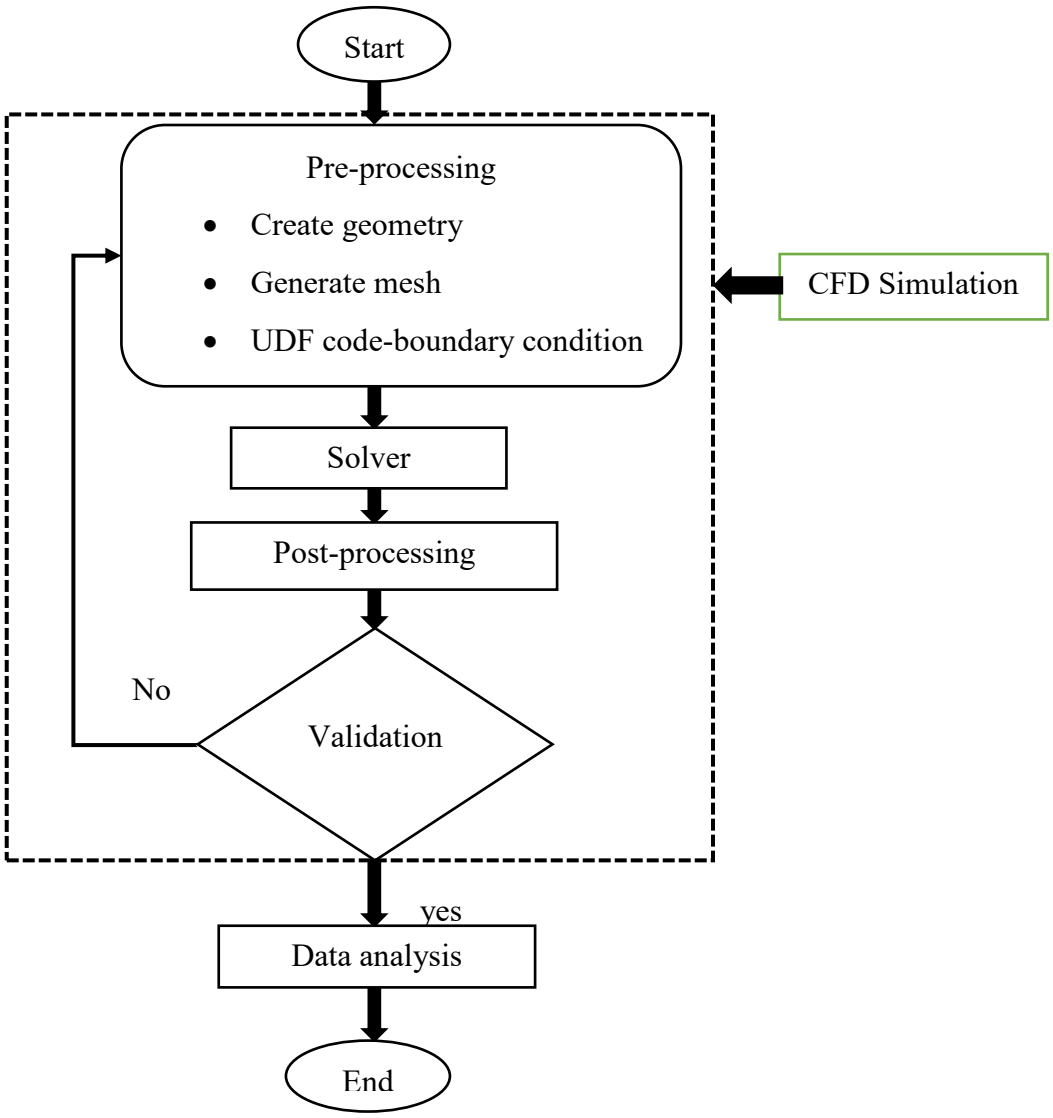

Figure 4.1: Modeling of Ansys fluent flow chart.

4.1 The geometry of the PT and PT with insertion of TT & PP

As shown in Figure 4.2 A for the typical absorber tube, the entire domain extends from z = 0 to z = 7.8 m. See Table 4.1 for further information on the geometry production process.

Table 4.1: Geometric specification of twisted tape and perforated plate

Twisted tape		**Reference**
Parameter	Value (m)	
Twisted tape length (L)	7.8 m	
Twisted tape width (w)	0.03 m	[50]
Twisted tape thickness (δ)	0.001 m	
Twist ratio, Tr = (y/w)	4, 5 & 6	
Perforated plate		
Perforated plate outer diameter (D)	0.066 m	[33, 50]
Perforated plate inner diameter (d)	0.054 m	
Small hole on perforated plate diameter (h)	0.004 m	
The thickness of each perforated plate (t)	0.002 m	
Number of triple sets of perforated plate	8 & 4	[33]
Distance between the triple sets of the perforated plate (l)	0.01 m	
Pitch length between triple sets of perforated plates (p)	0.8435 m and 1.5392 m	
Pitch ratio PR=(p/D)	12.78 and 23.32	

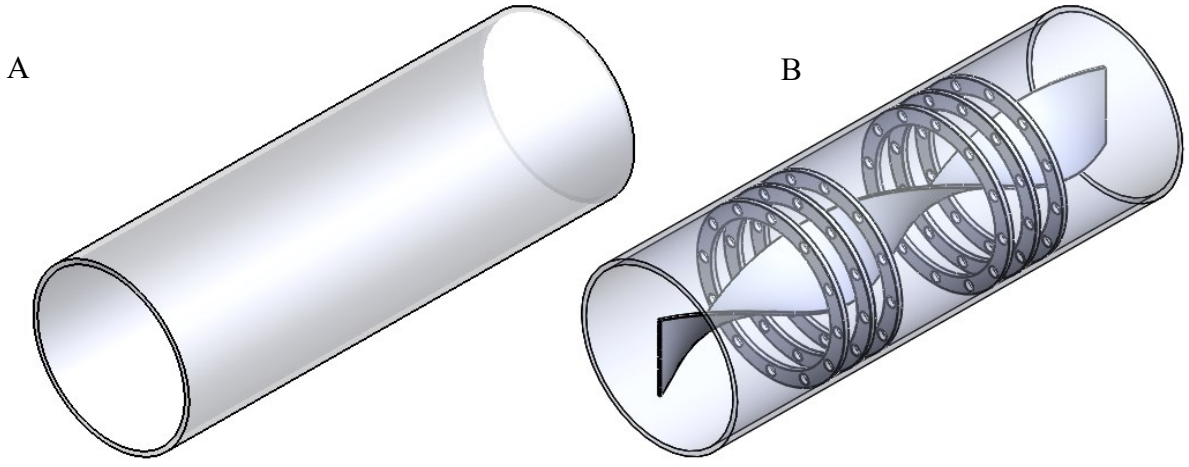

Figure 4.2: Isometric View of (A), Plain Tube (PT) alone (B), PT with Twisted tape (TT), and Perforated plate (PP) insert.

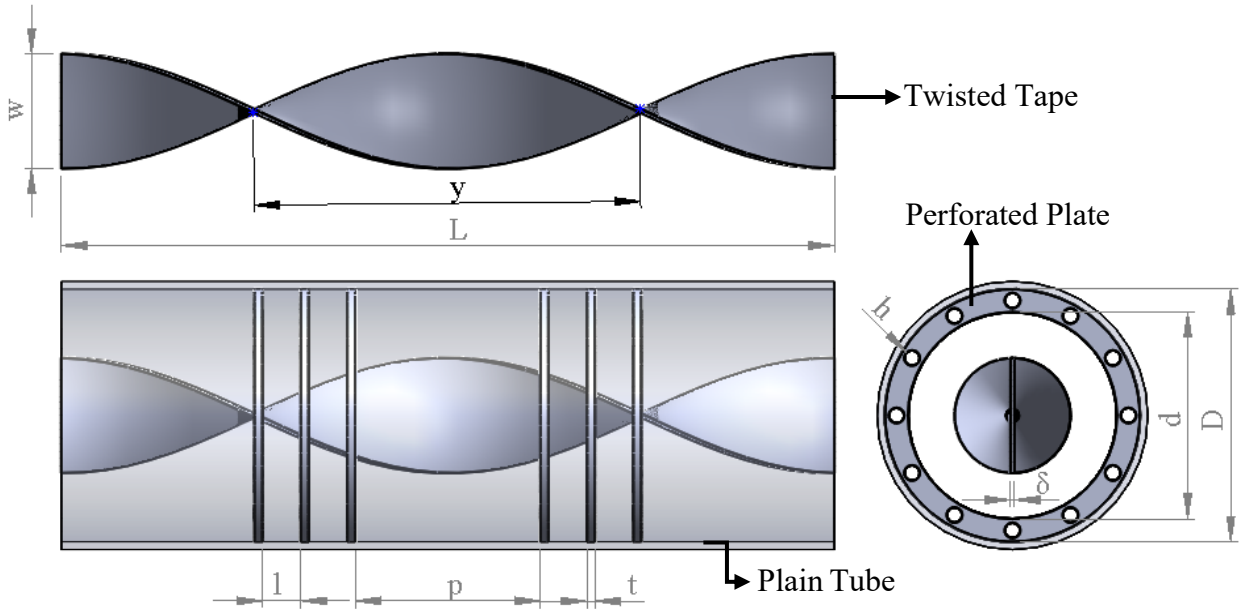

Figure 4.3: Geometric specification of the PT with TT and PP insert.

Figure 4.2 B depicts the geometric specification of the receiver tube with a TT and PP insert. The solid domains consist of plain tubes with TT and PP inserts. See Figure 4.3 In this investigation, TT at various twist ratios (Tr=y/w= 4, 5, & 6) and PP at various sets of numbers 4 and 8 are used in a configuration of 3 loops in a row, and filled with water-ZrO_2 nanofluids. In this study, we have attempted to examine the role of water-ZrO_2 nanofluid and twisted tape with perforated plate turbulators in enhancing the heat transmission of the receiver tube compared to the plain tube (PT). To compare the intended absorbent and the manufactured turbulators accurately and assess the effect of the improvement on enhancing heat transmission, we first evaluate the PT as a reference [33, 51].

4.2 The mesh generation of the PT and PT with insertion of TT & PP

The multi-zone approach is employed to reduce the amount of elements and nodes and the duration of calculation. The interior of the absorber tube is covered by inflation layers [3]. The mesh of a plain tube, a plain tube with twisted tape, and a perforated plate insert with the fluid region are shown in Figure 4.4, with twist ratios of Tr=(y/w)=4, 5, and 6, and pitch ratios of PR=(p/D)=12.78 respectively. The section view of the skewness distribution of the plain tube, plain tube with twisted tape and perforated plate insert at twist ratio of Tr = (y/w) =4, 5, & 6 and pitch ratio of PR = (p/D) =12.78 are given in Figure 4.5, respectively.

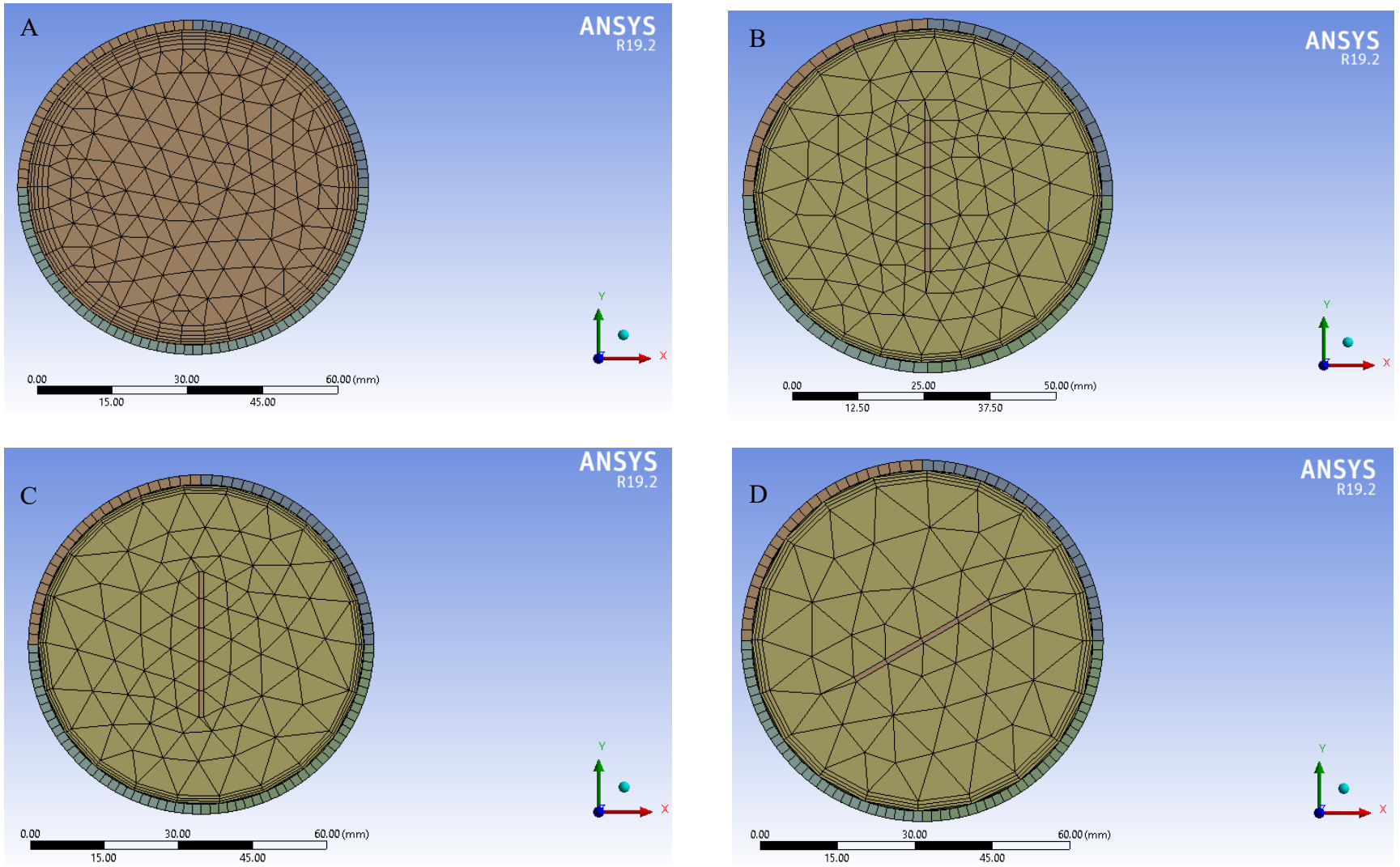

Figure 4.4: The mesh of the (A) PT, (B), PT with Tr=4 & 8-Turbulator (C), PT with Tr=5 & 8-Turbulator (D), PT with Tr=6 & 8-Turbulator.

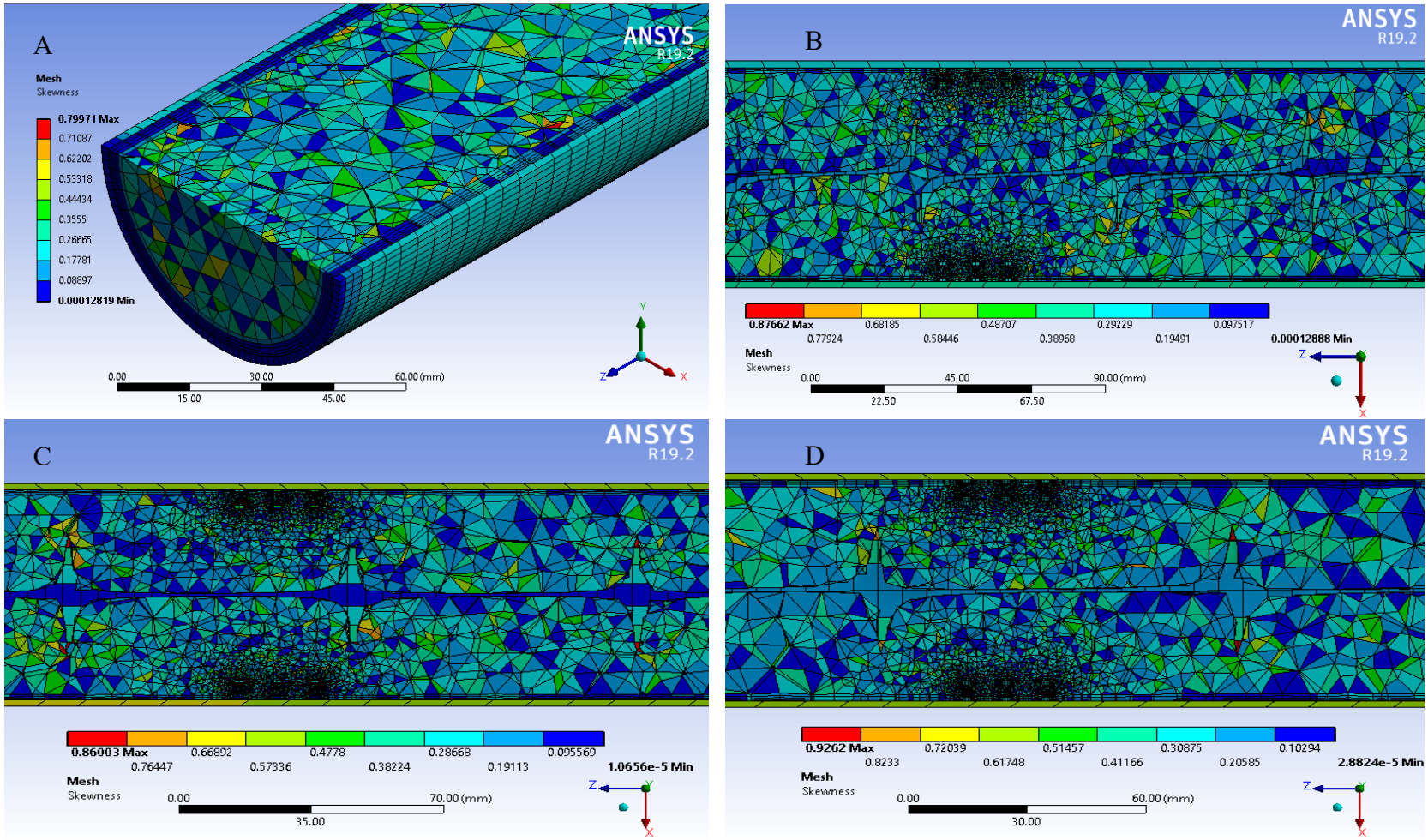

Figure 4.5: The section view of the skewness distribution of the (A) PT, (B), PT with Tr=4 & 8-Turbulator (C), PT with Tr=5 & 8-Turbulator (D), PT with Tr=6 & 8-Turbulator.

The other model of the receiver with twisted tape and perforated plate insert at twist tape ratio of Tr=4, 5, & 6 and pitch ratio of PR=23.32 are the same as the above method.

4.3 The governing equations

In this study, we assumed that the flow inside the absorber tube was a fully formed, steady-state turbulent flow. In addition to ensuring higher heat transfer coefficients and higher performance, this also contributes to decreasing the temperature gradients in the absorber tube, shielding the receiver tube from thermal stresses and eventual failure. The basic equations used are listed below [52].

Continuity equation

$$\nabla.\mathrm{u} = 0 \quad \text{……………………………..……..……………………}(4.1)$$

Momentum equation

$$\frac{\partial \mathrm{u}}{\partial \mathrm{t}} + \nabla.(\mathrm{uu}) = -\frac{1}{\rho}\nabla \mathrm{p} + \upsilon\nabla^2 u \quad \text{…………….……………...…….}\ (4.2)$$

Energy equation

$$\frac{\partial \mathrm{T}}{\partial \mathrm{t}} + \nabla.(\mathrm{uT}) = \alpha\nabla^2\mathrm{T} + \mathrm{q} \quad \text{……………………….………………}\ (4.3)$$

In the aforementioned equations u, p, T and q stand for the fluid velocity component, pressure, temperature and source term respectively.

Turbulence model

Researchers validated numerous turbulence models to choose a suitable model for CFD analysis. Standard k-model Realizable k-model and produced under predicted results, while Standard k-model and SST k-model produced over predicted results, they noted. The results of k-turbulence models produced by the renormalisation group (RNG) are in good agreement with the Petukhov, Dittus, and Boelter results. The RNG k-Epsilon with Enhanced Wall Treatment was chosen because of its excellent performance in more difficult main flow fields, accurate spreading rate prediction, high convergence rate, and relatively low memory usage. All simulations were required to represent the high resolution of gradients in the near-wall areas with a y^+ value in the range of 1-5. The improved wall treatment was used to represent the near-wall parts [38, 49]. Where $y^+ = y\mu_\tau/\upsilon$, μ_τ is the friction velocity given by $\mu_\tau = \sqrt{\tau_w/\rho}$, y is the distance from the wall, and υ is the fluid's kinematic viscosity [38].

Table 4.2: Comparison of various CFD models of coefficient determination (R^2) values [53]

Model	Coefficient of determination (R^2)
Renormalization k−ε	0.998
Standard k−ε	0.996
Realizable k−ε	0.995
Shear Stress Transport (SST) k−ω	0.994

The transport equation for the RNG k-$\boldsymbol{\varepsilon}$ model [54]

k-equation turbulent kinetic energy

$$\frac{\partial}{\partial t}(\rho k)+\frac{\partial}{\partial x_i}(\rho k u_i)=\frac{\partial}{\partial x_j}\left(\alpha_k \mu_{eff}\frac{\partial k}{\partial x_j}\right)+G_k+G_b-\rho\epsilon-Y_M+S_k \quad \ldots\ldots\ldots\ldots\ldots\ldots (4.4)$$

Rate of dissipation

$$\frac{\partial}{\partial t}(\rho\epsilon)+\frac{\partial}{\partial x_i}(\rho\epsilon u_i)=\frac{\partial}{\partial x_j}\left(\alpha_\epsilon \mu_{eff}\frac{\partial \epsilon}{\partial x_j}\right)+C_{1\epsilon}\frac{\epsilon}{k}(G_k+C_{3\epsilon}G_{b)}-C_{2\epsilon}\rho\frac{\epsilon}{k}-R_\epsilon+S_\epsilon \ldots. (4.5)$$

Whereas, S_k, and S_ϵ are source terms user-defined, Y_M is the contribution of the fluctuating dilatation incompressible turbulence to the overall dissipation rate, G_b is the turbulence kinetic energy generated due to buoyancy, G_k represents the generation of turbulence kinetic energy due to the mean velocity gradients, the quantities α_k and α_ϵ are the inverse effective Prandtl numbers for k and ε respectively [55].

The eddy viscosity is computed from

$$\mu_t=\rho C_\mu\frac{k^2}{\epsilon} \ldots\ldots\ldots\ldots\ldots\ldots\ldots\ldots\ldots\ldots\ldots\ldots\ldots\ldots\ldots\ldots(4.6)$$

R_ϵ Is given by, $R_\epsilon=\frac{C_\mu\eta^3\left(1-\eta/\eta_0\right)}{1+\Psi\eta^3}\frac{\epsilon^2}{k}$ ……………………………………………………..……(4.7)

The RNG theory gives the values of constants as $\eta=S\frac{k}{\epsilon}$, $S^2=2S_{ij}S_{ij}$, ($C_{1\varepsilon}$, $C_{2\varepsilon}$, η_o, Ψ and C_μ are turbulent model constants)

Table 4.3: The constants of RNG K-mode [39, 54]

C_μ	η_o	$C_{1\varepsilon}$	$C_{2\varepsilon}$	α_k	α_ϵ	Ψ
0.0845	4.38	1.42	1.68	1.39	1.39	0.012

Turbulence intensity is used to establish the inlet's turbulence characteristics [42].

$$I=0.16\times(Re_{DH})^{-1/8} \ldots\ldots\ldots\ldots\ldots\ldots\ldots\ldots\ldots\ldots\ldots\ldots\ldots\ldots\ldots (4.8)$$

Table 4.4: Summary of Operating Conditions

Models		
Energy	On	
Viscus model	K epsilon	
	K epsilon model	RNG
	Near wall treatment	Enhanced wall treatment

4.4 The boundary conditions

In CFD ANSYS Fluent, the boundary conditions for various faces were constructed while the grid's geometry was being built.

(i) Boundary conditions at inlets at the receiver intake, the flow has a uniform velocity at an ambient temperature [17].

$$u = U_{in,}\ T_f = T_{in} @ L = 0\ m \quad \ldots\ldots (4.9)$$

$$0 \le r \le \frac{d}{2}, \qquad -90° \le \theta \le 90°$$

(ii) Wall boundary condition: No-slip conditions exist inside the pipe wall

$$u = 0 @ r = \frac{d}{2} \quad \ldots\ldots (4.10)$$

$$90° \le \theta \le -90°$$

(iii) Heat flux that is not uniform on the outside of the absorber tube. Using the MCRT technique and an aperture width of 5 m or a concentration ratio (C_r) of 22.74, the sample distribution of heat flux utilized in this investigation was calculated. The receiver tube's outside wall is subjected to an uneven concentrated heat flux [56].

$$q'' = LCR \times I_b \quad \ldots\ldots (4.11)$$

Where I_b stand for direct normal irradiation, which is considered to be 509.65 W/m^2. Figure 4.6 depicts the distribution of the local concentration ratio (LCR) on the surface of the absorber tube. The radiation emitted from the receiver's outer surface is not considered because the heat transfer performance is analyzed within the receiver, as in the references [18]. The Fluent model is subsequently applied to UDFs. The procedure outlined here is carried out.

$$User\ Defined \rightarrow Functions \rightarrow \text{Interpreted}$$

Select the UDFs for the absorber tubes outside surfaces in the "Boundary Conditions" field.

(iv) Zero pressure gradient across the outlet boundary condition is employed.

Table 4.5: Summary of boundary conditions

Boundary conditions		
Inlet	Velocity inlet	
	Velocity magnitude	Calculated from Reynolds numbers
	Temperature	303.15 K
Outlet	Pressure outlet	
	Gauge pressure	0 pascal
Right-upper, Right-bottom, Left-upper, and Left-bottom wall	wall	
	Wall motion	Stationary wall
	Shear condition	No slip
	Heat flux	UDF code - calculated from MCRT

4.4.1 Local concentration ratio (LCR) validation with Jeter's ideal PTC

The local concentration ratio distribution is confirmed in this section using numerical studies from the literature. It is compared to Jeter [57], which investigates a hypothetical PTSC with a uniform sun angular radius of 4.65mrad, a 0° angle of incidence, a 90° rim angle, and a 20x geometrical concentration ratio. This ideal PTC is investigated by employing 2D-discretization MATLAB and the Tonatiuh technique (which could be applied for a 0° angle of incidence). The optical characteristics of this ideal PTSC are listed in Table 4.6.

Table 4.6: PTSC ideal Jeter module [3]

Parameters	**Value**	**Unit**
Mirror Reflectivity	1	-
Absorber tube Coating Absorptivity	1	-
Glass Cover Transmissivity	1	-

The other parameters are similar to this thesis model described in the previous chapter.

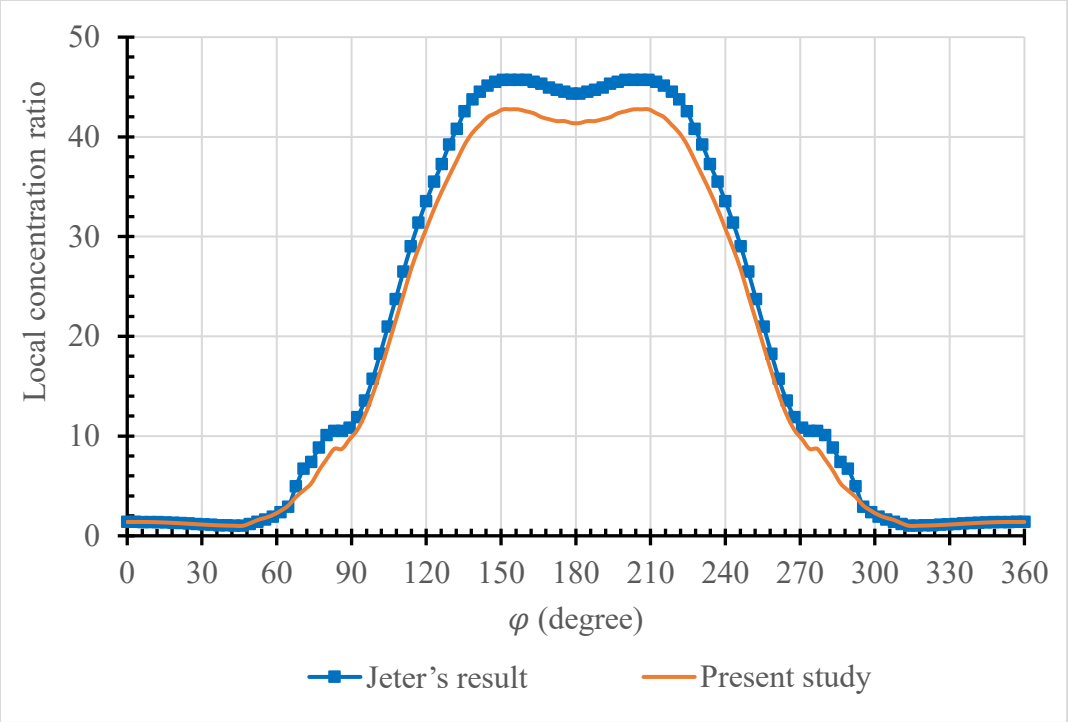

Figure 4.6: The LCR of Jeter's ideal [57] compared with the present study.

The distribution LCR of the present study is well-aligned with that of Jeter's [57] work, as shown in Figure 4.6. To generate a cross-section of the receiver tube and determine the distribution of heat flux, refer to Appendix I and J. In conclusion, boundary condition simulation data of Tonatiuh is precisely delivered to ANSYS Fluent. This data includes the distribution of heat flux and the amount of heat flux in the receiver tube. UDFs are constructed using piecewise surface fits. The optical method used in this thesis, which comprises creating the PTSC using Tonatiuh and analyzing the Tonatiuh data afterwards with MATLAB, can accurately determine the non-uniform distribution of the heat flux around the receiver tube.

4.5 Material properties

The property of the material in a PTSC, is given as fluid (nanofluid), absorber tube as solid (copper), Perforated plate and twisted tape as solid (aluminium).

Table 4.7: Material properties [34, 53, 58]

Material	Density (kg/ m^3)	Specific heat (J/kg K)	Thermal conductivity (W/m K)
Aluminum	2719	871	202.4
Copper	8978	381	387.6

4.6 Thermophysical properties of nanofluids

Water-ZrO_2 nanofluid is used as the working fluid, and its characteristics are made to be constant and determined by the temperature at the input. Simple algebraic equations may be used to determine the thermophysical characteristics of the nanofluid when considering single-phase flow. In the present study's literature, they are discussed and used. The following equations yield the relevant values of dynamic viscosity, thermal conductivity, specific heat capacity, and density.

4.6.1 Density of nanofluid

The model is derived by assuming a balanced state between the particles and the fluid [17, 59, 60].

$$\rho_{nf} = \left(\frac{m}{\nu}\right)_{nf} = \frac{m_f + m_p}{\nu_f + \nu_p} = \frac{\rho_f \nu_f + \rho_p \nu_p}{\nu_f + \nu_p} = \rho_f(1-\phi) + \rho_p\phi \quad \text{..... (4.12)}$$

Where: ϕ= Nano-particles concentration ratio in a nanofluid.

Subscripts: p = stands for nanoparticle

f = stands for fluid

4.6.2 Specific heat capacity of nanofluid

The specific heat capacity of the nanofluid is determined using this formula [60].

$$C_{p_{nf}} = C_{p_f}(1-\phi) - C_{p_p}\phi \quad \text{..... (4.13)}$$

4.6.3 Viscosity of nanofluid

In this study, Einstein's model is employed. Various formulas have been used to calculate the viscosity of the nanofluids [60].

$$\mu_{nf} = \mu_f(1 + 2.5\,\phi) \quad \text{..... (4.14)}$$

4.6.4 Thermal-conductivity of nanofluids

It is the most important element in analyzing the heat transfer of nanofluids. Several models exist; in this study, the Maxwell model is utilized [61].

$$k_{nf} = k_f \frac{k_p + 2k_f + 2\phi(k_p - k_f)}{k_p + 2k_f - \phi(k_p - k_f)} \quad \text{..... (4.15)}$$

In this investigation, a ZrO_2 nanofluid with four-volume concentrations is employed, as shown in Figure 4.7. The parameters of the nanofluid are determined using Equations (4.12)-(4.15) dependent on the concentration of nanoparticles. Since this fluid is not automatically included in the ANSYS-FLUENT software library, we must write its attributes in the UDF code and add it to the program. See Appendix Table A 2 and Appendix H for details.

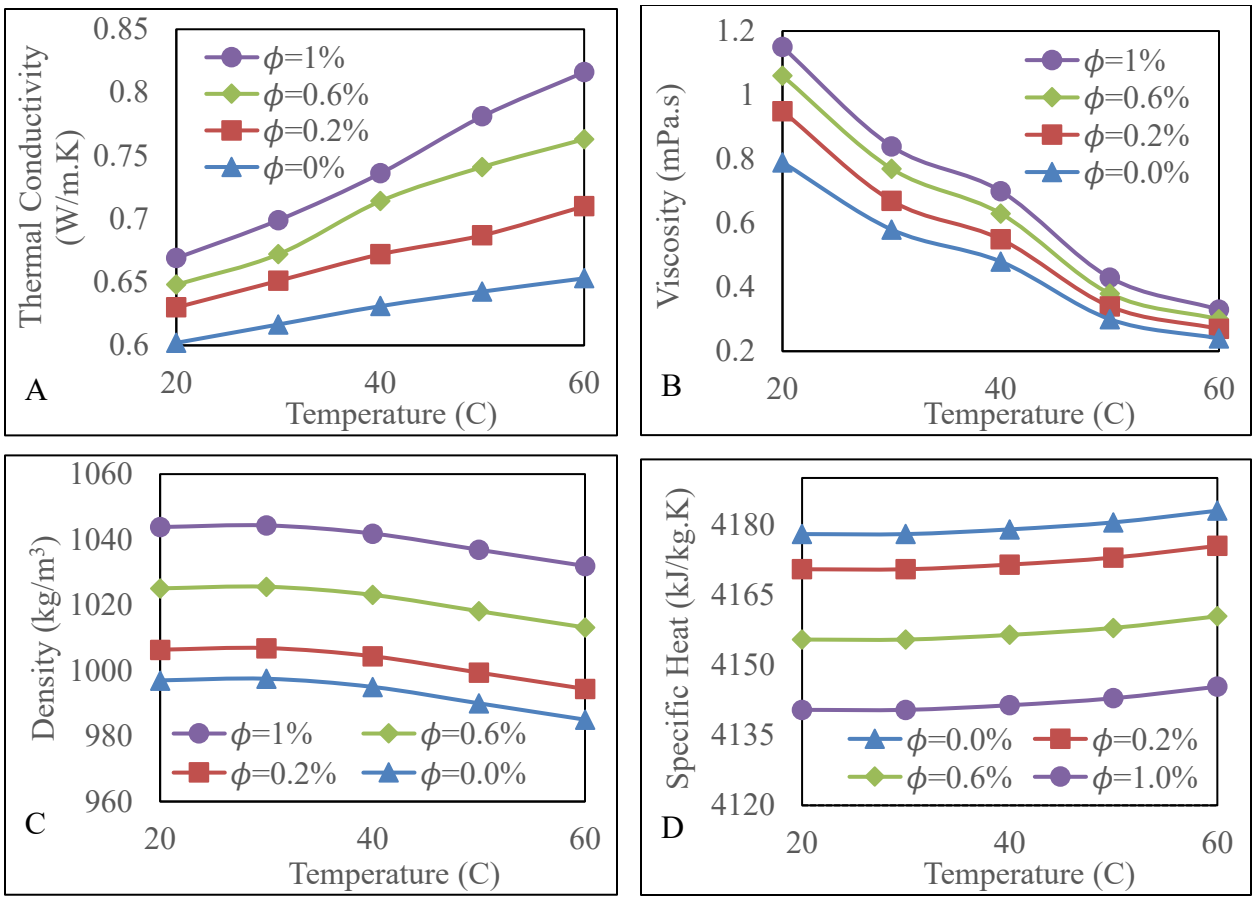

Figure 4.7: (A) Thermal conductivity, (B) Viscosity, (C) Density, (D) Specific heat of the water-ZrO_2 nanofluid at different concentration ratios [51].

4.7 Dimensionless parameters

By allowing the PTR heat transfer fluid to run through a copper tube, its capacity for heat transfer is examined. The Nusselt number (Nu), the heat transfer coefficient (h), the Reynolds number (Re), and the friction factor (f) are defined as follows:

$$\mathrm{Nu} = \frac{\mathrm{hD}}{\mathrm{K}} \quad \text{..... (4.16)}$$

Where h is derived from the following

$$\mathrm{h} = \frac{\mathrm{q''}}{(\mathrm{T_{wall}} - \mathrm{T_{fluid}})} \quad \text{..... (4.17)}$$

Where Twall is the average wall temperature and $\mathrm{T_{fluid}} = \frac{\mathrm{T_{in}} + \mathrm{T_{out}}}{2}$.

Reynolds number is derived as follows:

$$\mathrm{Re} = \frac{\mathrm{Dv}}{\upsilon} = \frac{\rho * \mathrm{D} * \mathrm{v}}{\mu} \quad \text{..... (4.18)}$$

The receiver tube friction factor is given as [16]:

$$f = \frac{2.\Delta P.D}{L.\rho.v^2} \quad \text{.....(4.19)}$$

Where v, ΔP, and L denote the mean velocity, the pressure drop of the working fluid, and the length of the receiver tube, respectively.

4.8 Solution procedure

In the current simulation, the governing equations of continuity, momentum, and energy are solved in the steady-state domain using the finite volume method. It is determined to solve the energy and momentum equations with a second-order upwind method. The double-precision pressure-based solver was utilized to resolve the given set of equations [33, 53]. All of the transport equations use the second-order upwind discretization approach. In a steady state, implicit linearization is used to solve the governing equations for momentum and mass conservation sequentially. This method is known as a segregated approach. Pressure and velocity are connected using the SIMPLE algorithm, a semi-implicit approach for pressure-related equations. The discretized energy equation was then solved after the resolution of the continuity and momentum conservation equations as well as the velocity field. The convergence requirements for the continuity and energy equations are 10^{-3} and 10^{-6}, respectively. The scaled residuals were all set to be 10^{-4} for the equations describing the convergence of momentum, turbulent kinetic energy, and turbulent dissipation rate [33, 62]. The type of scheme, gradient, and initialization applied for each model is summarized in Table 4.8.

Table 4.8: The Solution and Initialization Method

Solution method		
Pressure velocity coupling	Scheme	Simple
Special discretization	Gradient	Least square cell-based
	Pressure	Second order
	Momentum, Turbulent kinetic energy Turbulent dissipation rate, Energy	Second order upwind
Initialization		
Initialization method		Hybrid initialization

4.8.1 Convergence test

As shown in Figure 4.8 the scaled residuals solution is converged after 495 iterations. From Figure 4.9 the average output temperature is constant around 50 iterations which means the flow is thermally fully developed.

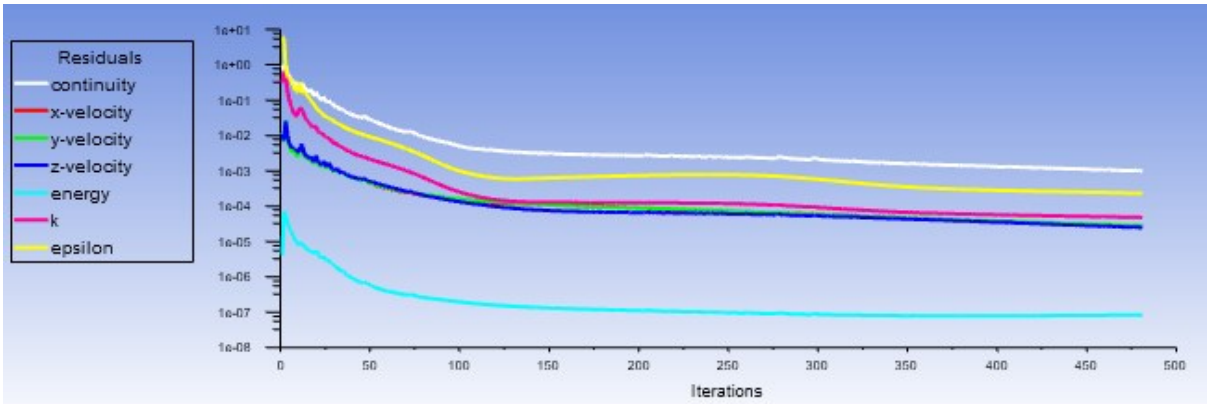

Figure 4.8: Scaled residuals.

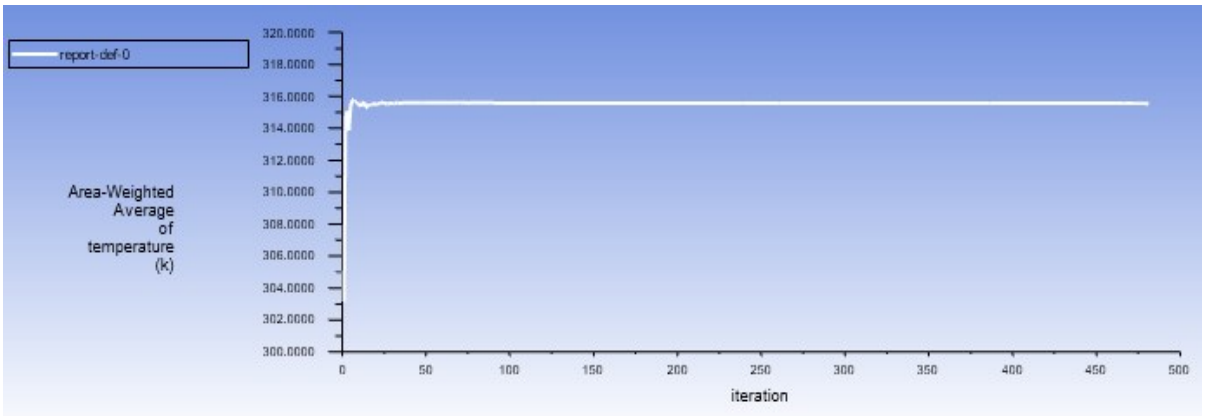

Figure 4.9: Average output temperature.

4.8.2 Grid independence test

By considering four grid systems with a significant number of grid points, a thorough analysis of the grid dependency of the numerical solutions, 585000 cells, 810270 cells, 950089 cells, and 1140516 cells at Re = 4000, was conducted. Table 4.9 shows the average Nusselt number and the output temperature for these four grid designs. The relative variances of averaged temperature and Nusselt numbers are observed to decrease as the grid's mesh number increases. Thus, the grid structure of 950089 cells is chosen to reduce computer resources while maintaining a balance between prediction accuracy and computational memory.

Table 4.9: Grid independence test of the plain tube at $\phi = 0\%, Re = 4000$ & $T_{in} = 303.15K$

Grid system	Grid	Nu	T_{out} (K)	Nu-difference (%) $\frac{\lvert Nu_{i+1} - Nu \rvert}{Nu}$	Temperature difference (%) $\frac{\lvert T_{out_{i+1}} - T_{out} \rvert}{T_{out}}$
Grid 1	585000	35.217	332.534	-	-
Grid 2	810270	34.581	332.173	1.805	0.108
Grid 3	950089	34.0153	331.824	1.635	0.105
Grid 4	1140516	33.5415	331.823	1.392	0.0003

4.9 Validation of the CFD model

To show the accuracy and validity of the model and numerical solution used in the current study, the Nusselt number produced from the present numerical code is compared with the Nusselt number computed from the Dittus-Boelter and Petukhov correlation.

For $3000 < Re < 5 \times 10^5$ and $0.7 < Pr < 160$ is possible to use the Petukhov correlation, given by [63].

$$Nu = 0.125 \times f \times Re \times Pr^{\frac{1}{3}} \quad (4.20)$$

Where f is the friction factor given by:

$$f = (0.79 LnRe - 1.64)^{-2} \quad (4.21)$$

For $2500 < Re < 10^5$ and $0.7 < Pr < 120$ is possible to use the Dittus-Boelter correlation [64].

$$Nu = 0.023 \times Re^{0.8} \times Pr^{0.4} \quad (4.22)$$

for $2000 < Re < 22000; 0 < \phi < 1\%$ The friction factor equation of ZrO_2 nanofluids is proposed by [51].

$$f = 0.282 \times Re^{-0.2369}(1 + \phi)^{0.09724} \quad (4.23)$$

The CFD analyses can be carried out once the MATLAB code for 2D discretization and the heat flux boundary condition have been verified. The data validation process is essential to having a high level of trust in the outcomes. Therefore, it is necessary to verify the correctness of the Nusselt number and friction factor values for the plain tube that was determined using equations (4.16) and (4.19) of the CFD outputs. This check is done by calculating the two quantities from the CFD simulation and compares with the Petukhov, Dittus-Boelter correlation and Eiamsa-ard et al., 2013 for the Nusselt number, and Petukhov, Blasius, Sundar correlations, and Eiamsa-ard et al., 2013 for friction factor, referred by equations from (4.20 - 4.23).

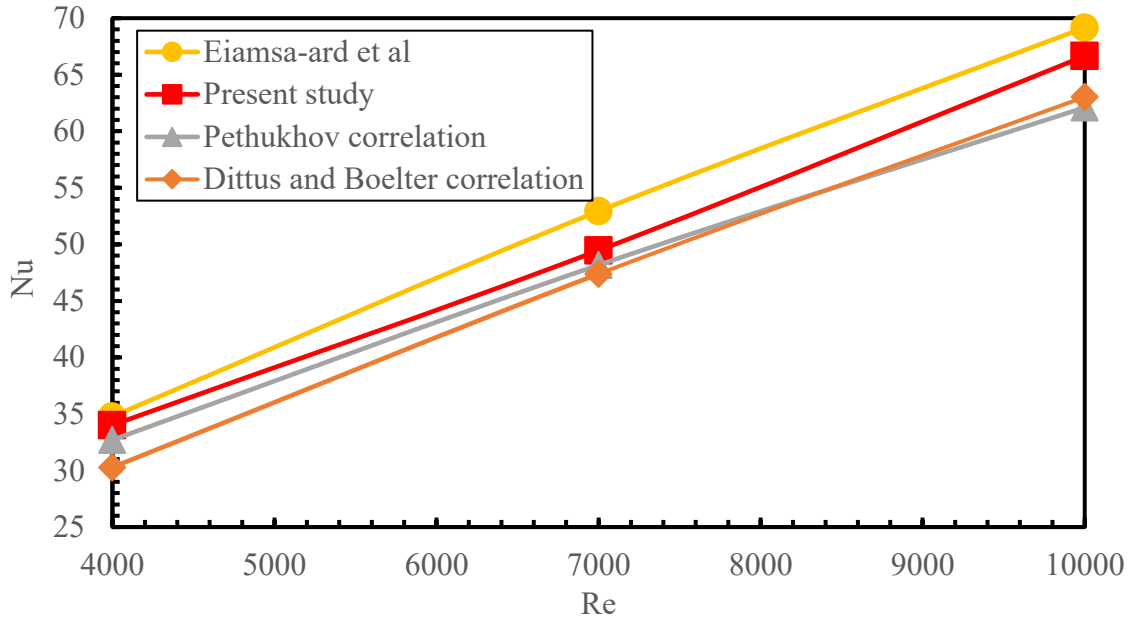

Figure 4.10: Validation of Nusselt number.

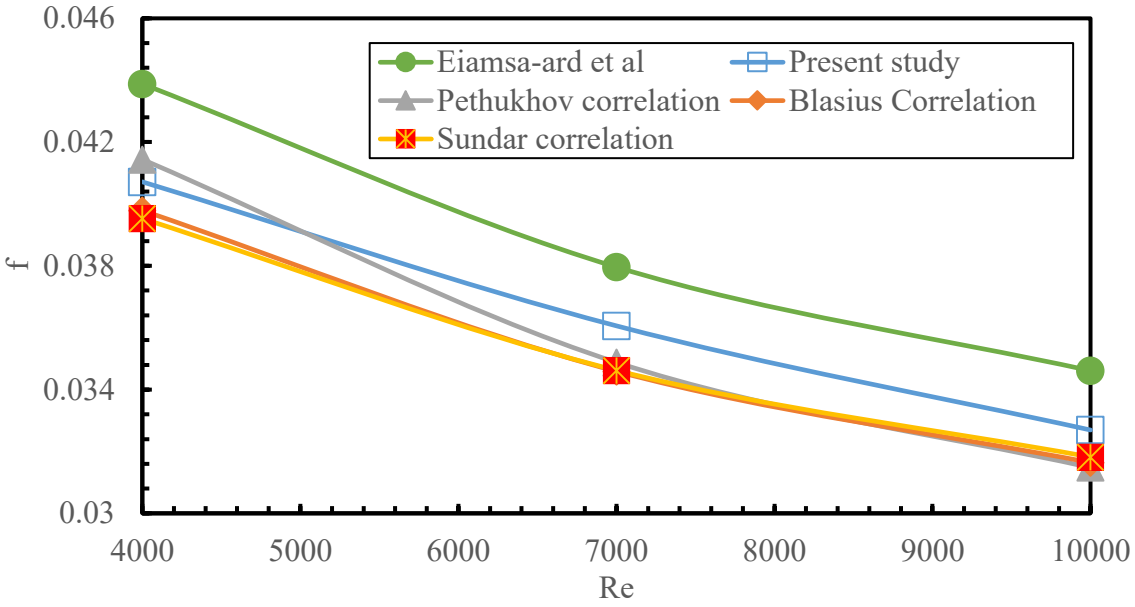

Figure 4.11: Validation of friction factor.

Figures 4.10 & 4.11 demonstrate that the CFD and empirical calculations for the Nusselt number (Nu) and friction factor (fr) exhibit agreement. The average standard deviation values, ranging from 2.199% to 7.326% for the Nusselt number and from 1.78% to 7.213% for the friction factor, were obtained from the correlations proposed by Petukhovs, Sundar & Blasisu, and Eiamsa-ard et al [34]. Therefore, it can be confidently concluded that the numerical model used in this study falls within an acceptable range of accuracy.

CHAPTER 5

RESULT AND DISCUSSION

In this section, the CFD analysis includes three major parts. Part 1: The distribution of heat flux in the absorber tube. Part 2: is the discussion of the structure of fluid flow including the result of the velocity, temperature, and pressure distribution in the PTSC. Part 3: is the result illustration of the thermal performance analysis of the heat transfer enhancement, the Nusselt number, the friction factor and the thermal performance factor.

5.1 The distribution of heat flux around the absorber tube

In this section, the results of the distribution of heat flux around the PTSC module's absorber tube are shown. Tonatiuh, MATLAB 2D discretization method, and ANSYS Fluent are used to find the findings. In this analysis, the variables "sigmaSlope" and "m_sigmaSlope" are set to a constant value of 2, representing the imperfections of the optical surfaces. Figure 5.1 shows the distribution of the heat flux surrounding the absorber tube PTSC module with a 0° angle of incidence.

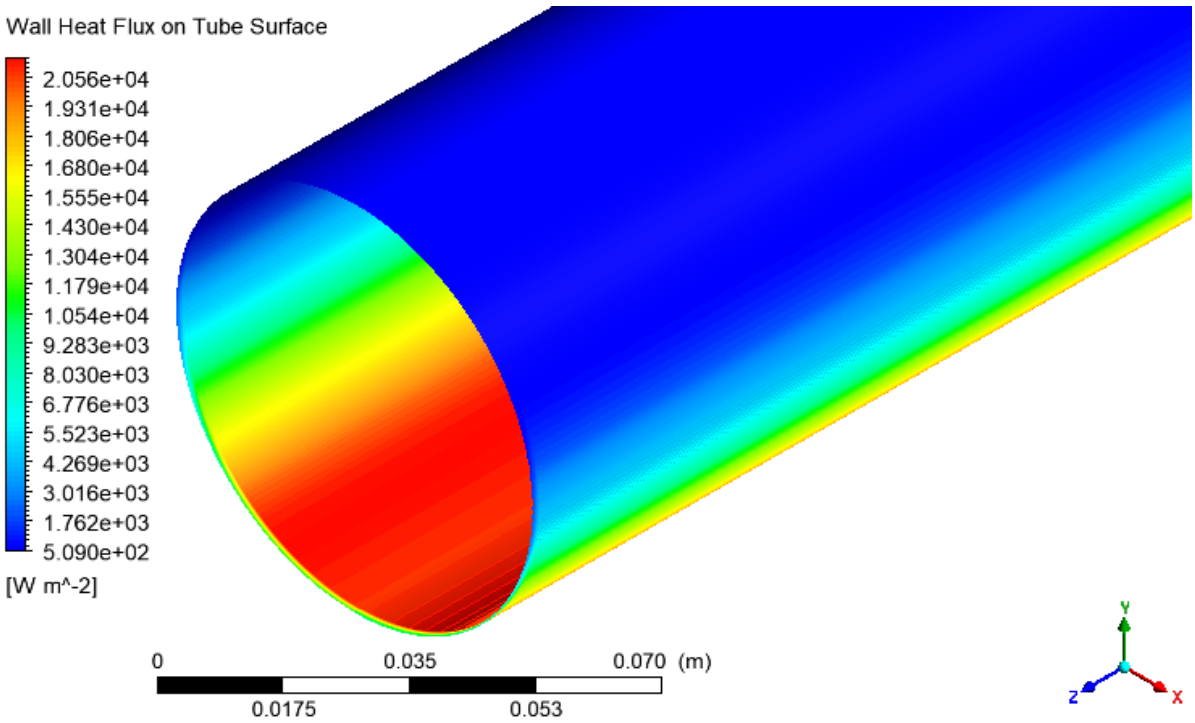

Figure 5.1: The distribution of heat flux in the absorber tube.

Figure 5.2 shows the distribution of heat flux for a 0° angle of incidence around the absorber tube and view coming from the +x direction.

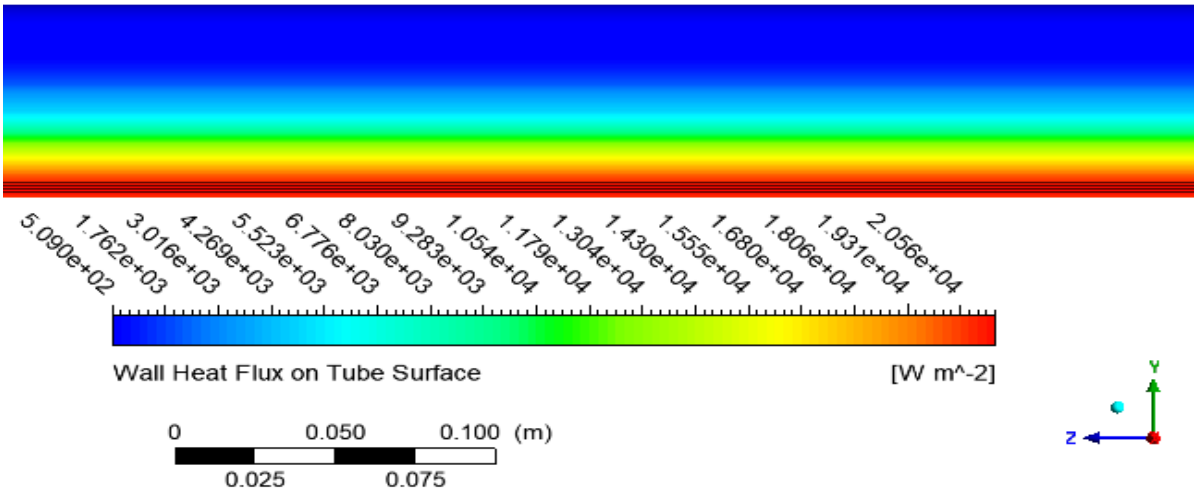

Figure 5.2: At zero degree angle of incidence the distribution of heat flux in the absorber.

It is possible to state that the heat flux profile virtually stays the same in the axial direction or z-direction. Due to the analysis's inclusion of optical imperfections, there are extremely minor alterations. Around the absorber tube of the PTSC module, the distribution of heat flux is shown in Figure 5.3 at a cross-section of z = 7.7 m.

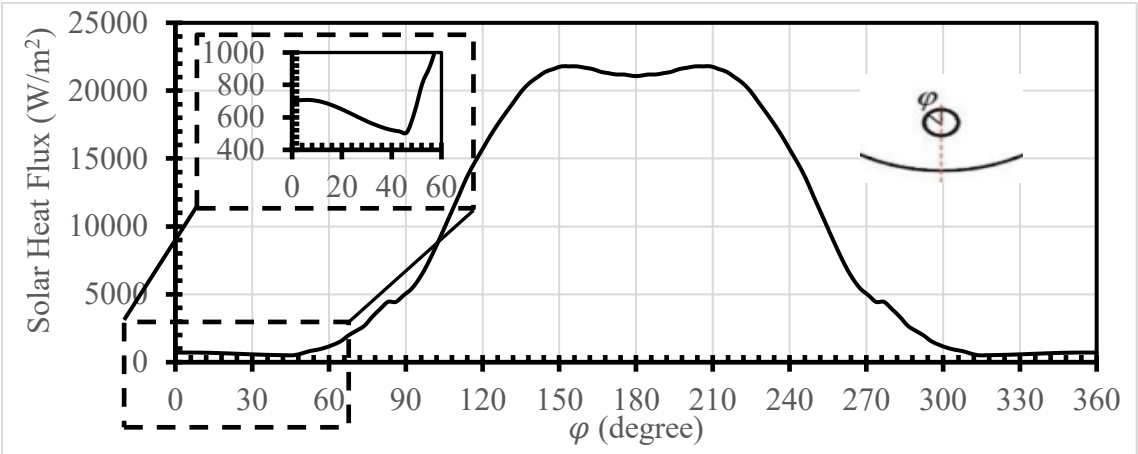

Figure 5.3: The distribution of heat flux at a cross-section of $z = 7.7\ m$ around absorber tube.

5.2 The structure of the fluid flow

5.2.1 The flow field velocity

We are particularly interested in the area where fluid is transported from one PTC line to another at high fluid temperatures. Fluid has fully developed temperature and velocity profiles when it is moved from one PTC line to another. As a result, fully formed temperature and velocity profiles are used to evaluate various tube geometries. To acquire fully developed temperature and velocity

profiles, it is discovered that a typical absorber tube with a length of 7.8 m is used [24]. Figure 5.4 & 5.5 shows the velocity profile and the local convective heat transfer coefficient at the Reynolds number of Re=4000. We can observe that the fully developed region occurs after z = 0.6 m. The fully developed entrance length was also given by Sokhansefat et al. [21] 10*D = 0.66 m. Therefore, if the flow is thermally fully developed, the local heat transfer coefficient along a line should become constant after a point [3].

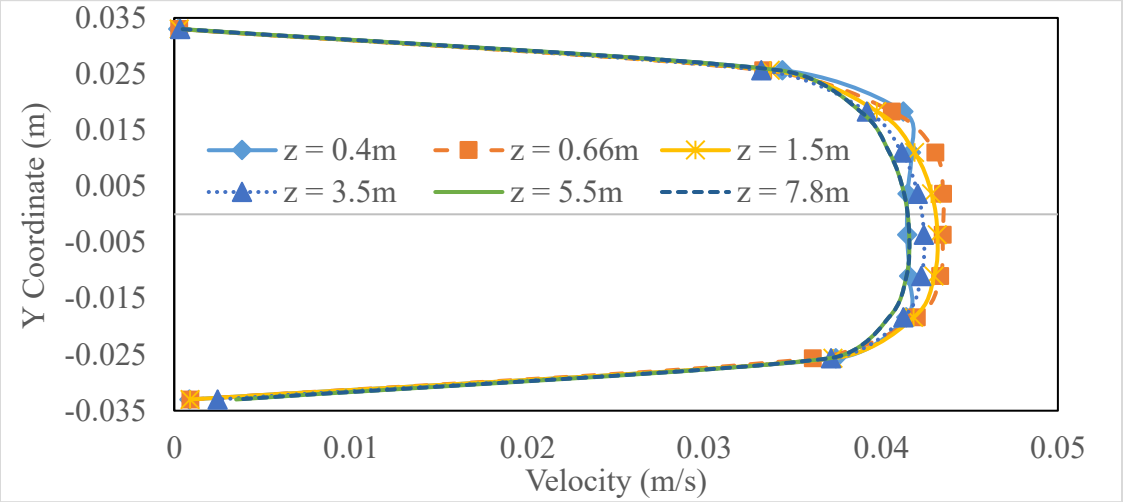

Figure 5.4: At different z-locations of the velocity profile.

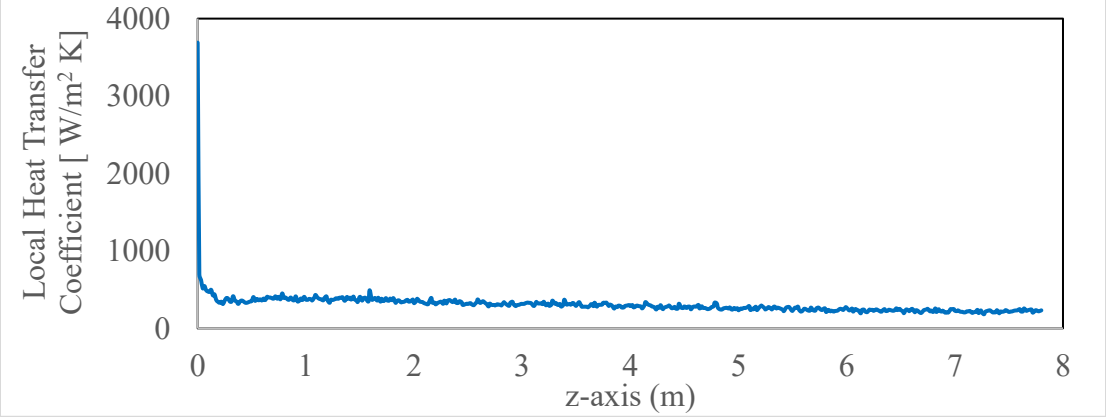

Figure 5.5: Local heat transfer coefficient along the absorber tube inner surface.

As shown in Figure 5.6 the fluid flow velocity contours in the plain tube insert with twisted tape and perforated plate form swirl around the twisted tape in the main flow region. The exit fluid velocity increases as the twisted tape ratio, and pitch ratio of the perforated plate are reduced. The existence of these swirls assists in the disruption of the boundary region and the fluid mixing from the bottom heated half section of the receiver tube with fluid from the top half section of the receiver tube receiver mainly solar radiation from the sun.

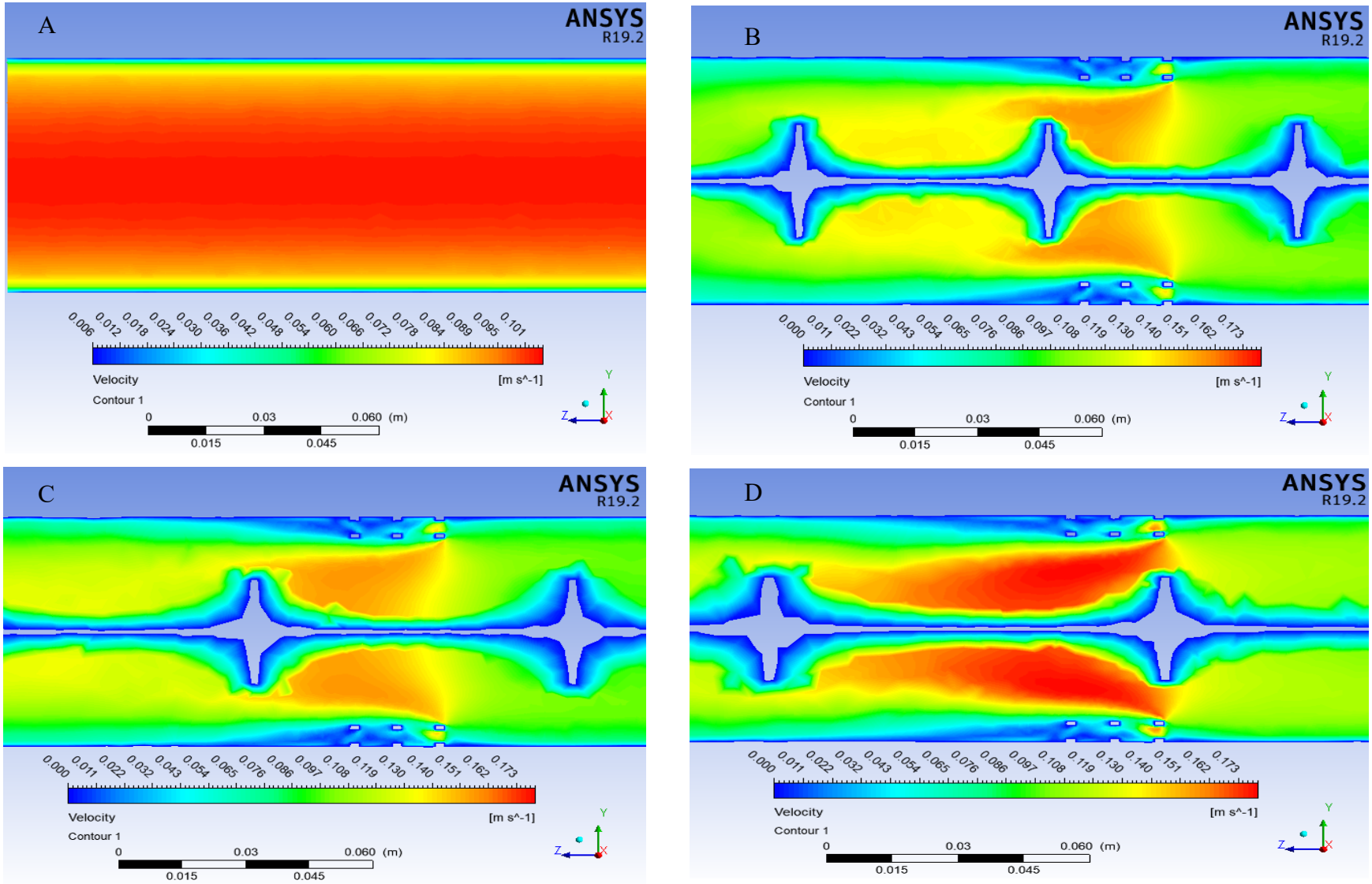

Figure 5.6: Velocity contours of the (A) PT, (B), PT with Tr=4 & 8-Turbulator (C), PT with Tr=5 & 8-Turbulator (D), PT with Tr=6 & 8-Turbulator at $\phi = 0\%$ & $Re = 10000$.

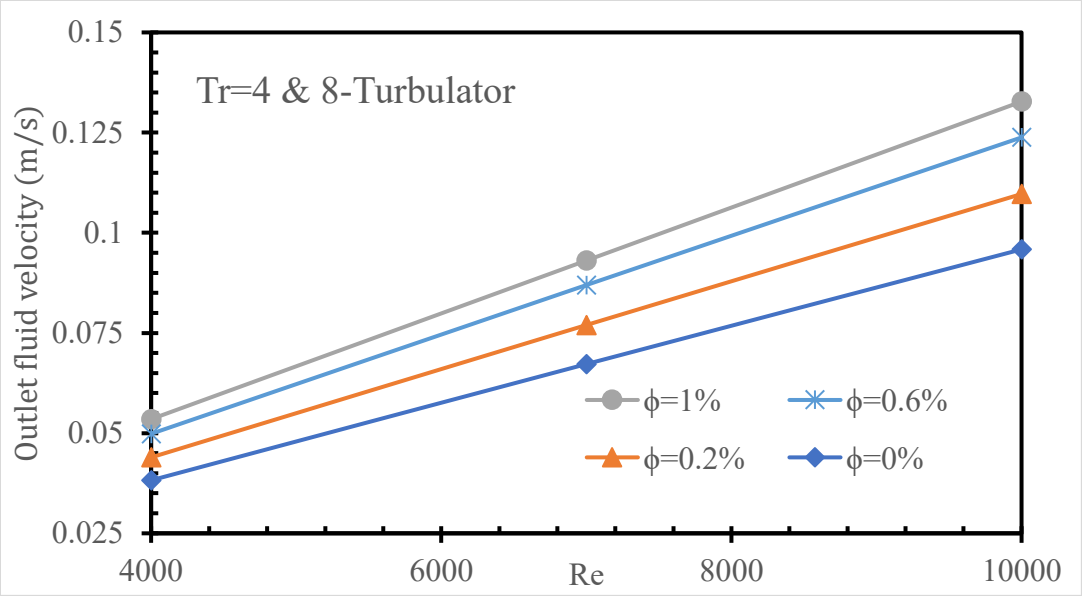

Figure 5.7: Reynolds number vs. outlet fluid velocity.

As shown in Figure 5.7 the outlet fluid velocity is directly proportional to the Reynolds number. In addition to this as we increase the concentration ratio of the nanofluid the outlet fluid velocity of the system increases. As shown in Table 5.1 the outlet profile of the outlet fluid velocity.

Table 5.1: Outlet fluid velocity at $\phi = 1\%$ and $8 - \text{Turbulator}$

Re	Tr=4	Tr=5	Tr=6
Re=4000	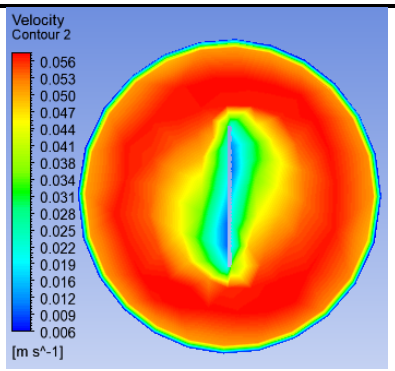	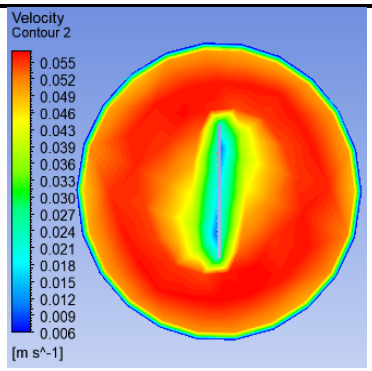	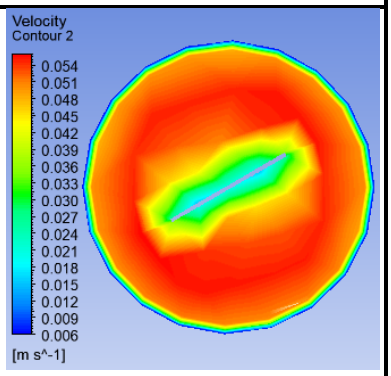
Re=10000	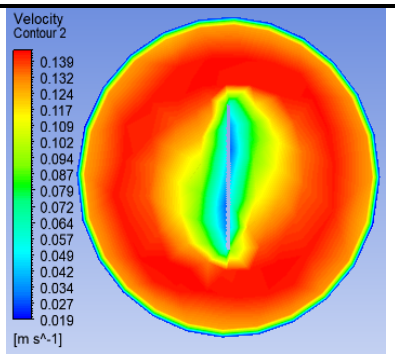	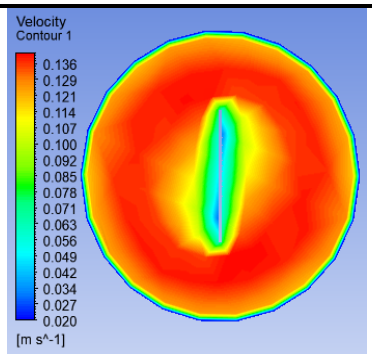	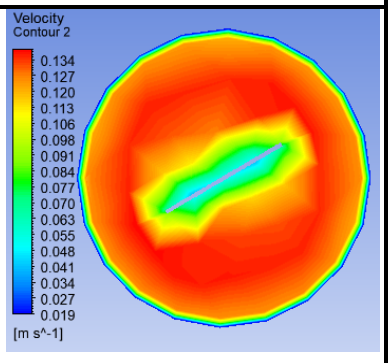

5.2.2 The flow field temperature

The temperature distribution inside the absorber tube is impacted by the use of twisted tape and perforated plate inserts, which enhance fluid mixing. As shown in Figure 5.8 the temperature difference of the fluid is inversely proportional to the Reynolds number. In addition to this as we increase the concentration ratio of the nanofluid the temperature difference of the system decreases. Incorporating twisted tape and perforated plate inserts with nanofluid leads to a more uniform distribution of temperature within the receiver tube.

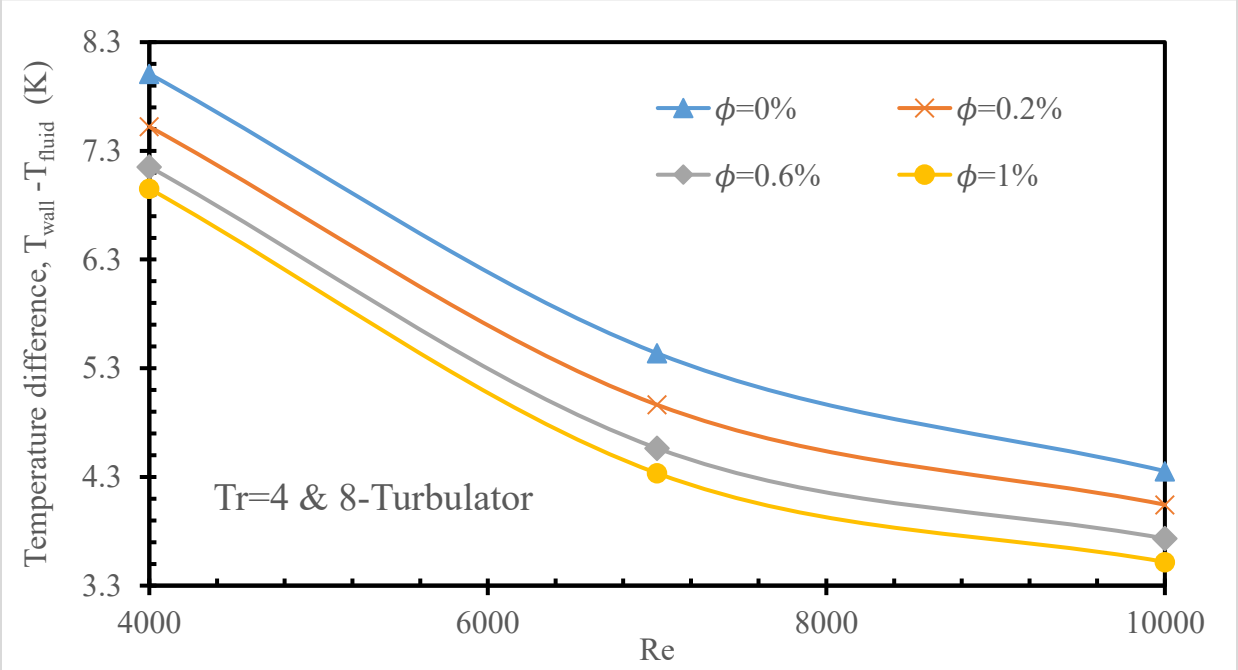

Figure 5.8: Reynolds number vs. temperature difference.

Table 5.2 demonstrates that the use of these inserts with nanofluids enhances the temperature distribution in the absorber tube. This improved temperature distribution enhances the heat transfer performance and subsequently reduces the circumferential temperature variations in the receiver tube. As shown in Figure 5.9 the maximum temperature lies on the bottom of the receiver tube and also the fluid temperature is increased as the tube length increases. The temperature contours show improved heat transfer in the areas where the fluid interacts with the turbulators and changes the direction of the velocity vectors.

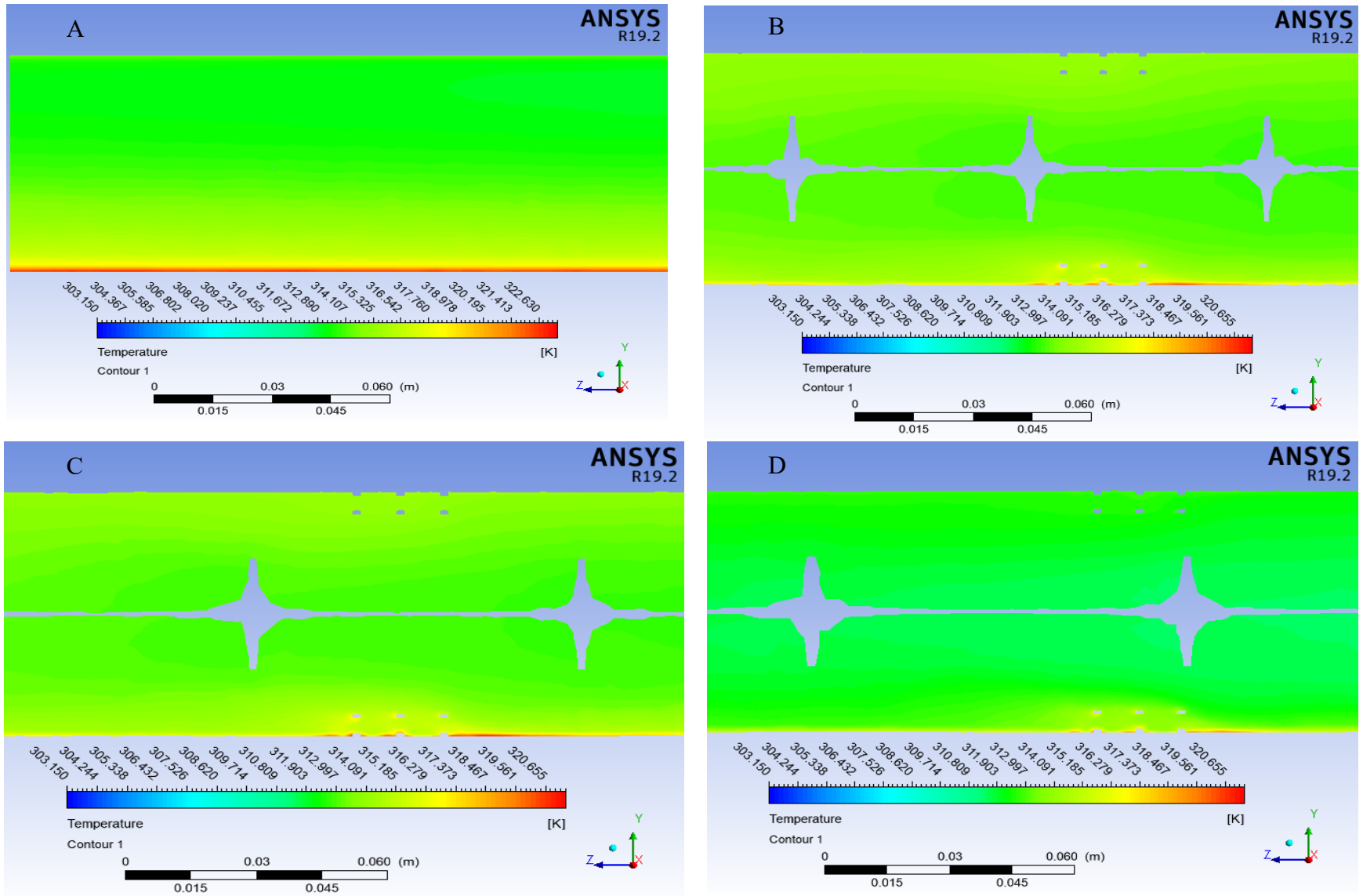

Figure 5.9: Temperature contours in the (A), PT (B), PT with Tr=4 & 8-Turbulator (C), PT with Tr=5 & 8-Turbulator (D), PT with Tr=6 & 8-Turbulator at $\phi = 0\%$ & $Re = 10000$

Table 5.2: Outlet fluid temperature at $\phi = 1\%$ and $8 -$ Turbulator

Re	Tr=4	Tr=5	Tr=6
Re=4000	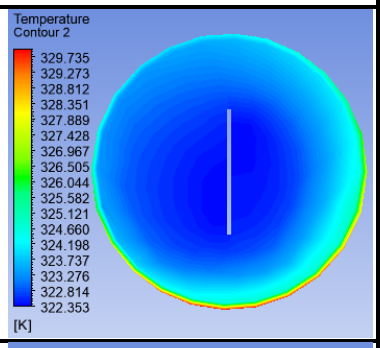	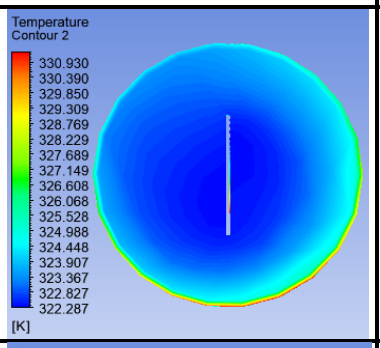	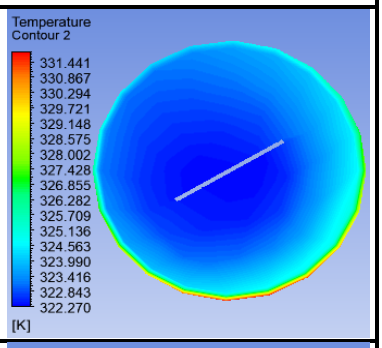
Re=10000	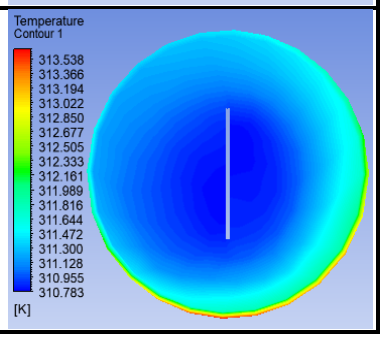	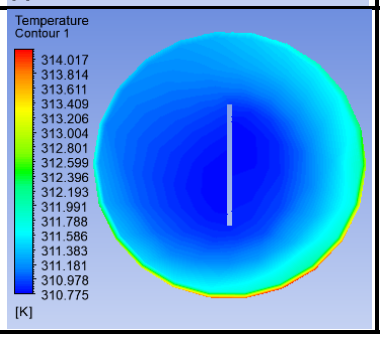	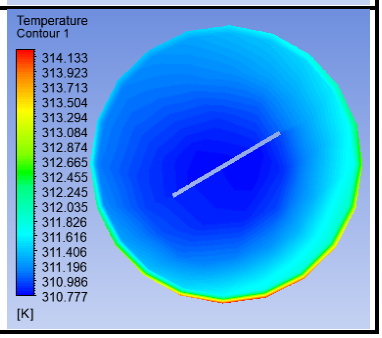

5.2.3 The pressure drop

As shown in Figure 5.10 the pressure drop varies depending on the twisted tape ratio, perforated plate with Reynolds number, and nanofluid concentration ratio. The tubes with compound devices have a greater pressure drop than the simple tube at a given Reynolds number. This is due to the fluid's dynamic pressure dissipating as a result of the interactions between three factors: (1) the flow blockage generated by the perforated plate and twisted tape, (2) the reversal, swirl flows, and separation caused by the insertion, and (3) the expansion of the fluid flow interface region.

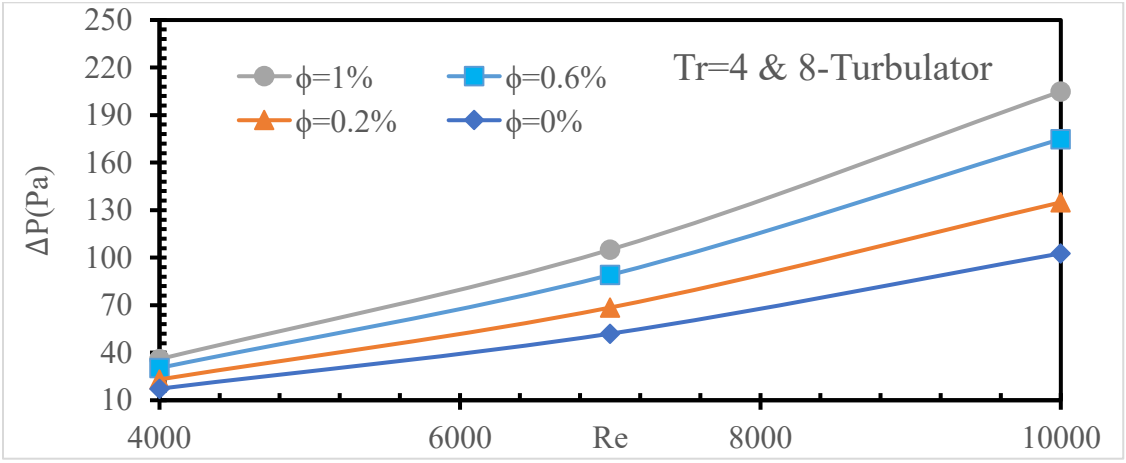

Figure 5.10: Reynolds number vs. Pressure drop of the fluid.

As shown in Figure 5.10 the pressure drop of the fluid is directly proportional to the Reynolds number. Furthermore, the pressure drop of the fluid increases concurrently with the increase in the nanofluid's concentration ratio. As shown in Table 5.3 the pressure drops at the inlet section of the fluid domain.

Table 5.3: Pressure field at the inlet section of $\phi = 1\%$ and $8 - \text{Turbulator}$

Re	Tr=4	Tr=5	Tr=6
Re=4000	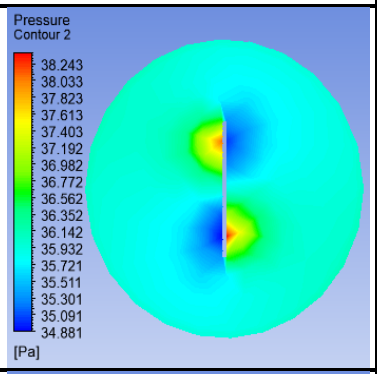	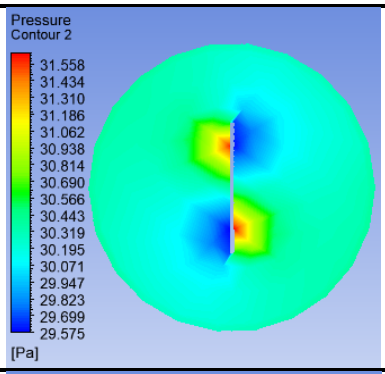	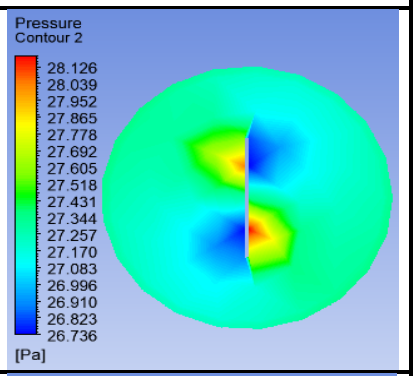
Re=10000	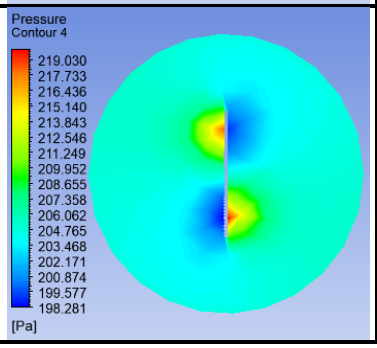	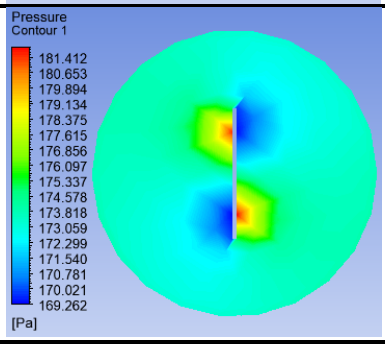	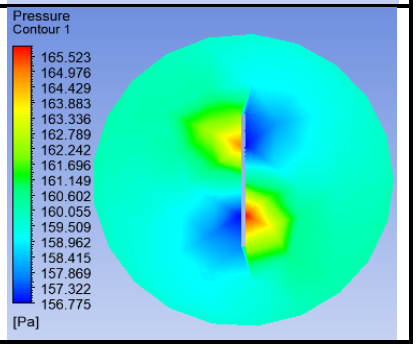

5.3 Thermal performance analysis

5.3.1 Heat transfer coefficient

CFD simulations were run for nanofluids with Reynolds numbers ranging from 4000 to 10000 [34], [50], [51]. The majority of studies have shown that the Reynolds number affects the heat transfer of nanofluids, thus the current data is also displayed similarly in Figure 5.11 by computing the (h_{nf}) from Eq. (4.17) at different Re and ϕ values. Increasing Re causes (h_{nf}) to rise. Since the CFD simulation was run in a fully developed turbulent flow, the higher the fluid's Reynolds number, the more heat is absorbed, which results in a bigger (h_{nf}) value. The combination of twisted tape and a perforated plate further improved heat transmission. At the lowest twist ratio, pitch ratio, and higher concentration ratio of nanofluid, the heat transfer is enhanced. In addition to this increasing the concentration ratio of the nanofluid more heat is transferred.

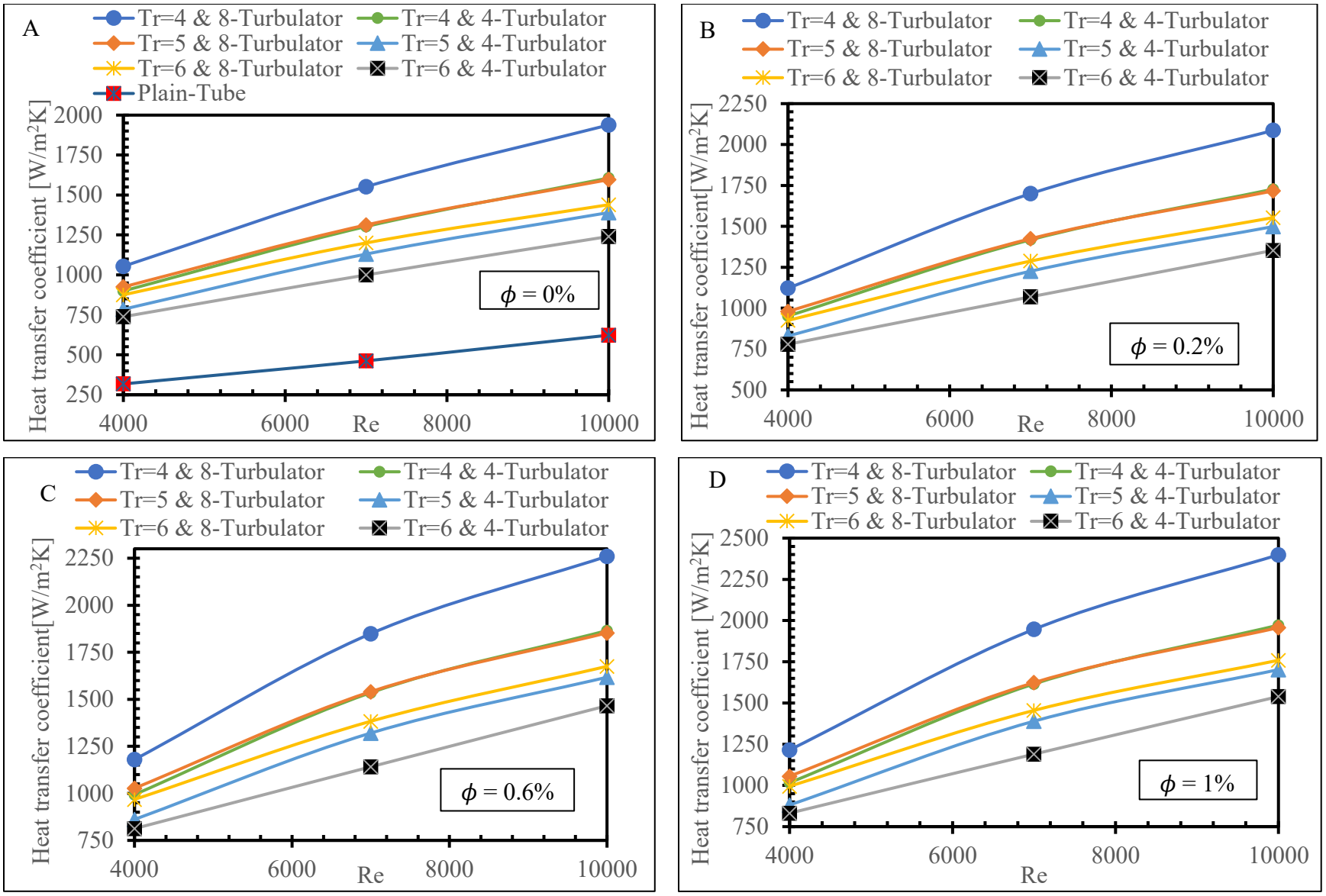

Figure 5.11: Heat transfer coefficient at a concentration ratio: (A) $\phi = 0\%$, B) $\phi = 0.2\%$, C) $\phi = 0.6\%$, and D) $\phi = 1\%$.

5.3.2 Analysis of the Nusselt number

Using the equation (4.16), the Nusselt number is the proportion of convective to conductive heat transfer at a fluid barrier under identical circumstances. In our situation, a high Nusselt number would mean that more heat was transferred from the absorber tube to the heat transfer fluid, to put it simply. The main goal of the current work is to increase the rate of heat transfer from an absorber tube utilizing twisted tapes and a perforated plate with nanofluids. Figure 5.13 shows how the Nusselt number is impacted by the twist ratio, pitch ratio, Reynolds number, and concentration ratio of the water-ZrO_2 nanofluid. As shown in Figure 5.12 (a), the minimum and maximum Nusselt numbers at the concentration ratio of $\phi = 0\%$ in the order of around 79.26 to 132.925 at Tr=6 & 4-Turbulator and 112.96 to 207.574 at Tr=4 & 8-Turbulator respectively. From Figure 5.12 (b), at $\phi = 0.2\%$ the minimum and maximum Nusselt numbers are found within the range from 83.57 to 144.93 at Tr=6 & 4-Turbulator and 120.374 to 223.411 at Tr=4 & 8-Turbulator respectively. Figure 5.12 (c) at $\phi = 0.6\%$ shows the Nusselt number of the minimum and maximum values around 86.99 to 156.93 at Tr=6 & 4-Turbulator and 126.517 to 242.019 at Tr=4 & 8-Turbulator respectively. Figure 5.12 (d) at $\phi = 1\%$ shows that the minimum and maximum Nusselt numbers are around 89.06 to 164.79 at Tr=6 & 4-Turbulator and 130.11 to 253.836 at Tr=4 & 8-Turbulator respectively.

Thus, it emerged that raising the concentration ratio of nanofluid, lowering the twisted tape ratio, and using the lowest pitch ratio of the turbulators all perform better enhancements of heat transfer rate. This is due to the lower value of pitch ratio resulting in more fluid obstructions and blockages and because closely spaced perforated plate impact on jets have higher frequency and dominance. Additionally, it can be deduced that as the number of perforated plates (turbulators) rises, so does the Nusselt number.

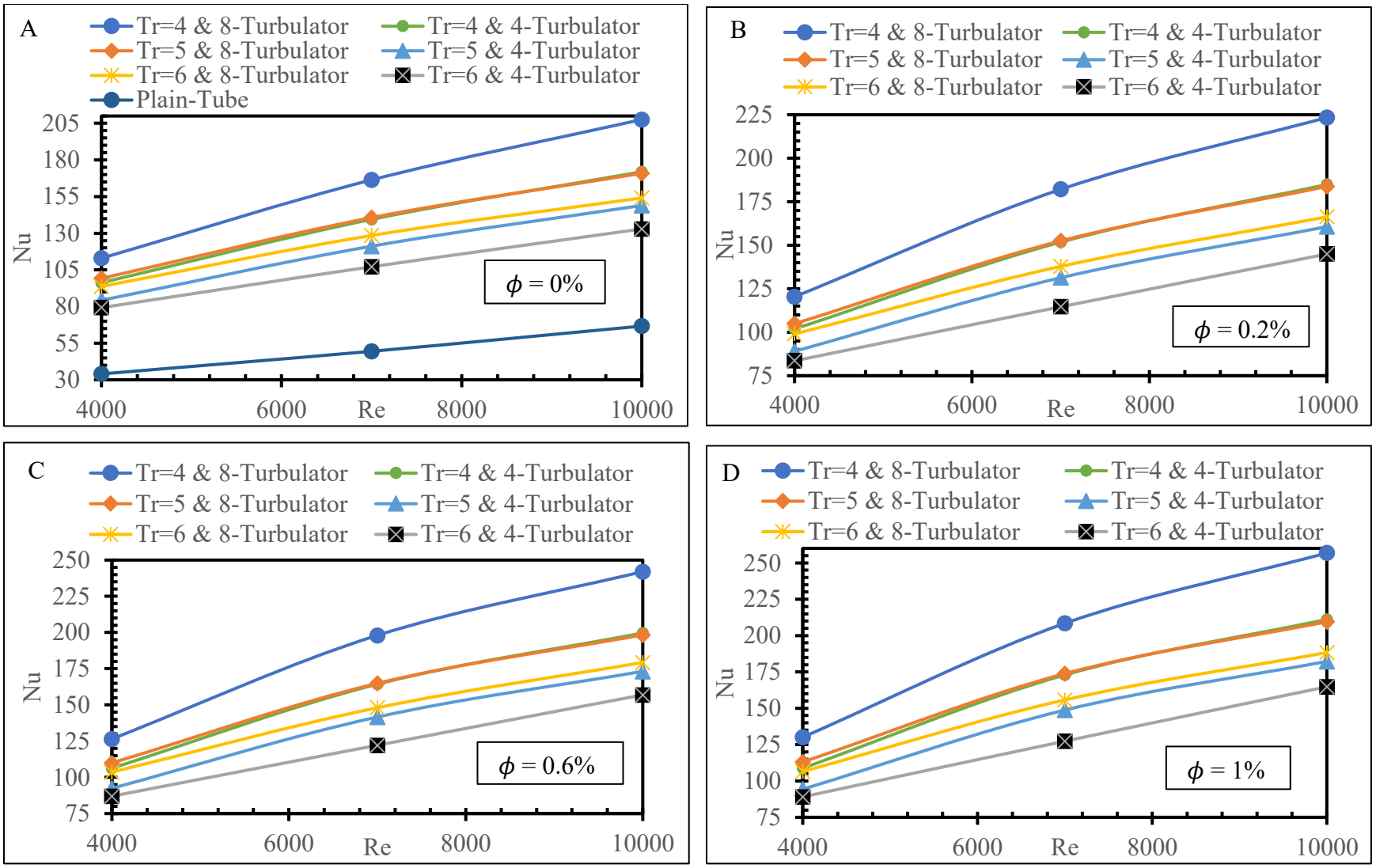

Figure 5.12: Reynolds number vs. Nusselt number variation for TT and PP insert at a concentration ratio of (A) $\phi = 0\%$, (B) $\phi = 0.2\%$, C) $\phi = 0.6\%$ and (D) $\phi = 1\%$.

The ratio of the Nusselt number (Nu/Nup) is calculated as the ratio of the enhanced Nusselt number to that of the PT Nusselt number and this is represented as a function of Reynolds in Figure 5.13 for concentration ratio values of $\phi = 0\%, 0.2\%, 0.6\%$ & 1% respectively. For lower Reynolds numbers, the heat transfer improvement for simple tubes is more prominent. Figure 5.13 (a) at $\phi = 0\%$ depicted that the ratio of Nusselt number (Nu/Nup) lowest and highest value ranges from 1.99 to 2.33 at Tr=6 & 4-Turbulator and 3.11 to 3.36 at Tr=4 & 8-Turbulator respectively. Figure 5.13 (b) at $\phi = 0.2\%$ depicted that the ratio of Nusselt number (Nu/Nup) lowest and highest value ranges from 2.17 to 2.45 at Tr=6 & 4-Turbulator and 3.35 to 3.68 at Tr=4 & 8-Turbulator respectively. Figure 5.13 (c) at $\phi = 0.6\%$ shows that the ratio of Nusselt number (Nu/Nup) lowest and highest Nusselt value ranges from 2.35 to 2.55 at Tr=6 & 4-Turbulator and 3.63 to 4.004 at Tr=4 & 8-Turbulator respectively. Figure 5.13 (d) at $\phi = 1\%$ shows that the ratio of Nusselt number (Nu/Nup) lowest and highest value ranges from 2.47 to 2.62 at Tr=6 & 4-Turbulator and 3.82 to 4.214 at Tr=4 & 8-Turbulator respectively.

It can be shown that when the Reynolds number increases, the value of the Nusselt number ratio tends to fall. This shows that the heat transfer enhancement is more effective at low Reynolds numbers. This is easily clarified by the fact that the thermal barrier is thicker at lower Reynolds numbers, making the perforated plate and twisted tape insert's disruption of the boundary more obvious. All examples have Nusselt number ratio values that are higher than unity. This shows that employing tubes with perforated plates and twisted tape placed over the plain tube has a benefit.

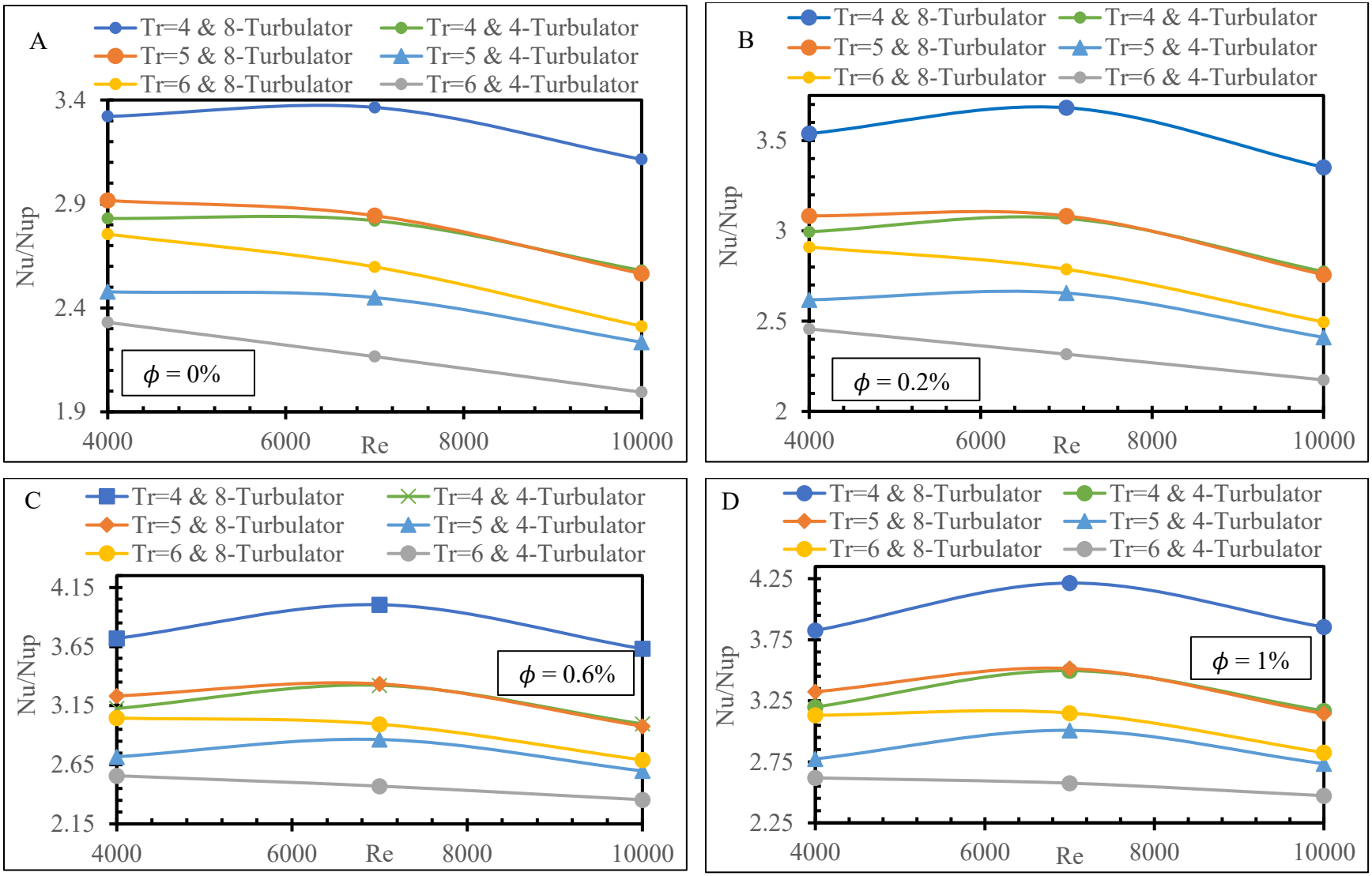

Figure 5.13: Reynolds number vs. the Nusselt number ratio of variation of TT and PP insert at a concentration of (A) ϕ = 0%, (B) ϕ = 0.2%, C) ϕ = 0.6% and (D) ϕ = 1%.

5.3.3 Analysis of friction factor

Equation (4.19) illustrates that interactions between the fluid and the absorber cause the pressure drop of the HTF in the tube to depend on the friction factor. Figure 5.14 shows how the Reynolds number affects the friction factor as a function of geometrical factors. Figure 5.14 (a) at $\phi = 0\%$ shows that the minimum and maximum friction factor values are in the order of 0.13 to 0.133 at Tr=6 & 4-Turbulator and 0.215 to 0.226 Tr=4 & 8-Turbulator respectively. Figure 5.14 (b) at $\phi = 0.2\%$ observed that the minimum and maximum friction factor values are in the order of 0.13 to 0.138 at Tr=6 & 4-Turbulator and 0.216 to 0.231 Tr=4 & 8-Turbulator respectively. Figure 5.14 (c) at $\phi = 0.6\%$ depicted that the minimum and maximum friction factor values are in the order of 0.133 to 0.144 at Tr=6 & 4-Turbulator and 0.22 to 0.238 Tr=4 & 8-Turbulator respectively. Figure 5.14 (d) at $\phi = 1\%$ observed that the minimum and maximum friction factor values are in the order of 0.136 to 0.149 at Tr=6 & 4-Turbulator and 0.224 to 0.246 Tr=4 & 8-Turbulator respectively. It was observed that the friction factor values increase with an increment in the concentration ratio of nanofluid, decrement in the twisted tape ratio, and pitch ratio between the turbulators. This is a result of the fluid's dynamic pressure dissipating owing to the combined effects of the devices' separation swirl flows, flow blockage from twisted tape and perforated plate when the flow is reversed, and increased flow contact area. Because of the large flow blockage, the friction factor is highest for smaller twist ratio values and decreases significantly as the twist ratio value increases.

Figure 5.15 describes the variation of the Reynolds numbers with the friction factor ratio (f/fp). Figure 5.15 (a) at $\phi = 0\%$ shows that the minimum and maximum friction factor ratio (f/fp) values are in the order of 3.28 to 3.98 at Tr=6 & 4-Turbulator and 5.56 to 6.58 at Tr=4 & 8-Turbulator respectively. In Figure 5.15 (b) at $\phi = 0.2\%$ observed that the minimum and maximum friction factor ratio (f/fp) values are in the order of 3.41 to 3.99 at Tr=6 & 4-Turbulator and 5.68 to 6.61 at Tr=4 & 8-Turbulator respectively. Figure 5.15 (c) at $\phi = 0.6\%$ depicted that the minimum and maximum friction factor ratio (f/fp) values are in the order of 3.54 to 4.07 at Tr=6 & 4-Turbulator and 5.86 to 6.73 at Tr=4 & 8-Turbulator respectively. Figure 5.15 (d) at $\phi = 1\%$ observed that the minimum and maximum friction factor ratio (f/fp) values are in the order of 3.66 to 4.17 at Tr=6 & 4-Turbulator and 6.04 to 6.87 at Tr=4 & 8-Turbulator respectively.

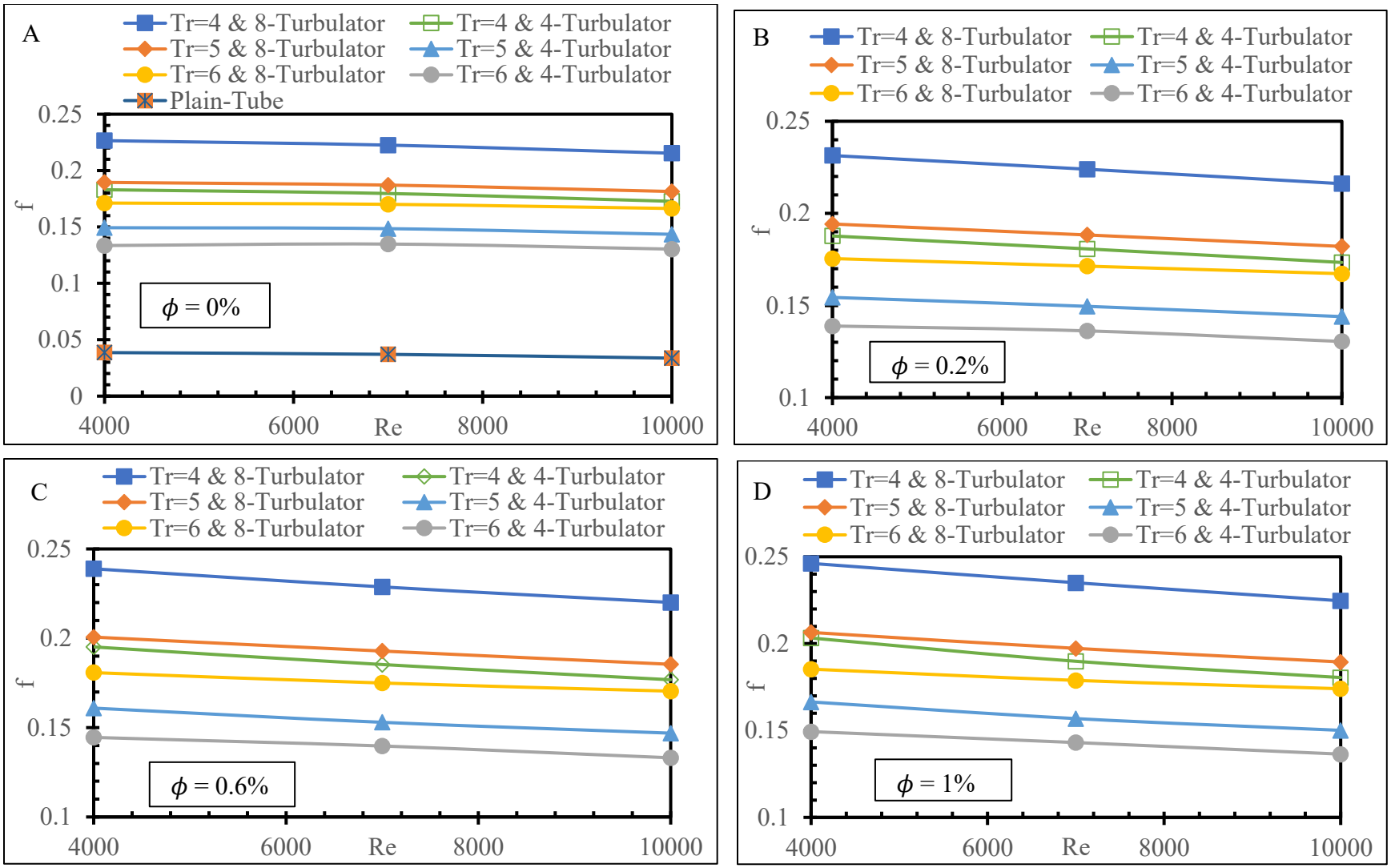

Figure 5.14: Reynolds number vs friction factor variation of TT and PP insert at a concentration ratio of (A) ϕ = 0%, (B) ϕ = 0.2%, C) ϕ = 0.6% and (D) ϕ = 1%.

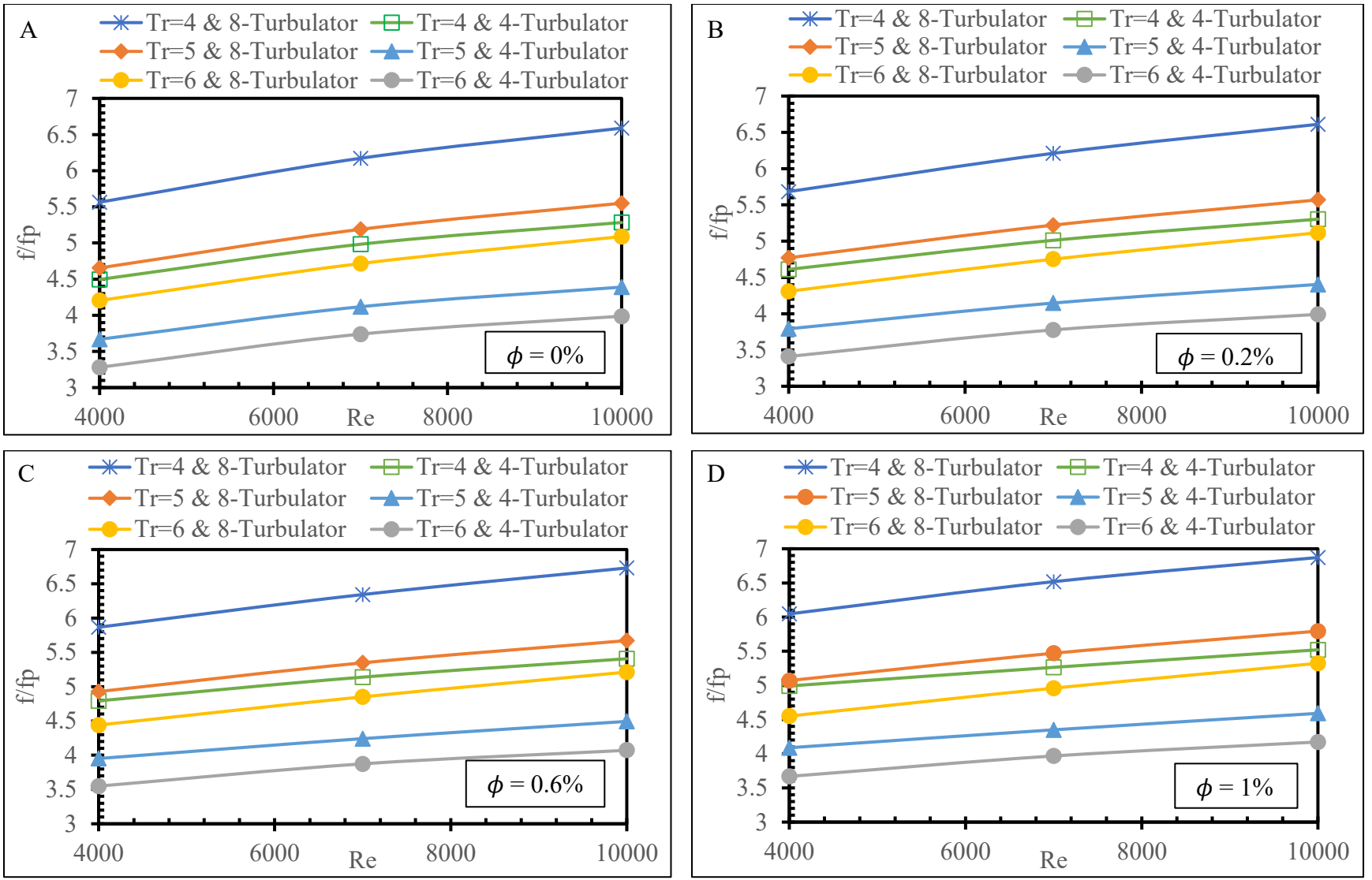

Figure 5.15: Reynolds number vs friction factor ratio of variation of TT and PP insert at a concentration ratio of (A) ϕ = 0%, (B) ϕ = 0.2%, C) ϕ = 0.6% and (D) ϕ = 1%.

It was found that as the Reynolds number and the nanofluid concentration ratio increased, correspondingly increased the friction factor ratio. The friction factor also increases at the lowest twisted tape ratio and lowest pitch ratio of the turbulators.

5.3.4 Analysis of thermal performance factor (PEC I)

The most accurate measure of how well the PTR improves heat transport in both this study and all other works of research on related subjects is the thermal performance factor (η). It is undesirable to exclusively utilize insert geometries with the highest thermal performance factor since there is a substantial rise in the values of heat transmission and friction factor for different insert geometries. Here, the emphasis is mostly on how different insert geometries affect the thermal performance factor. With an increase in Reynolds number, thermal performance factor values fall. With an increase in the nanofluid's concentration ratio, the value of the thermal performance factor rises.

From Figure 5.16 (a) at $\phi = 0\%$ It was observed that the minimum and maximum values of thermal performance factors are in the order of 1.257 to 1.568 at Tr=6 & 4-Turbulator and 1.66 to 1.87 at Tr=4 & 8-Turbulator respectively. Figure 5.16 (b) at $\phi = 0.2\%$ depicted that the minimum and maximum values of thermal performance factors are in the order of 1.37 to 1.63 at Tr=6 & 4-Turbulator and 1.78 to 2.00 at Tr=4 & 8-Turbulator respectively. Figure 5.16 (c) at $\phi = 0.6\%$ shows that the minimum and maximum values of thermal performance factors are in the order of 1.47 to 1.67 at Tr=6 & 4-Turbulator and 1.92 to 2.16 at Tr=4 & 8-Turbulator respectively. Figure 5.16 (d) at $\phi = 1\%$ shows that the minimum and maximum values of thermal performance factors are in the order of 1.536 to 1.697 at Tr=6 & 4-Turbulator and 2.027 to 2.256 at Tr=4 & 8-Turbulator respectively.

Twisted tapes with more turbulators were employed to provide the highest level of thermal performance. This has accumulated as a result of the expansion of the thermal performance factor area and the intensification of the flow's turbulence, which has improved fluid mixing between the tube wall and core region. The maximum thermal performance factor (η) obtained over the range of 1.66 to 1.87 times the plain tube at twisted tape ratio of Tr=4 and pitch ratio of (l/D=12.73) or 8-Turbulator at a concentration of ratio of $\phi = 0\%$. Further thermal performance is raised in the range of 2.027 to 2.256 over the plain tube alone at twisted tape Tr=4&8-Turbulators at a concentration ratio $\phi = 1\%$ water-ZrO_2 nanofluid.

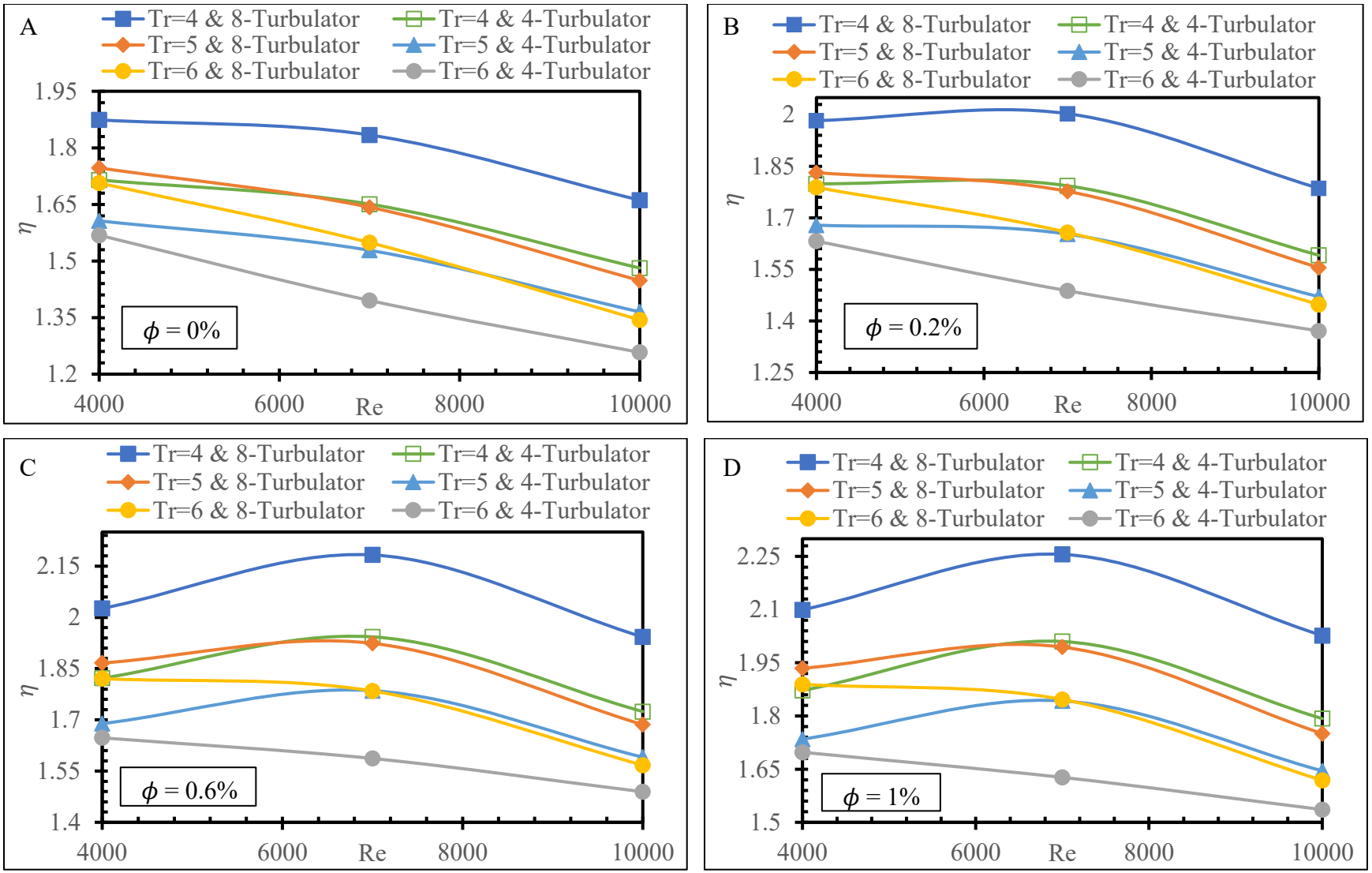

Figure 5.16: Reynolds number vs thermal performance factor variation of TT and PP insert at a concentration ratio of (A) ϕ = 0%, (B) ϕ = 0.2%, C) ϕ = 0.6% and (D) ϕ = 1%.

5.4 Comparison of thermal performance criteria

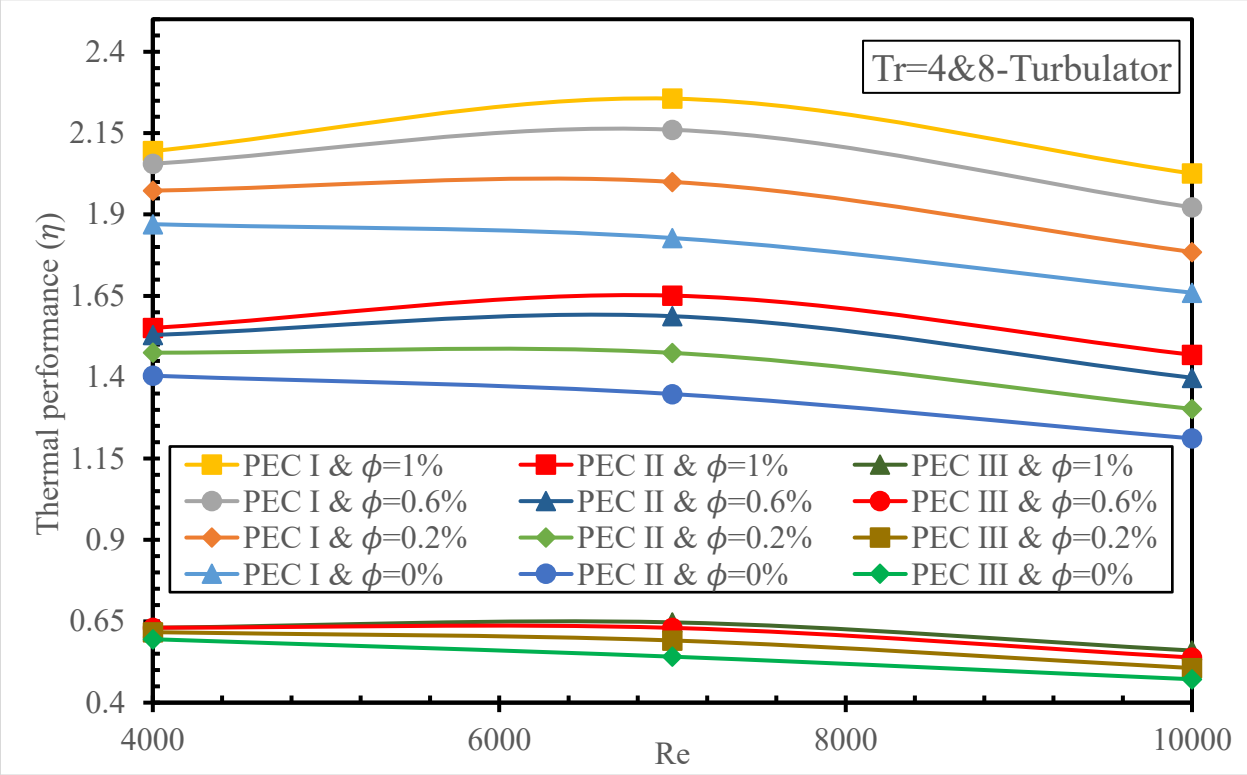

Figure 5.17: Comparison of performance enhancement criteria.

As shown in Figure 5.17 the absorber tube inserts with TT (Tr=4) & PP satisfying PEC I & PEC II. Improved heat transfer efficiency of the tube is a necessary result of an increase in the thermal performance factor. Based on this comparison, it is simple to conclude that the current study, in contrast to the majority of earlier work of a similar kind, has more substantial outcomes for heat transfer enhancement and thermal performance factor.

CHAPTER 6

CONCLUSION AND RECOMMENDATION

This section explains the thesis's conclusions and recommendations for further work.

6.1 Conclusion

The goal of this study is to improve heat transfer in parabolic trough solar collectors. The effect of various turbulators on the thermal performance of parabolic trough solar receivers is quantitatively investigated. To investigate friction factors and heat transfer inside the absorber tube inserts, comprehensive heat transfer evaluations were performed in this work. The behaviours of compound devices made up of three varying twist ratios of TT (y/W) = 4, 5, and 6, and two pitch ratios of PP of l/D = 12.78, and 22.32, and water-ZrO_2 nanofluid at concentration ratios of ϕ = 0%, 0.2%, 0.6%, and 1%, were determined. For comparison, the plain tube was also examined. The level of heat transfer improvement associated with compound devices ranges from 1.994 to 3.857 times that of a plain tube, with a pressure drop of 3.539 to 12.24 times that of a plain tube, relying on Reynolds number, twist ratio (y/W) and pitch ratio (l/D) values. Heat transfer rate increases with rising Reynolds number and decreases with decreasing pitch/twist ratio. At Reynolds number 7000, l/D = 12.78, y/w = 4, and 1% Water-ZrO_2 nanofluid concentration ratio, the highest thermal performance factor of 2.256 is achieved. According to the literature, typical values for the evaluated parameters are chosen. The following statement might be drawn from the study.

- The resulting Nusselt number and friction factor agreed well with the equation correlations of Petukhov, Dittus-Boelter, Sundar, and Blassius, as well as Eiamsa ard et al [34].
- The Nusselt number is raised while the friction factor is adversely affected by using twisted tape and perforated plate inserts in the absorber tube.
- As water-ZrO_2 nanofluids are used, heat transfer is greatly improved, resulting in the greatest thermal performance as compared to the base fluid.

6.2 Recommendation

The present work could be refined further and augmented by employing an absorber tube with a glass cover and determining the heat loss of the system. Additionally, additional simulations with more Reynolds number values and more add-up turbulators can be undertaken to verify the outcomes obtained and get a broad comprehensive idea of the effect of various variables on the thermal performance of the PTC. Another study that might be conducted is whether the improvement in thermal performance efficiency is valuable, especially when it comes to the rise in production expenses brought on by the addition of TT and PP inserts to the regular tube. Furthermore, another investigation can be conducted by reducing the pressure drop by insertion of TT and PP with nanofluid and also investigating for improvement of the efficiency of the parabolic trough collectors.

REFERENCES

[1] Kalogirou SA. *Solar energy engineering: processes and systems*. Academic press, 2013.

[2] Teferie ST. *Simulation of Parabolic Trough Concentrating Solar Power Generation System*. MSc Thesis, Addis Ababa University, 2014.

[3] Uygur S. *Detailed simulations of parabolic trough collector for investigating enhancement of heat transfer to absorber tube flow*. Master's Thesis, Middle East Technical University, 2021.

[4] Abdi A. *Performance Analysis of Parabolic Trough Solar Steam Generators: Acase of Wenji Pulp and Paper Factory*. Msc. Thesis, ASTU, 2019.

[5] Tefera MA. Electricity Production from Concentrated Solar Power and PV System in Ethiopia.

[6] Woldeyes S. Assessment of Stand-Alone Solar Photovoltaic Power Systems Performance and Reliability for Rural Electrification in Ethiopia.

[7] Messele Y, Assefa A. Thermal Analysis, Design and Experimental Investigation of Parabolic Trough Solar Collector. In: Abraham A, Krömer P, Snasel V (eds) *Afro-European Conference for Industrial Advancement*. Cham: Springer International Publishing, pp. 245–260.

[8] Mouaky A, Alami Merrouni A, Laadel NE, et al. Simulation and experimental validation of a parabolic trough plant for solar thermal applications under the semi-arid climate conditions. *Sol Energy* 2019; 194: 969–985.

[9] Vorrath S. First 160MW of huge Noor solar thermal plant connected to Moroccan grid. *RenewEconomy*, https://reneweconomy.com.au/first-160mw-of-huge-noor-solar-thermal-plant-connected-to-moroccan-grid-18132/ (2016, accessed 17 May 2023).

[10] Dirker J, izufrank123@yahoo.com, Meyer JP, et al. *Influence of Circumferential Spans of Heat Flux Distributions on Secondary Flow, Heat Transfer and Friction Factors for a Linear Focusing Solar Collector Type Absorber Tube*. Thesis, University of Pretoria, https://repository.up.ac.za/handle/2263/64173 (2017, accessed 30 May 2023).

[11] Manikandan GK, Iniyan S, Goic R. Enhancing the optical and thermal efficiency of a parabolic trough collector – A review. *Appl Energy* 2019; 235: 1524–1540.

[12] Shajahan M, Michael JJ, Arulprakasajothi M, et al. Effect of Conical Strip Inserts and ZrO2/DI-Water Nanofluid on Heat Transfer Augmentation: An Experimental Study. *Energies* 2020; 13: 4554.

[13] Olia H, Torabi M, Bahiraei M, et al. Application of nanofluids in thermal performance enhancement of parabolic trough solar collector: state-of-the-art. *Appl Sci* 2019; 9: 463.

[14] Bekele A, Alemu D, Mishra M. Large Scale Solar Water Heating Systems Analysis in Ethiopia: A Case Study Adisu Bekele, Demiss Alemu, Manish Mishra. International Journal of Sustainable Energy, Vol. 32 (4), Feb. 2013, pp. 207-228. *Int J Sustain Energy* 2013; 32: 207–228.

[15] Ethio Resource Group with Partners. Development, Ethiopian Rural Energy. Solar and Wind Energy Utilization and Project Development Scenarios (October 2007) - Google Search, https://www.google.com/search? (2007, accessed 28 January 2022).

[16] Hong K, Yang Y, Rashidi S, et al. Numerical simulations of a Cu–water nanofluid-based parabolic-trough solar collector. *J Therm Anal Calorim* 2021; 143: 4183–4195.

[17] Ghasemi SE, Ranjbar A. Effect of nanoparticles in working fluid on thermal performance of solar parabolic trough collector. *J Mol Liq* 2016; 222: 156–166.

[18] Ekiciler R, Arslan K, Turgut O, et al. Effect of hybrid nanofluid on heat transfer performance of parabolic trough solar collector receiver. *J Therm Anal Calorim* 2021; 143: 1637–1654.

[19] Okonkwo EC, Abid M, Ratlamwala TA. Numerical analysis of heat transfer enhancement in a parabolic trough collector based on geometry modifications and working fluid usage. *J Sol Energy Eng*; 140.

[20] Subramani J, Nagarajan PK, Mahian O, et al. Efficiency and heat transfer improvements in a parabolic trough solar collector using TiO2 nanofluids under turbulent flow regime. *Renew Energy* 2018; 119: 19–31.

[21] Sokhansefat T, Kasaeian AB, Kowsary F. Heat transfer enhancement in parabolic trough collector tube using Al2O3/synthetic oil nanofluid. *Renew Sustain Energy Rev* 2014; 33: 636–644.

[22] Siavashi M, Bozorg MV, Toosi MH. A numerical analysis of the effects of nanofluid and porous media utilization on the performance of parabolic trough solar collectors. *Sustain Energy Technol Assess* 2021; 45: 101179.

[23] Alnaqi AA, Alsarraf J, Al-Rashed AAAA. Hydrothermal effects of using two twisted tape inserts in a parabolic trough solar collector filled with MgO-MWCNT/thermal oil hybrid nanofluid. *Sustain Energy Technol Assess* 2021; 47: 101331.

[24] Bellos E, Tzivanidis C, Tsimpoukis D. Enhancing the performance of parabolic trough collectors using nanofluids and turbulators. *Renew Sustain Energy Rev* 2018; 91: 358–375.

[25] Bellos E, Daniil I, Tzivanidis C. A cylindrical insert for parabolic trough solar collector. *Int J Numer Methods Heat Fluid Flow*.

[26] Reddy KS, Satyanarayana GV. Numerical study of porous finned receiver for solar parabolic trough concentrator. *Eng Appl Comput Fluid Mech* 2008; 2: 172–184.

[27] Shahzad Nazir M, Shahsavar A, Afrand M, et al. A comprehensive review of parabolic trough solar collectors equipped with turbulators and numerical evaluation of hydrothermal performance of a novel model. *Sustain Energy Technol Assess* 2021; 45: 101103.

[28] Reddy KS, Kumar KR, Satyanarayana GV. Numerical investigation of energy-efficient receiver for solar parabolic trough concentrator. *Heat Transf Eng* 2008; 29: 961–972.

[29] Soo Too YC, Benito R. Enhancing heat transfer in air tubular absorbers for concentrated solar thermal applications. *Appl Therm Eng* 2013; 50: 1076–1083.

[30] Bellos E, Tzivanidis C, Antonopoulos KA, et al. Thermal enhancement of solar parabolic trough collectors by using nanofluids and converging-diverging absorber tube. *Renew Energy* 2016; 94: 213–222.

[31] Bellos E, Tzivanidis C, Tsimpoukis D. Multi-criteria evaluation of parabolic trough collector with internally finned absorbers. *Appl Energy* 2017; 205: 540–561.

[32] Ahmed KA, Natarajan E. Thermal performance enhancement in a parabolic trough receiver tube with internal toroidal rings: A numerical investigation. *Appl Therm Eng* 2019; 162: 114224.

[33] Shaker B, Gholinia M, Pourfallah M, et al. CFD analysis of Al2O3-syltherm oil Nanofluid on parabolic trough solar collector with a new flange-shaped turbulator model. *Theor Appl Mech Lett* 2022; 12: 100323.

[34] Eiamsa-ard S, Kongkaitpaiboon V, Nanan K. Thermohydraulics of turbulent flow through heat exchanger tubes fitted with circular-rings and twisted tapes. *Chin J Chem Eng* 2013; 21: 585–593.

[35] He W, Toghraie D, Lotfipour A, et al. Effect of twisted-tape inserts and nanofluid on flow field and heat transfer characteristics in a tube. *Int Commun Heat Mass Transf* 2020; 110: 104440.

[36] Ravi Kumar K, Reddy KS. Effect of porous disc receiver configurations on performance of solar parabolic trough concentrator. *Heat Mass Transf* 2012; 48: 555–571.

[37] Too YCS, Benito R. Enhancing heat transfer in air tubular absorbers for concentrated solar thermal applications. *Appl Therm Eng* 2013; 50: 1076–1083.

[38] Mwesigye A, Bello-Ochende T, Meyer JP. Heat transfer and entropy generation in a parabolic trough receiver with wall-detached twisted tape inserts. *Int J Therm Sci* 2016; 99: 238–257.

[39] Ebrahim Ghasemi S, Akbar Ranjbar A. Numerical thermal study on effect of porous rings on performance of solar parabolic trough collector. *Appl Therm Eng* 2017; 118: 807–816.

[40] Shahsavar Goldanlou A. Energy and exergy analysis of using turbulator in a parabolic trough solar collector filled with mesoporous silica modified with copper nanoparticles hybrid nanofluid, https://core.ac.uk/reader/328828732 (2020, accessed 11 February 2022).

[41] Al-Rashed AAAA, Alnaqi AA, Alsarraf J. Thermo-hydraulic and economic performance of a parabolic trough solar collector equipped with finned rod turbulator and filled with oil-based hybrid nanofluid. *J Taiwan Inst Chem Eng* 2021; 124: 192–204.

[42] Mohammed HA, Vuthaluru HB, Liu S. Heat transfer augmentation of parabolic trough solar collector receiver's tube using hybrid nanofluids and conical turbulators. *J Taiwan Inst Chem Eng* 2021; 125: 215–242.

[43] Khetib Y, Sait H, Habeebullah B, et al. Numerical study of the effect of curved turbulators on the exergy efficiency of solar collector containing two-phase hybrid nanofluid. *Sustain Energy Technol Assess* 2021; 47: 101436.

[44] Yadav AS, Shrivastava V, Sharma A, et al. CFD simulation on thermo-hydraulic characteristics of a circular tube having twisted tape inserts. *Mater Today Proc* 2021; 47: 2790–2795.

[45] Ju Y, Zhu T, Mashayekhi R, et al. Evaluation of Multiple Semi-Twisted Tape Inserts in a Heat Exchanger Pipe Using Al2O3 Nanofluid. *Nanomaterials* 2021; 11: 1570.

[46] Ghasemi SE, Mohsenian S, Ranjbar AA. Numerical analysis on heat transfer of parabolic solar collector operating with nanofluid using Eulerian two-phase approach. *Numer Heat Transf Part Appl* 2021; 80: 475–484.

[47] Hasanpour A, Farhadi M, Sedighi K. A review study on twisted tape inserts on turbulent flow heat exchangers: The overall enhancement ratio criteria. *Int Commun Heat Mass Transf* 2014; 55: 53–62.

[48] Blanco MJ, Mutuberria A, Garcia P, et al. Preliminary validation of Tonatiuh. In: *SolarPACES 2009 International Conference, At Berlin (Germany)*. 2009, p. 2009.

[49] Abbas R, Montes MJ, Rovira A, et al. Parabolic trough collector or linear Fresnel collector? A comparison of optical features including thermal quality based on commercial solutions. *Sol Energy* 2016; 124: 198–215.

[50] Eiamsa-ard S, Thianpong C, Eiamsa-ard P. Turbulent heat transfer enhancement by counter/co-swirling flow in a tube fitted with twin twisted tapes. *Exp Therm Fluid Sci* 2010; 34: 53–62.

[51] Sundar LS. Experimental study on the thermophysical properties, heat transfer, thermal entropy generation and exergy efficiency of turbulent flow of ZrO2-water nanofluids. *Alex Eng J* 2023; 65: 867–885.

[52] Yılmaz İH, Mwesigye A, Göksu TT. Enhancing the overall thermal performance of a large aperture parabolic trough solar collector using wire coil inserts. *Sustain Energy Technol Assess* 2020; 39: 100696.

[53] Rago T. Numerical and Experimental Investigation of Heat Transfer Enhancement in Flat Plate Solar Collector Using Nano Fluids. 137.

[54] Yakhot V, Orszag SA, Thangam S, et al. Development of turbulence models for shear flows by a double expansion technique. *Phys Fluids Fluid Dyn* 1992; 4: 1510–1520.

[55] Chakraborty O, Das B, Gupta R, et al. Heat transfer enhancement analysis of parabolic trough collector with straight and helical absorber tube. *Therm Sci Eng Prog* 2020; 20: 100718.

[56] Bozorg MV, Doranehgard MH, Hong K, et al. CFD study of heat transfer and fluid flow in a parabolic trough solar receiver with internal annular porous structure and synthetic oil–Al2O3 nanofluid. *Renew Energy* 2020; 145: 2598–2614.

[57] Jeter SM. Calculation of the concentrated flux density distribution in parabolic trough collectors by a semifinite formulation. *Sol Energy* 1986; 37: 335–345.

[58] Farooq M, Farhan M, Ahmad G, et al. Thermal performance enhancement of nanofluids based parabolic trough solar collector (NPTSC) for sustainable environment. *Alex Eng J* 2022; 61: 8943–8953.

[59] Einstein A. Eine neue Bestimmung der Moleküldimensionen. *Ann Phys* 1906; 324: 289–306.

[60] Ghanam MS, Saad T. Hamidi, Fikrat A.K. Fattah. Performance Improvement of the Parabolic Trough Solar Collector Using Different Types of Fluids with Numerical Simulation. 2018; 26: 332–347.

[61] Maxwell JC. An Elementary Treatise on Electricity.

[62] Fattahi A. Numerical simulation of a solar collector equipped with a twisted tape and containing a hybrid nanofluid. *Sustain Energy Technol Assess* 2021; 45: 101200.

[63] Petukhov BS. Heat Transfer and Friction in Turbulent Pipe Flow with Variable Physical Properties. In: Hartnett JP, Irvine TF (eds) *Advances in Heat Transfer*. Elsevier, pp. 503–564.

[64] Dittus FW, Boelter LMK. Heat transfer in automobile radiators of the tubular type. *Int Commun Heat Mass Transf* 1985; 12: 3–22.

[65] Chaudhari SR, Maheshwari PB. Finite strip method for the analysis of diaphragm supported cylindrical shell. *Mater Today Proc* 2020; 28: 846–851.

APPENDIX

Table A 1: Solar radiation on the horizontal surface [kWh/m^2/day]

Year	Jan	Feb	Mar	Apr	May	Jun	Jul	Aug	Sep	Oct	Nov	Dec	ANN
2017	7.84	6.18	7.32	6.3	4.71	5.52	4.43	4.45	4.88	5.77	7.84	8.66	6.16
2018	8.11	7.03	5.81	4.17	5.49	4.31	3.91	4.94	5.95	5.63	6.61	8.12	5.84
2019	8.78	7.31	7.23	5.88	5.44	4.93	4.51	4.83	4.7	5.43	5.68	7.51	6.02
2020	6.58	7.37	5.65	4.9	5.98	5.31	4.08	4.18	4.87	7.12	7.62	8.12	5.98
2021	8.84	7.75	8.11	5.86	6.02	5.49	3.2	5.48	5.14	6.4	8.21	8.46	6.57
Average	8.03	7.128	6.824	5.422	5.528	5.112	4.026	4.776	5.108	6.07	7.192	8.174	6.114

Source: https://power.larc.nasa.gov/data-access-viewer

Table A 2: Thermo-physical properties of ZrO_2 nanofluids [51]

	Physical property				
ϕ	**T (°C)**	Thermal conductivity (W/m. K)	Viscosity (mPa.s)	density (kg/m^3)	Specific heat (J/kg K)
Base fluid	20	0.602	0.79	997	4178
	30	0.6165	0.58	997.5	4178
	40	0.631	0.48	995	4179
	50	0.6425	0.3	990	4180.5
	60	0.653	0.24	985	4183
0.20%	20	0.63	0.95	1006.37	4170.48
	30	0.651	0.67	1006.87	4170.48
	40	0.672	0.55	1004.37	4171.48
	50	0.687	0.34	999.38	4172.98
	60	0.71	0.27	994.39	4175.47
0.60%	20	0.648	1.06	1025.1	4155.45
	30	0.672	0.77	1025.6	4155.45
	40	0.714	0.63	1023.11	4156.45
	50	0.741	0.38	1018.14	4157.94
	60	0.763	0.3	1013.17	4160.42
1.00%	20	0.669	1.15	1043.83	4140.42
	30	0.699	0.84	1044.33	4140.42
	40	0.736	0.7	1041.85	4141.41
	50	0.781	0.43	1036.9	4142.9
	60	0.816	0.33	1031.95	4145.37

The correlations between the thermophysical characteristics of the ZrO2/water nanofluids generated are put into a multi-linear regression model and are shown below.

Thermal conductivity: $k_{nf} = 0.5349 + 0.00265T + 0.104057\phi$ ……..……..…….... (1)

Absolute viscosity: $\mu_{nf} = 1.22161 - 0.01803T + 0.19949\phi$ ……..……..…….... (2)

Density: $\rho_{nf} = 1005.43 - 0.3134T + 46.87\phi$……..……..……..……..…… (3)

Specific heat: $C_{p,nf} = 4174.72 + 0.1244T - 37.593\phi$……..……..……..…… (4)

Validity: $\phi < 1.0\%$; $T = 20 - 60℃$

A. Develop the parabola trough

It describes how to utilize Tonatiuh to build the parabolic mirror for the PTSC module. Figure A 1's tree representation of the parabolic reflector includes the surface and group nodes.

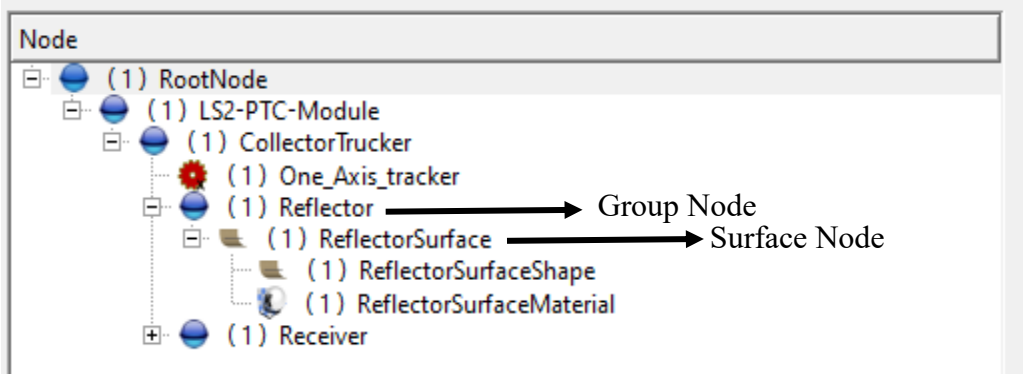

Figure A 1: The parabolic reflector's tree structure has a group and a surface node.

How to establish a surface and group node is shown in Figure A 2.

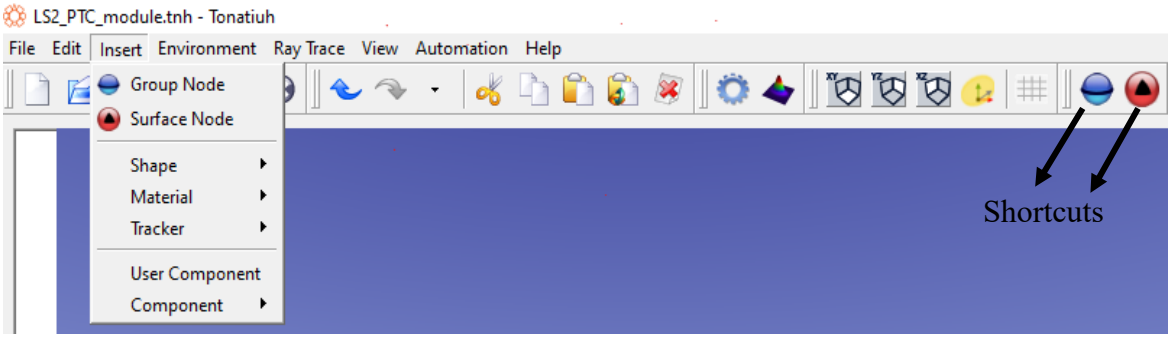

Figure A 2: Surface and group node insert section.

For The shape "Parabola trough" is selected and for the material, “Standard Specula Material" is selected. Figures A 3 and A 4 illustrate the Tonatiuh portions for inserting shape and material, consequently.

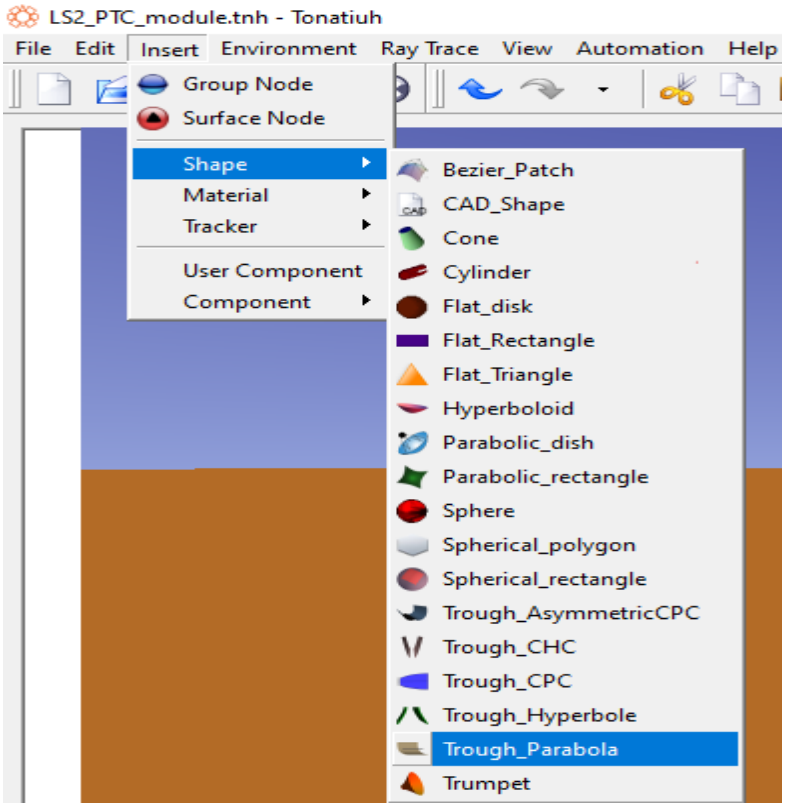

Figure A 3: The parabola trough insert section.

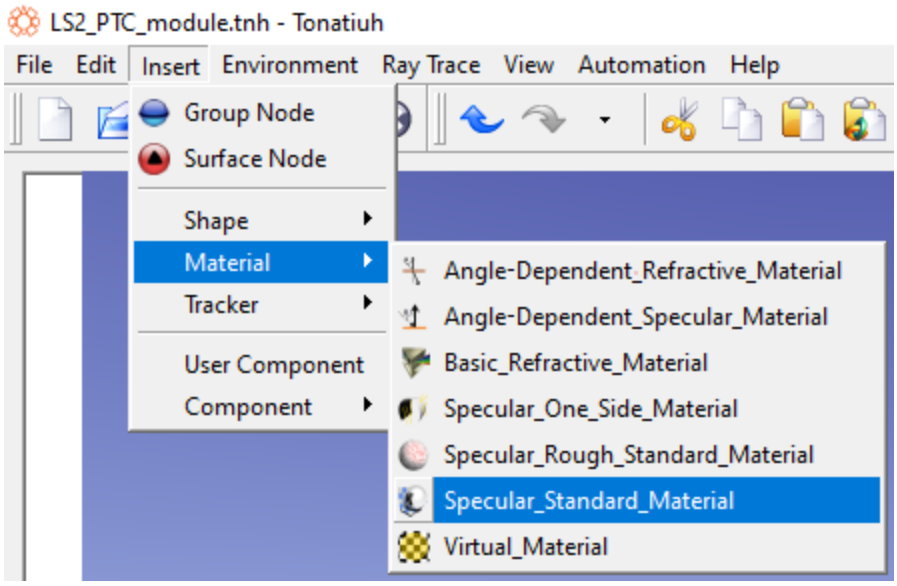

Figure A 4: The parabolic trough material.

For the parabola trough to be completely characterized, information on its optical and geometrical properties is provided. Figures A5, A6, and A7, respectively, show the group node of the reflector, through geometry, and the optical parameter.

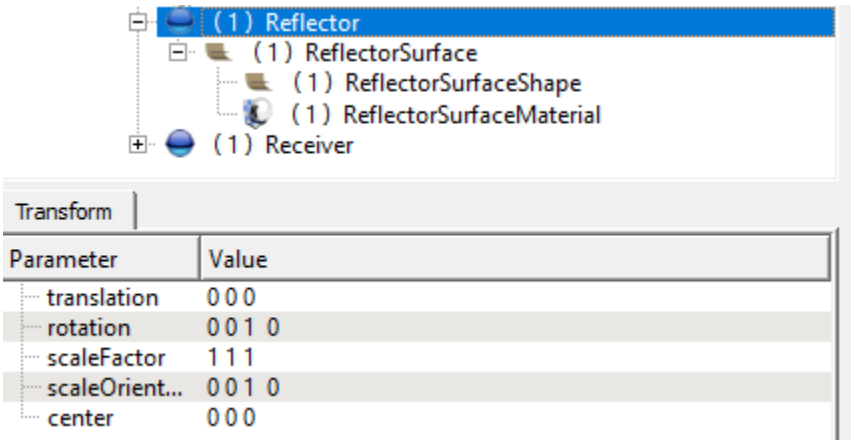

Figure A 5: The group node of the reflector.

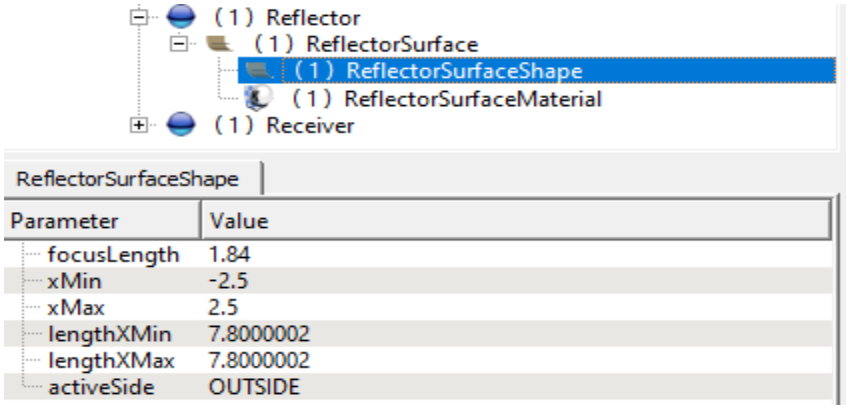

Figure A 6: The parabolic trough geometry.

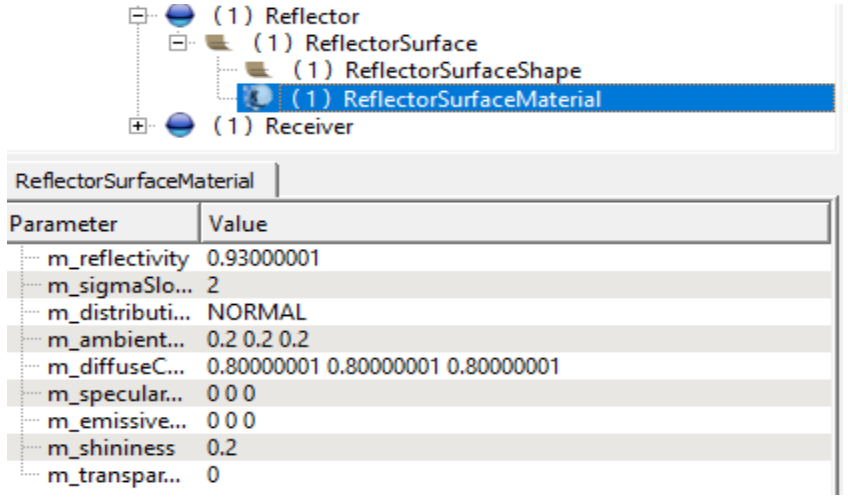

Figure A 7: The reflector surface optical parameter.

B. Develop the receiver tube

It describes how to utilize Tonatiuh to develop the receiver for the PTSC module. Figure B 1's tree representation of the absorber tubes includes the group node and surface node.

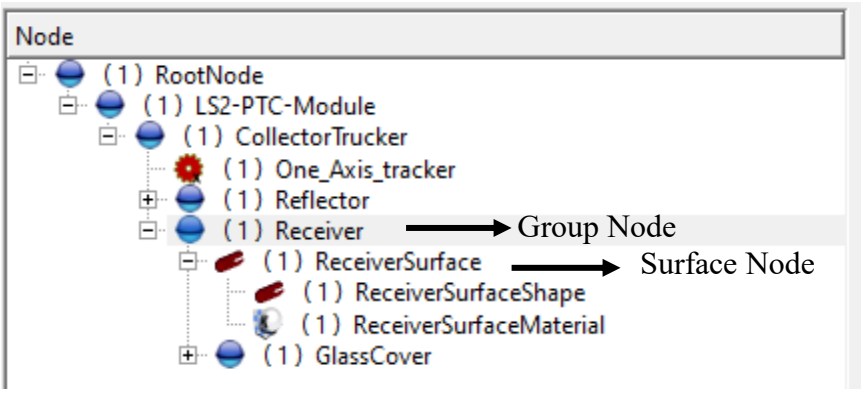

Figure B 1: The receiver tube surface and group node.

For the receiver tube shape “Cylinder” shape is selected and for the material “Standard_ specular Specular_Material” is selected. Figures B 2 and B 3 illustrate how to input the form and the material section in Tonatiuh, respectively.

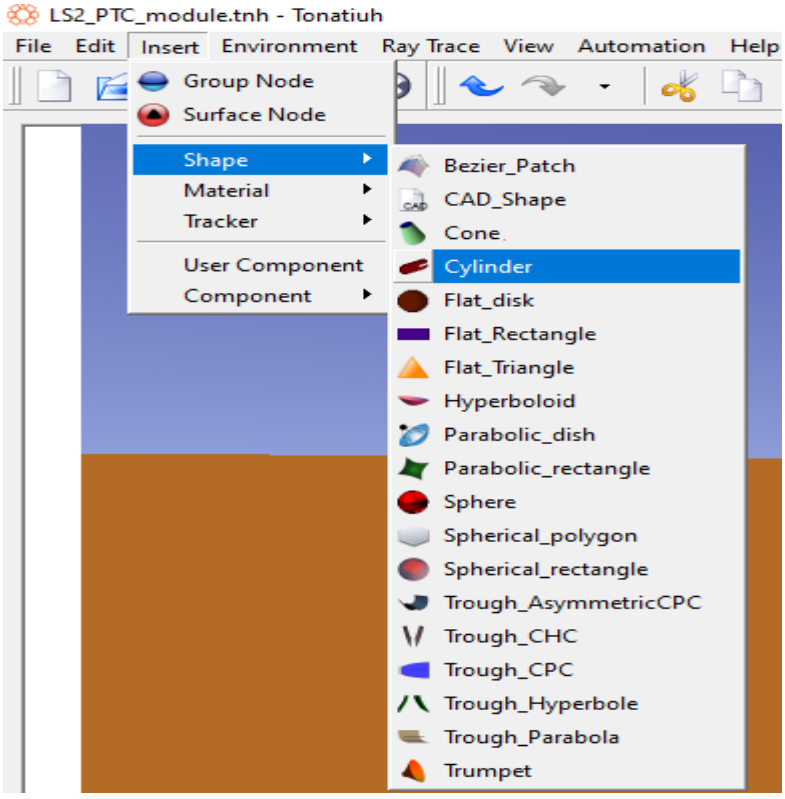

Figure B 2: The receiver tube surface shape.

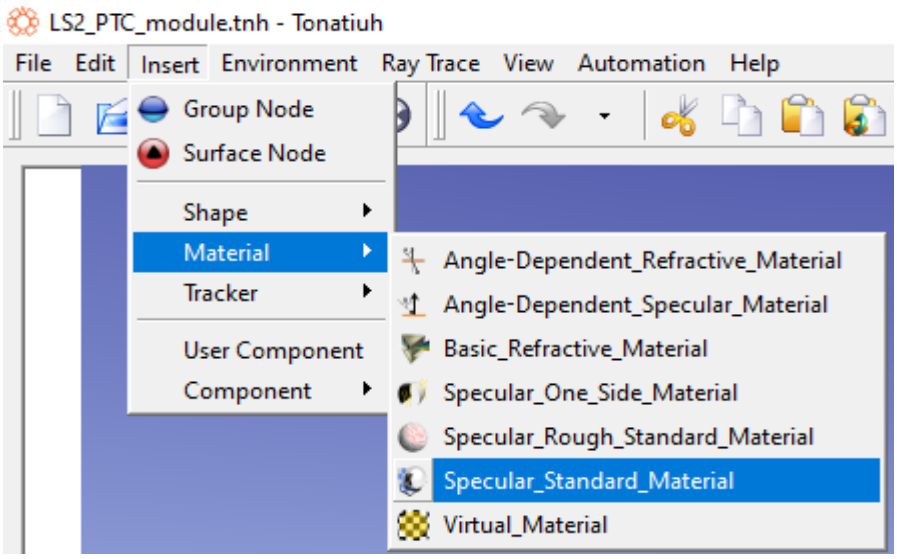

Figure B 3: The receiver tube material surface.

To properly describe the receiver tube, data on optical and geometrical properties are provided. The group node of the receiver, geometric data, and data from the optical are depicted in Figures B 4, B 5, and B 6, respectively.

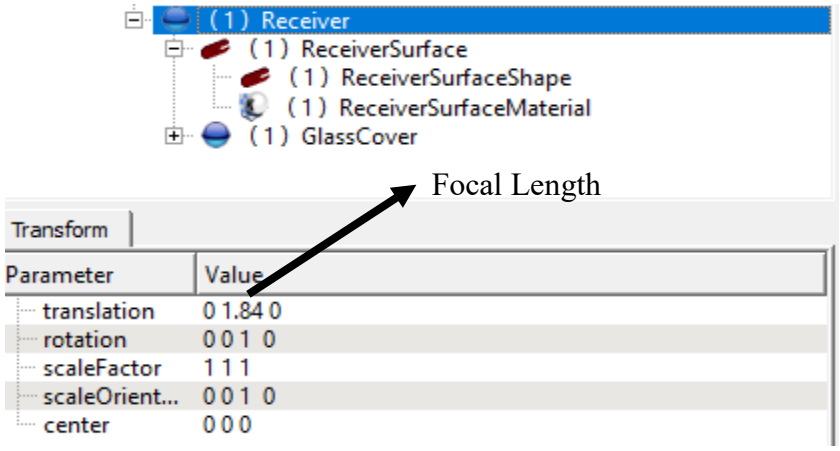

Figure B 4: The group node of the Receiver tube.

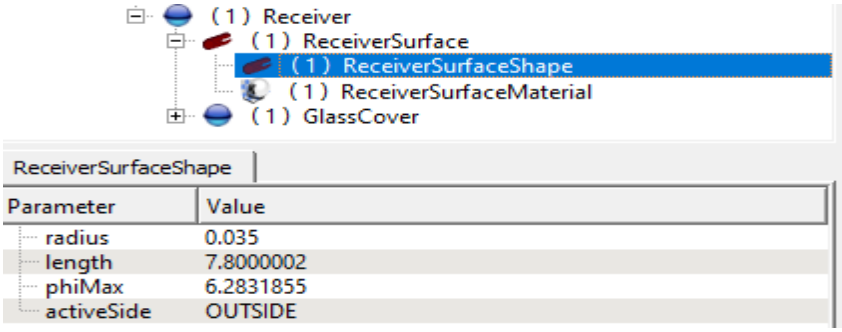

Figure B 5: The receiver tube geometric.

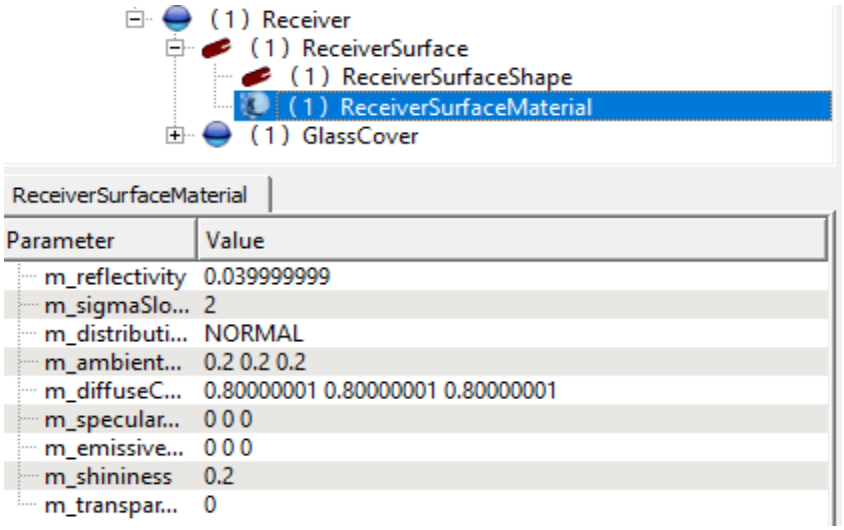

Figure B 6: The receiver tube optical value.

C. Develop the glass cover

It describes how to utilize Tonatiuh to develop the glass cover for the PTSC module. Figure C 1's tree representation of the glass cover includes the surface and group node.

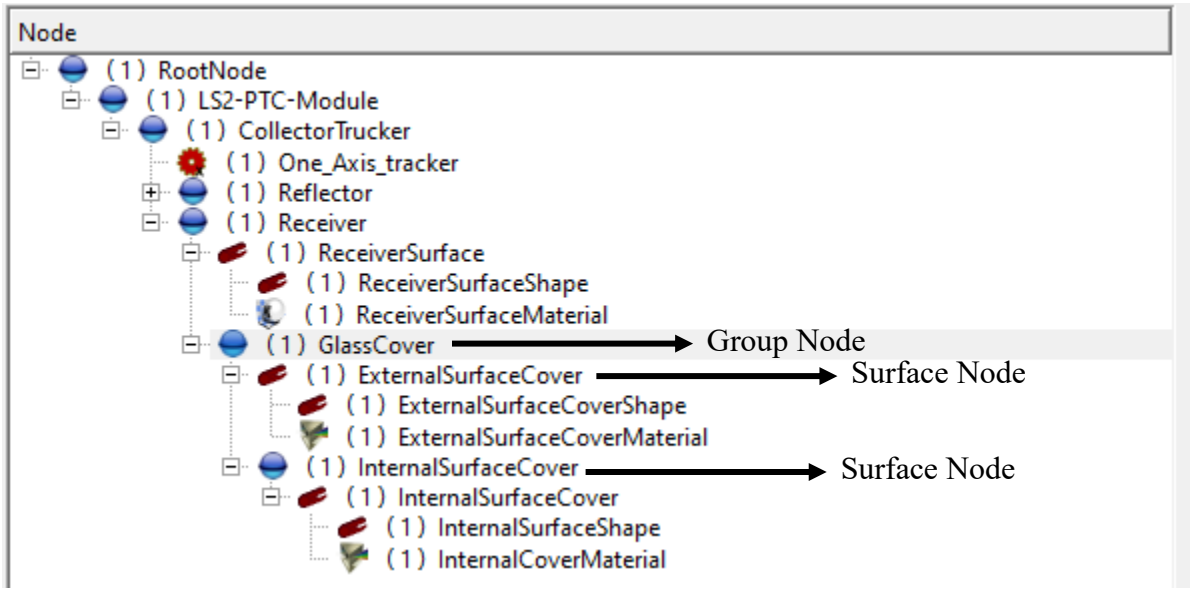

Figure C 1: The glass cover surface and group node.

For the glass cover shape “Cylinder” shape is selected and for the material “Standard_ specular Specular_Material” is selected. Figures C 2 and C 3 illustrate how to input the form and the material section in Tonatiuh, respectively.

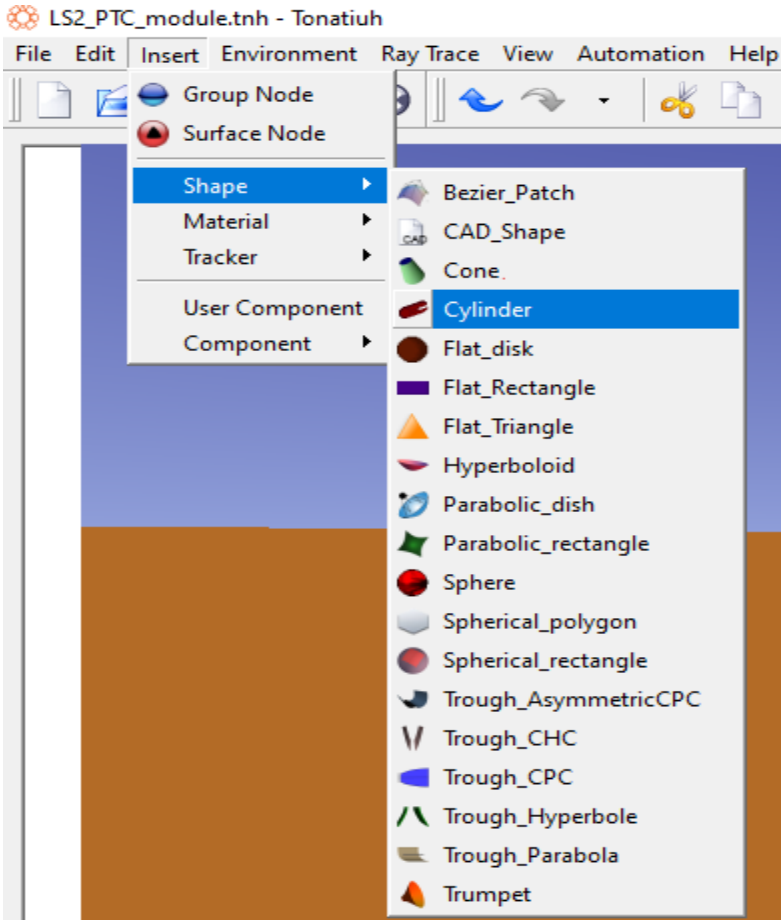

Figure C 2: The glass cover shape surface.

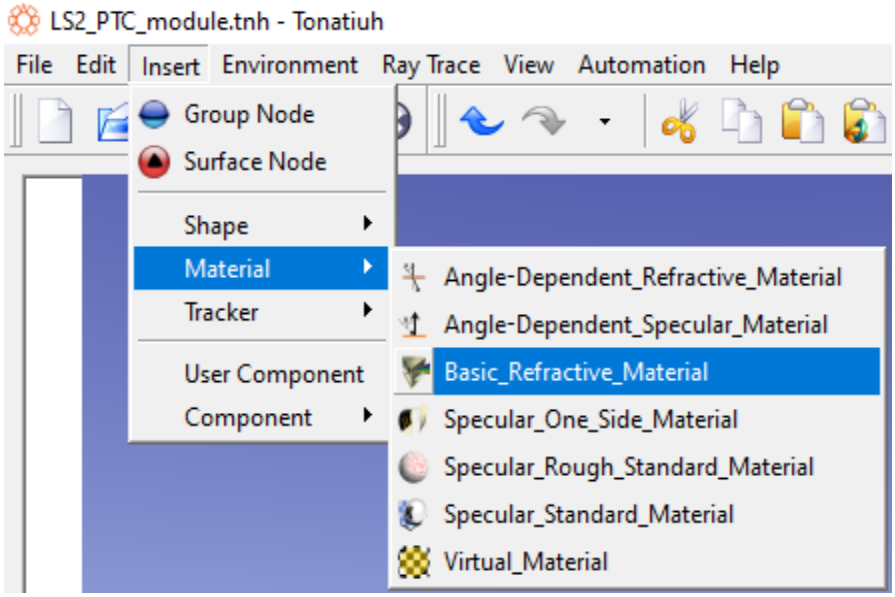

Figure C 3: The glass cover material.

To completely characterize the glass cover, optical and geometrical properties are provided. Figures C4, C5, C6, C7, and C8 show the group node of the glass cover, geometry, and optic value for the outer surface of the glass cover, and also for the internal surface of the glass cover, respectively.

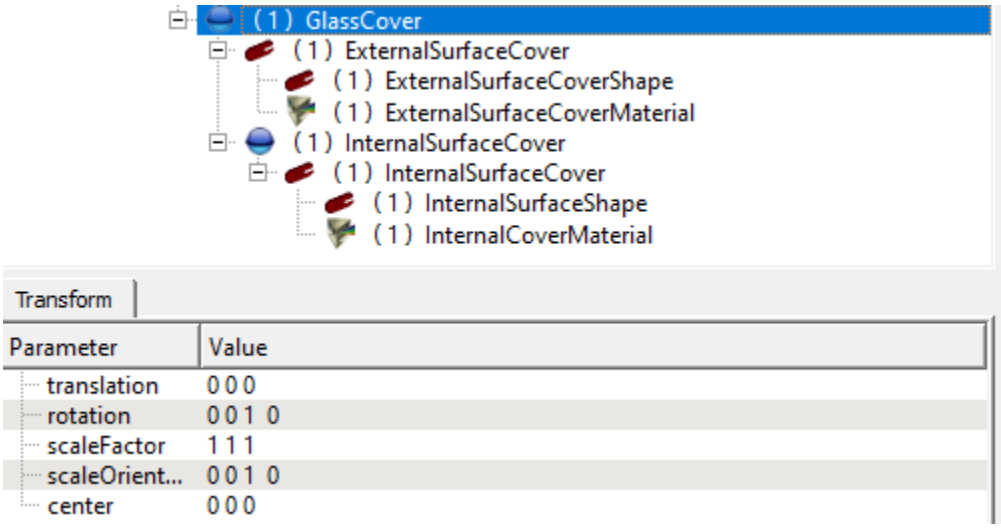

Figure C 4: The group node of the glass cover.

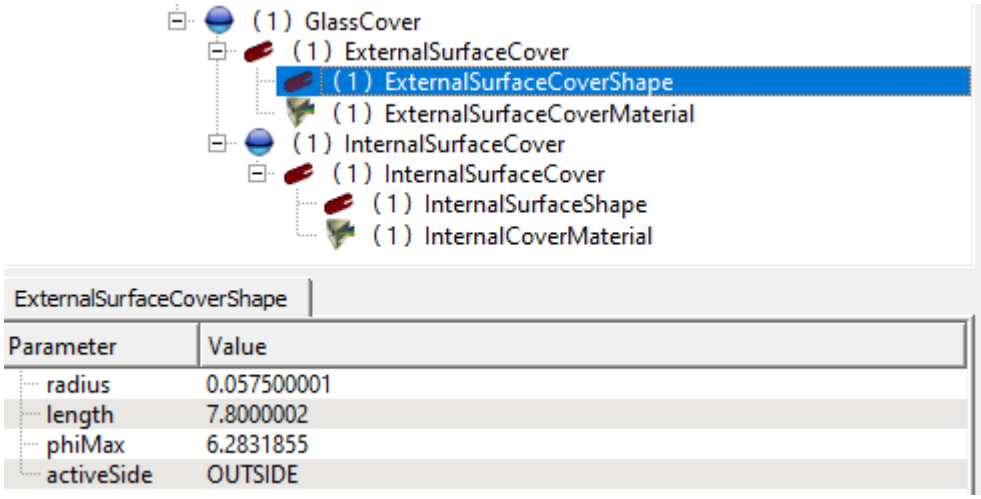

Figure C 5: The outer glass cover parameter.

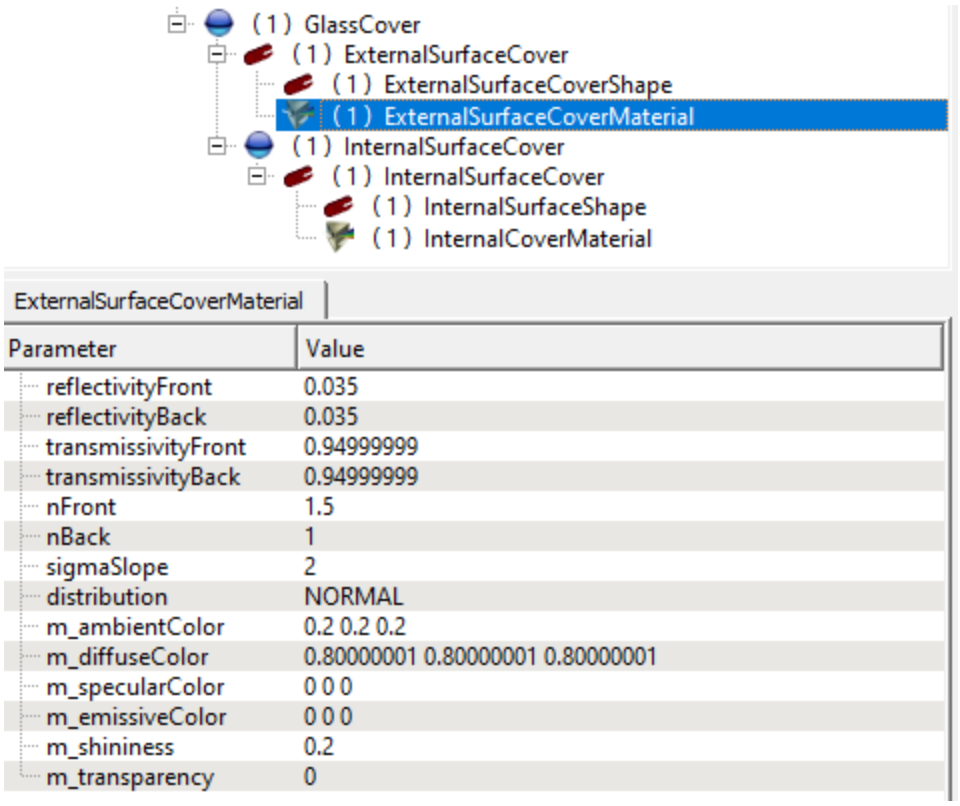

Figure C 6: The outer glass cover optical parameter.

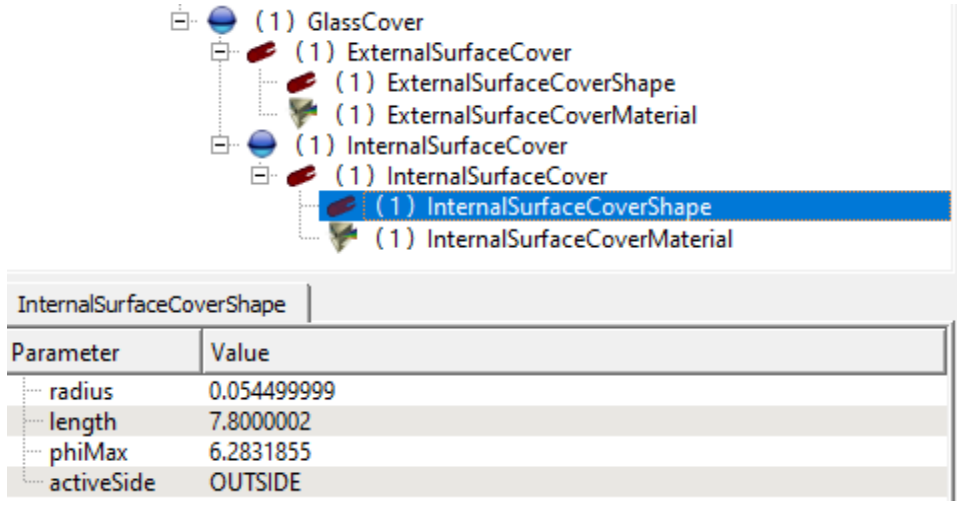

Figure C 7: The inner surface glass cover geometric parameter.

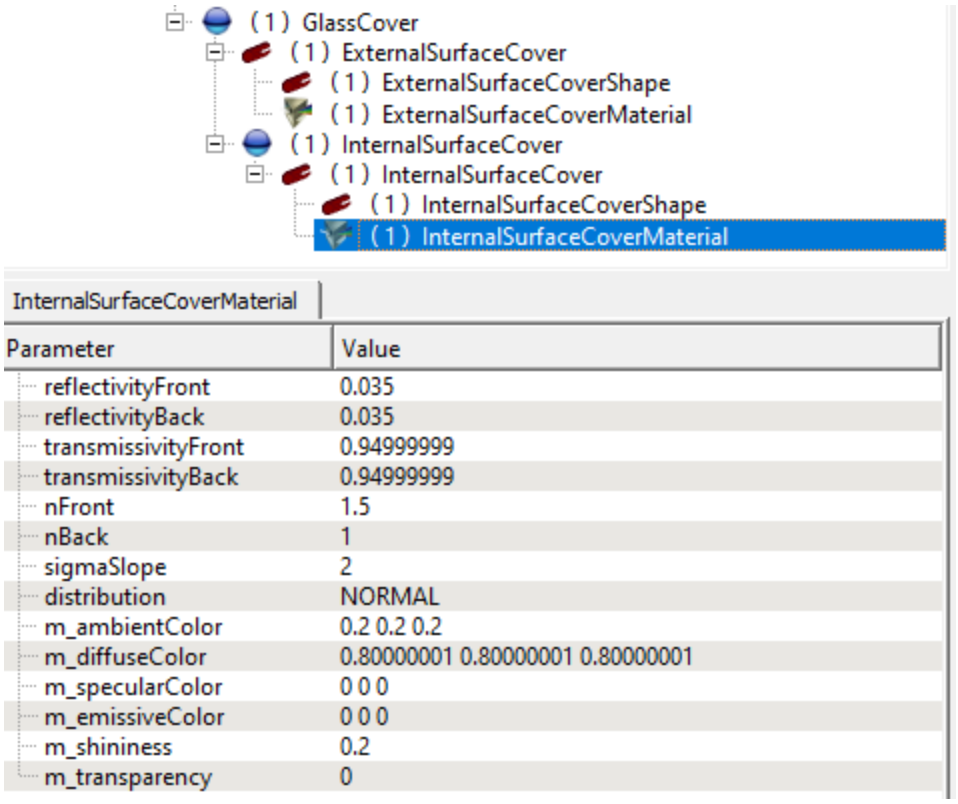

Figure C 8: The inner glass cover optical parameter.

D. Define sunlight

The Sun definition must be inserted after the PTSC geometry has been established. Figure D 1 depicts the Tonatiuh portion where the Sun should be inserted.

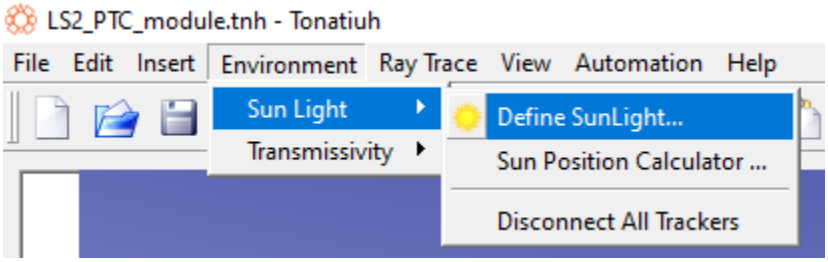

Figure D 1: The portion of Tonatiuh for putting the Sunlight.

Users may enter the variables (DNI, Sun shape, angle of incidence, azimuth angle, etc.) using the "Define Sunlight" option. As a result, it is used for the Sun definition. Given that users can specify the time and place on Earth explicitly the "Sun Position Calculator" in Figure D 1 is also extremely useful. Figure D 2 illustrates the Sun definition.

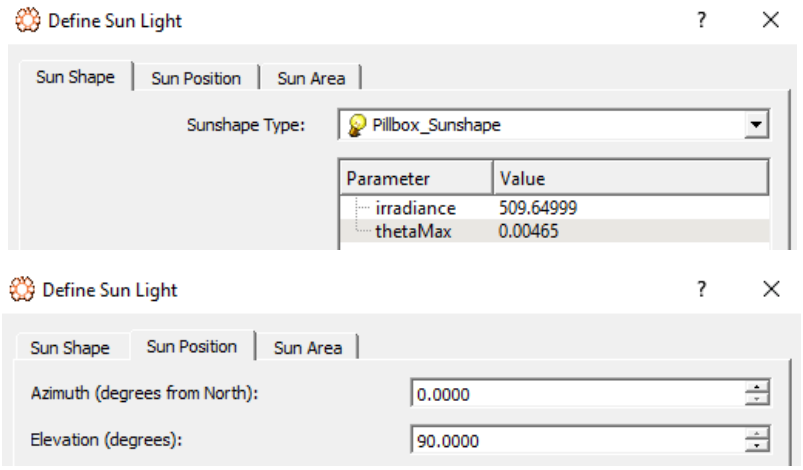

Figure D 2: The Sun description.

Adjust the "Elevation (degrees)" (as defined by the "Sun Positions" tab) to get a variable incidence angle, as shown in Figure D 2.

$$Incidence\ (degrees) = 90 - (degrees) \quad \text{..... (5)}$$

Due to the previously present one-axis tracker, the PTSC component is positioned on the east-west direction path after the position of the sun has been determined. To reposition the PTSC component on the North-South in orientation direction, the system is rotated by $\left(\frac{3\pi}{2}\right)$ radians. Figure D 3 displays the process's specifics.

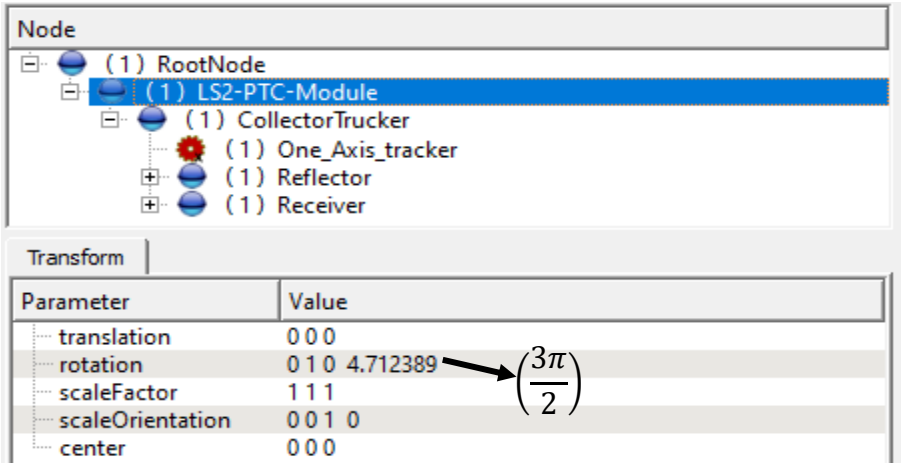

Figure D 3: After describing the Sun, the solar system rotates.

As seen in Figure D 3, the x, y, and z axes are denoted by "0 1 0" for the "rotation" portion, respectively. Since the x- as well as z-axes both have a value of "0," rotation is not done using them. The y-axis is utilized for rotation since it has the value "1". In other words, the y-axis of the PTSC system is rotated by $\frac{3\pi}{2}$ radians.

E. Export the Tonatiuh absorber tube data for post-processing

The model of the PTSC is defined, the definition of the sun is stated, and the total number of rays is established. A ray-tracing simulation could be conducted. First, the method for generating random numbers and the number of rays are specified. The details are displayed in Figures E 1 and E 2.

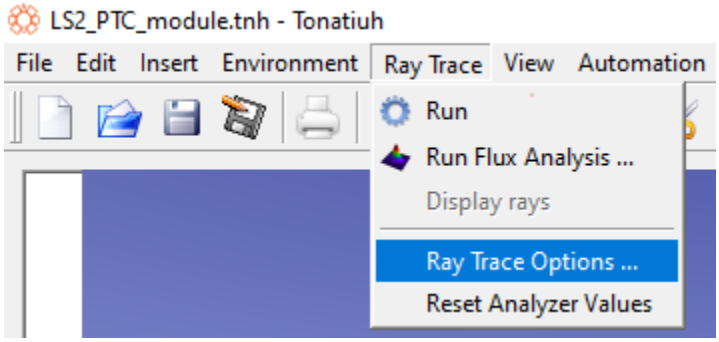

Figure E 1: Tonatiuh's part for configuring ray-trace parameters.

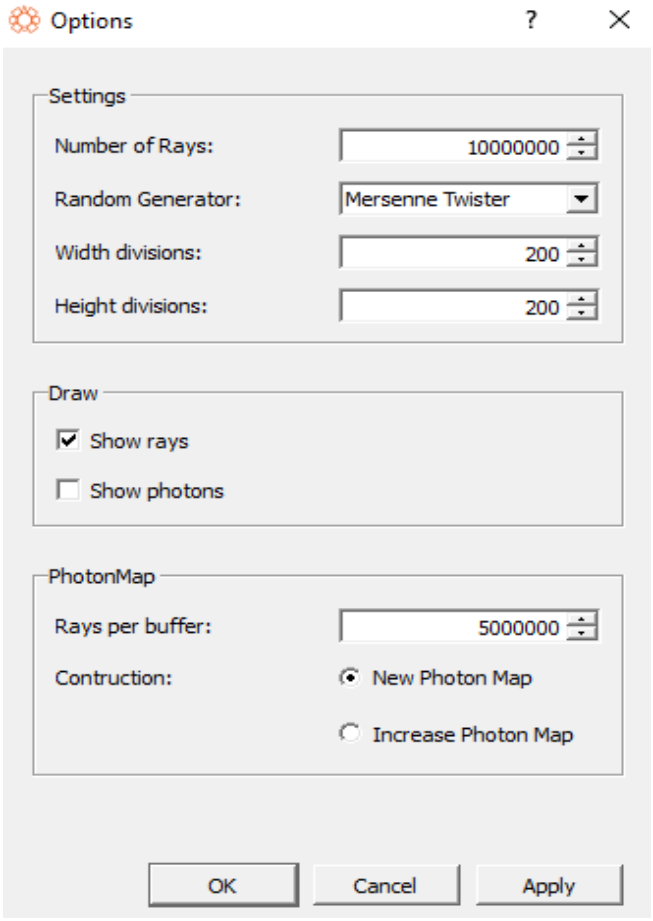

Figure E 2: Overview of ray-tracing parameters

Mersenne Twister is used as a "Random Generator" in Figure E 2. "Number of Rays" is set at 10,000,000, however, the user is free to adjust it. Second, a binary file containing Tonatiuh ray-tracing data is exported. The details are explained in Figures E 3 and E 4.

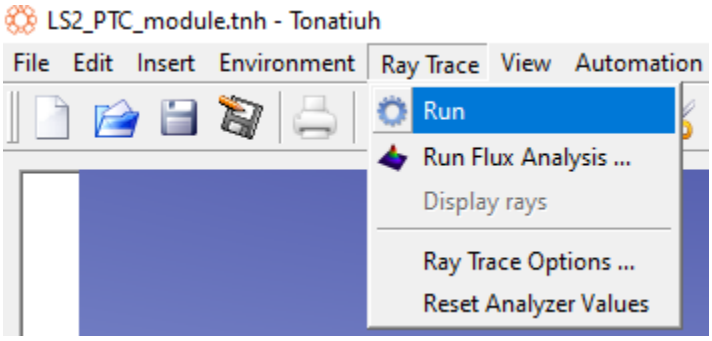

Figure E 3: Exporting the receiver tube's ray trace data.

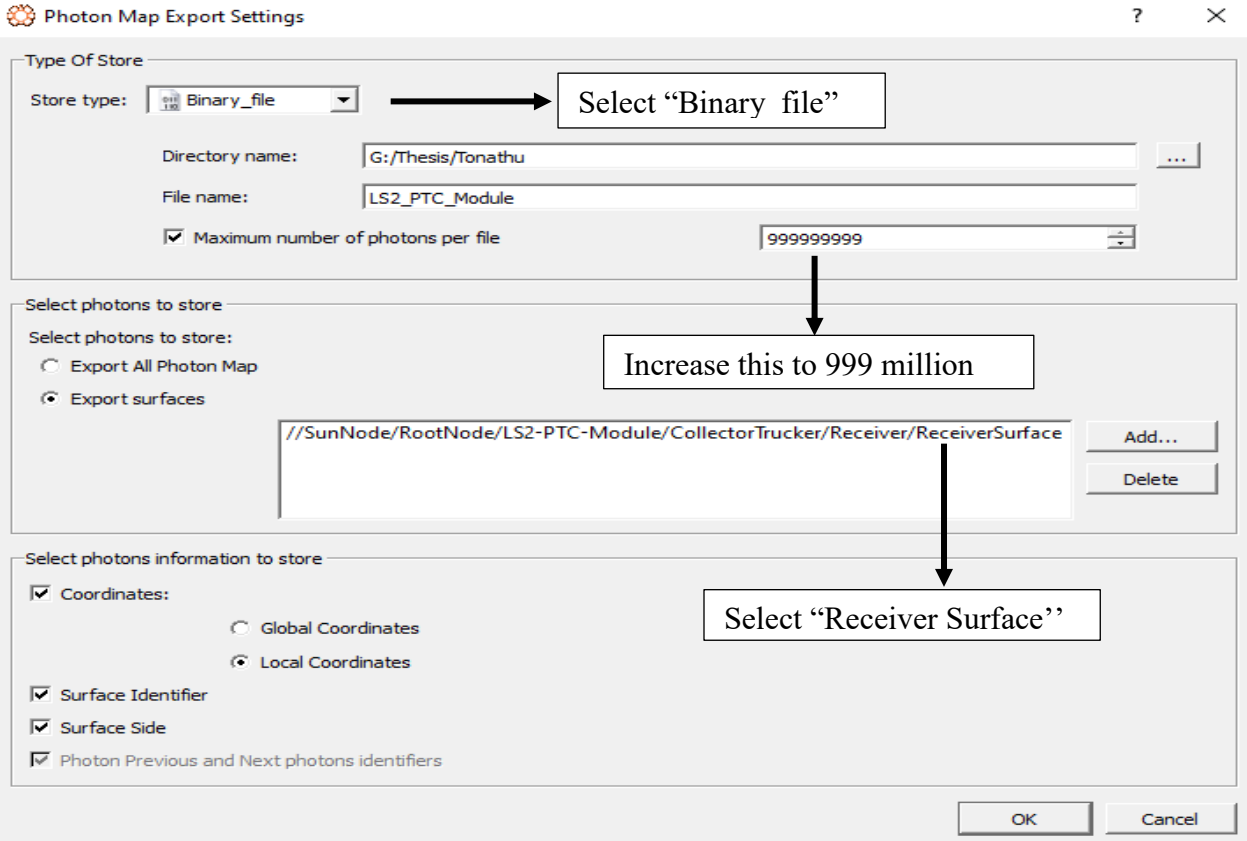

Figure E 4: Description of generating the ray-tracing parameters of the receiver tube.

As opposed to having many binary files, Figure E 4 shows an increase in the number of photons to 999 million (the maximum number of photons per file), writing all of the ray-trace data into a single, easier-to-manage file. The entire simulation's data set does not need to be exported. Only the photon data on the absorber tube's surface is retrieved. Therefore, select "Receivers Surface"

from the directory structure with the "Add..." option. Finally, these outputs are in the form of an a.txt file and a.dat file. MATLAB is used to view the binary file. Figure E 5 depicts the.txt file's overall layout.

```
START PARAMETERS
id
x ⟶ x-coordinates
y ⟶ y-coordinates
z ⟶ z-coordinates
side
surface ID
END PARAMETERS
START SURFACES
1 //SunNode/RootNode/LS2-PTC-Module/CollectorTrucker/Reciver/ReciverSurface
END SURFACES
0.00206044 ⟶ Power of one photon
```

Figure E 5: Overview of.txt parameters.

As shown in the above figure the positions of rays and the power of one photon will be used as the inputs that are needed for the built-in MATLAB program.

F. 2D discretization approach MATLAB code given by Uygur [3]

This section contains the MATLAB code for the 2D discretization. Finite strips are split into the absorber tube's outside surface radially. Figure F 1 shows the finite stripe cylinder surface for the 2D discretization.

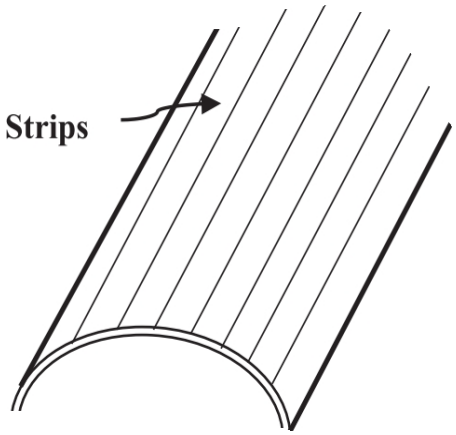

Figure F 1: Finite strips cylinder surface for 2D Discretization [65].

The discretization relies on the axial direction of the sun's rays on the absorber tube face being uniform. As a result, this sort of discretization is appropriate for a 0-degree angle of incident.

The code also includes clarifications.

```
clc
clear all
format long
```

```
%% Generating The Tonatiuh receiver tube data
file_ID=fopen('LS2_PTC_Module_1.dat');
Raw_absorber_tube_data = fread(file_ID,'double','b'); %% b is ordering of
Big-endian
Data_proccessed_for_the_absorber_tube= reshape(Raw_absorber_tube_data, [6,
length(Raw_absorber_tube_data)/6]);
Data_of_the_absorber_tube = Data_proccessed_for_the_absorber_tube';
Data_of_the_absorber_tube_x = Data_of_the_absorber_tube(:,2);
Data_of_the_absorber_tube_y = Data_of_the_absorber_tube(:,3);
Data_of_the_absorber_tube_z = Data_of_the_absorber_tube(:,4);
%% %% The_right_upper_data_part (1/4) of the absorber tube
j = 1;
k = 1; %% %%Samples are employed in the following loops.
for i = 1:1:length(Data_of_the_absorber_tube_x)
     if Data_of_the_absorber_tube_x(i,1) >= 0
            if Data_of_the_absorber_tube_y(i,1) >= 0
                Data_of_the_absorber_tube_Right_Upper_y(j,1) =
Data_of_the_absorber_tube_y(i,1);
                Data_of_the_absorber_tube_Right_Upper_x(k,1) =
Data_of_the_absorber_tube_x(i,1);
                j = j + 1;
                k = k + 1;
            end
     end
end
%% The_right_bottom_data_part (1/4) of the absorber tube
j = 1;
k = 1; %% Samples are employed in the following loops.
for i = 1:1:length(Data_of_the_absorber_tube_x)
    if Data_of_the_absorber_tube_x(i,1) >= 0
        if Data_of_the_absorber_tube_y(i,1) <= 0
            Data_of_the_absorber_tube_Right_Bottom_y(j,1) =
Data_of_the_absorber_tube_y(i,1);
            Data_of_the_absorber_tube_Right_Bottom_x(k,1) =
Data_of_the_absorber_tube_x(i,1);
            j = j + 1;
            k = k + 1;
        end
    end
end
%% The_left_upper_data_part (1/4) of the absorber tube
j = 1;
k = 1; %% %% Samples are employed in the following loops.
for i = 1:1:length(Data_of_the_absorber_tube_x)
 if Data_of_the_absorber_tube_x(i,1) <= 0
   if Data_of_the_absorber_tube_y(i,1) >= 0
    Data_of_the_absorber_tube_Left_Upper_y(j,1) =
Data_of_the_absorber_tube_y(i,1);
    Data_of_the_absorber_tube_Left_Upper_x(k,1) =
Data_of_the_absorber_tube_x(i,1);
    j = j + 1;
    k = k + 1;
   end
 end
end
%% The_left_bottom_data_part (1/4) of the absorber tube
```

```
j = 1;
k = 1; %%  Samples are employed in the following loops.
for i = 1:1:length(Data_of_the_absorber_tube_x)
   if Data_of_the_absorber_tube_x(i,1) <= 0
        if Data_of_the_absorber_tube_y(i,1) <= 0
           Data_of_the_absorber_tube_Left_Bottom_y(j,1) =
Data_of_the_absorber_tube_y(i,1);
           Data_of_the_absorber_tube_Left_Bottom_x(k,1) =
Data_of_the_absorber_tube_x(i,1);
           j = j + 1;
           k = k + 1;
        end
   end
end
%% Finding the Heat Flux profiles at the outer surface of the receiver tube
One_Ray_Power = 0.00206044; %% [W] absorber ray tube data generated from
Tonatiuh
r = 0.035; %% [m] The recevier tube radius
L = 7.8; %% The receiver tube length in the z-direction
theta = 0:1:90; %% Width of the absorber tube & z-direction for the height
division
n = length(theta) - 1; %% strips (cells) number of the absorber tube
Coordinates_of_Right_Upper_Surface= r .* sind(theta); %% arrays keeping track
of strip boundary coordinates
Coordinates_of_Right_Bottom_Surface= r .* sind(theta); %% arrays keeping
track of strip boundary coordinates
Coordinates_of_Left_Upper_Surface= -r .* cosd(theta); %% arrays keeping track
of strip boundary coordinates
Coordinates_of_Left_Bottom_Surface= -r .* cosd(theta); %% arrays keeping
track of strip boundary coordinates
Count_array_strip_Eb_Right_Bottom = zeros(n, 1);
Count_array_strip_Eb_Left_Bottom = zeros(n, 1);
Count_array_strip_Eb_Right_Upper = zeros(n, 1);
Count_array_strip_Eb_Left_Upper = zeros(n, 1);
%% The calculations of energy at the Right_Upper position
for i = 1:1:length(Data_of_the_absorber_tube_Right_Upper_x)
    j = 1;
    if Coordinates_of_Right_Upper_Surface(1,
length(Coordinates_of_Right_Upper_Surface) - 1) <
Data_of_the_absorber_tube_Right_Upper_x(i,1)
        j = n + 1;
        elseif Data_of_the_absorber_tube_Right_Upper_x(i,1) <
Coordinates_of_Right_Upper_Surface(1,2)
            j = 2;
        else
            while Coordinates_of_Right_Upper_Surface(1,j) <
Data_of_the_absorber_tube_Right_Upper_x(i,1)
                j = j + 1;
            end
    end
Count_array_strip_Eb_Right_Upper(j-1,1) = Count_array_strip_Eb_Right_Upper(j-
1,1) + 1;
end
%% Tonatiuh distribution of flux incident  energy of each strip
for i = 1:1:length(Count_array_strip_Eb_Right_Upper)
```

```
    Energy_array_strip_Eb_Right_Upper(i,1) =
(Count_array_strip_Eb_Right_Upper(i,1) *
One_Ray_Power)/(0.5*L*r*pi/(length(Count_array_strip_Eb_Right_Upper)));
end
%% The calculations of energy at the Right_Bottom position
for i = 1:1:length(Data_of_the_absorber_tube_Right_Bottom_x)
    j = 1;
     if Coordinates_of_Right_Bottom_Surface(1,
length(Coordinates_of_Right_Bottom_Surface) - 1) <
Data_of_the_absorber_tube_Right_Bottom_x(i,1)
        j = n + 1;
         elseif Data_of_the_absorber_tube_Right_Bottom_x(i,1) <
Coordinates_of_Right_Bottom_Surface(1,2)
            j = 2;
         else
           while Coordinates_of_Right_Bottom_Surface(1,j) <
Data_of_the_absorber_tube_Right_Bottom_x(i,1)
               j = j + 1;
           end
     end
Count_array_strip_Eb_Right_Bottom(j-1,1) =
Count_array_strip_Eb_Right_Bottom(j-1,1) + 1;
end
%% Tonatiuh distribution of flux incident energy of each strip
for i = 1:1:length(Count_array_strip_Eb_Right_Bottom)
     Energy_array_strip_Eb_Right_Bottom(i,1) =
(Count_array_strip_Eb_Right_Bottom(i,1) *
One_Ray_Power)/(0.5*L*r*pi/(length(Count_array_strip_Eb_Right_Bottom)));
end
%% The calculations of energy at the Left_Upper position
for i = 1:1:length(Data_of_the_absorber_tube_Left_Upper_x)
    j = 1;
    if Coordinates_of_Left_Upper_Surface(1,
length(Coordinates_of_Left_Upper_Surface) - 1) <
Data_of_the_absorber_tube_Left_Upper_x(i,1)
        j = n + 1;
        elseif Data_of_the_absorber_tube_Left_Upper_x(i,1) <
Coordinates_of_Left_Upper_Surface(1,2)
        j = 2;
        else
            while Coordinates_of_Left_Upper_Surface(1,j) <
Data_of_the_absorber_tube_Left_Upper_x(i,1)
                j = j + 1;
            end
    end
   Count_array_strip_Eb_Left_Upper(j-1,1) =
Count_array_strip_Eb_Left_Upper(j-1,1) + 1;
end
%% Tonatiuh distribution of flux incident energy of each strip
for i = 1:1:length(Count_array_strip_Eb_Right_Upper)
    Energy_array_strip_Eb_Left_Upper(i,1) =
(Count_array_strip_Eb_Left_Upper(i,1) *
One_Ray_Power)/(0.5*L*r*pi/(length(Count_array_strip_Eb_Left_Upper)));
end
%% The calculations of energy at the Left_Bottom position
for i = 1:1:length(Data_of_the_absorber_tube_Left_Bottom_x)
```

```
    j = 1;
    if Coordinates_of_Left_Bottom_Surface(1,
length(Coordinates_of_Left_Bottom_Surface) - 1) <
Data_of_the_absorber_tube_Left_Bottom_x(i,1)
       j = n + 1;
         elseif Data_of_the_absorber_tube_Left_Bottom_x(i,1) <
Coordinates_of_Left_Bottom_Surface(1,2)
              j = 2;
        else
             while Coordinates_of_Left_Bottom_Surface(1,j) <
Data_of_the_absorber_tube_Left_Bottom_x(i,1)
                 j = j + 1;
             end
    end
     Count_array_strip_Eb_Left_Bottom(j-1,1) =
Count_array_strip_Eb_Left_Bottom(j-1,1) + 1;
end
%% Tonatiuh distribution of flux incident energy of each strip
for i = 1:1:length(Count_array_strip_Eb_Left_Bottom)
    Energy_array_strip_Eb_Left_Bottom(i,1) =
(Count_array_strip_Eb_Left_Bottom(i,1) *
One_Ray_Power)/(0.5*L*r*pi/(length(Count_array_strip_Eb_Left_Bottom)));
end
%% Plot_x = linspace(Coordinates_of_Surface_1(1,1),
Coordinates_of_Surface_1(1,end), length(Count_array_strip_Eb_1));
for i = 1:1:length(Coordinates_of_Right_Upper_Surface) - 1
    Right_Upper_x(i,1) = (Coordinates_of_Right_Upper_Surface(1,i) +
Coordinates_of_Right_Upper_Surface(1,i+1)) / 2;
end
for i = 1:1:length(Coordinates_of_Right_Bottom_Surface) - 1
    Right_Bottom_x(i,1) = (Coordinates_of_Right_Bottom_Surface(1,i) +
Coordinates_of_Right_Bottom_Surface(1,i+1)) / 2;
end
for i = 1:1:length(Coordinates_of_Left_Upper_Surface) - 1
    Left_Upper_x(i,1) = (Coordinates_of_Left_Upper_Surface(1,i) +
Coordinates_of_Left_Upper_Surface(1,i+1)) / 2;
end
for i = 1:1:length(Coordinates_of_Left_Bottom_Surface) - 1
    Left_Bottom_x(i,1) = (Coordinates_of_Left_Bottom_Surface(1,i) +
Coordinates_of_Left_Bottom_Surface(1,i+1)) / 2;
end
%% Boundary condition of Right Upper surface Piecewise function
j = 1;
k = 1;
m = 1;
for i =  1:1:length(Right_Upper_x)
    if Right_Upper_x(i,1) <= 0.02813
        Right_Upper_x_up_to_28_mm(j,1) = Right_Upper_x(i,1);
        Energy_array_strip_Eb_Right_Upper_up_to_28_mm(j,1) =
Energy_array_strip_Eb_Right_Upper(i,1);
        j = j + 1;
        elseif (0.02813 < Right_Upper_x(i,1)) && (Right_Upper_x(i,1) <=
0.03373)
                Right_Upper_x_28_to_33_mm(k,1) = Right_Upper_x(i,1);
                Energy_array_strip_Eb_Right_Upper_28_to_33_mm(k,1) =
Energy_array_strip_Eb_Right_Upper(i,1);
```

```
                k = k + 1;
        else
            Right_Upper_x_after_33_mm(m,1) = Right_Upper_x(i,1);
            Energy_array_strip_Eb_Right_Upper_after_33_mm(m,1) =
Energy_array_strip_Eb_Right_Upper(i,1);
            m = m + 1;
    end
end
%% Boundary condition of Right Bottom surface Piecewise function
j = 1;
k = 1;
m = 1;
for i = 1:1:length(Right_Bottom_x)
    if Right_Bottom_x(i,1) <= 0.005
       Right_Bottom_x_up_to_5_mm(j,1) = Right_Bottom_x(i,1);
       Energy_array_strip_Eb_Right_Bottom_up_to_5_mm(j,1) =
Energy_array_strip_Eb_Right_Bottom(i,1);
        j = j + 1;
          elseif (0.005 < Right_Bottom_x(i,1)) && (Right_Bottom_x(i,1) <=
0.02)
            Right_Bottom_x_5_to_20_mm(k,1) = Right_Bottom_x(i,1);
            Energy_array_strip_Eb_Right_Bottom_5_to_20_mm(k,1) =
Energy_array_strip_Eb_Right_Bottom(i,1);
            k = k + 1;
         else
            Right_Bottom_x_after_20_mm(m,1) = Right_Bottom_x(i,1);
            Energy_array_strip_Eb_Right_Bottom_after_20_mm(m,1) =
Energy_array_strip_Eb_Right_Bottom(i,1);
            m = m + 1;
   end
end
%% Boundary condition of Left Upper surface Piecewise function
j = 1;
k = 1;
m = 1;
for i = 1:1:length(Left_Upper_x)
    if Left_Upper_x(i,1) >= -0.02849
        Left_Upper_x_up_to_28_mm(j,1) = Left_Upper_x(i,1);
        Energy_array_strip_Eb_Left_Upper_up_to_28_mm(j,1) =
Energy_array_strip_Eb_Left_Upper(i,1);
        j = j + 1;
        elseif (-0.02849 > Left_Upper_x(i,1)) && (Left_Upper_x(i,1) >= -
0.03373)
                Left_Upper_x_28_to_33_mm(k,1) = Left_Upper_x(i,1);
                Energy_array_strip_Eb_Left_Upper_28_to_33_mm(k,1) =
Energy_array_strip_Eb_Left_Upper(i,1);
                k = k + 1;
        else
            Left_Upper_x_after_33_mm(m,1) = Left_Upper_x(i,1);
            Energy_array_strip_Eb_Left_Upper_after_33_mm(m,1) =
Energy_array_strip_Eb_Left_Upper(i,1);
            m = m + 1;
    end
end
%% Boundary condition of Left Bottom surface Piecewise function
j = 1;
```

```
k = 1;
m = 1;
for i = 1:1:length(Left_Bottom_x)
    if Left_Bottom_x(i,1) >= -0.005
        Left_Bottom_x_up_to_5_mm(j,1) = Left_Bottom_x(i,1);
        Energy_array_strip_Eb_Left_Bottom_up_to_5_mm(j,1) =
Energy_array_strip_Eb_Left_Bottom(i,1);
        j = j + 1;
     elseif (-0.005 > Left_Bottom_x(i,1)) && (Left_Bottom_x(i,1) >= - 0.02)
            Left_Bottom_x_5_to_20_mm(k,1) = Left_Bottom_x(i,1);
            Energy_array_strip_Eb_Left_Bottom_5_to_20_mm(k,1) =
Energy_array_strip_Eb_Left_Bottom(i,1);
            k = k + 1;
        else
            Left_Bottom_x_after_20_mm(m,1) = Left_Bottom_x(i,1);
            Energy_array_strip_Eb_Left_Bottom_after_20_mm(m,1) =
Energy_array_strip_Eb_Left_Bottom(i,1);
            m = m + 1;
    end
end
%% Plot Right Upper surface rays distribution
figure(1)
plot(Right_Upper_x,Energy_array_strip_Eb_Right_Upper)
set(gca, 'FontSize', 16)
xlabel('x-coordinate', 'FontSize', 16)
ylabel('The distribution of flux incident','FontSize',16)
%%ylabel('Incident Flux Distribution', 'FontSize', 20)
title('(Right Upper part)absorber tube on the x-z cross-section non-uniform
rays distribution', 'FontSize', 16)
%% Plot Right Bottom surface rays distribution
figure(2)
plot(Right_Bottom_x,Energy_array_strip_Eb_Right_Bottom)
set(gca, 'FontSize', 16)
xlabel('x-coordinate', 'FontSize', 16)
ylabel('The distribution of flux incident', 'FontSize', 16)
title('(Right_Upper_part)_absorber tube on the x-z cross-section non-uniform
rays distribution', 'FontSize', 16)
%% Plot Left Upper surface rays distribution
figure(3)
plot(Left_Upper_x,Energy_array_strip_Eb_Left_Upper)
set(gca, 'FontSize', 16)
xlabel('x-coordinate', 'FontSize', 16)
ylabel('The distribution of flux incident', 'FontSize', 16)
title('(Left_Upper_part)_absorber tube on the x-z cross-section non-uniform
rays distribution', 'FontSize', 16)
%% Plot Left Bottom surface rays distribution
figure(4)
plot(Left_Bottom_x,Energy_array_strip_Eb_Left_Bottom)
set(gca, 'FontSize', 16)
xlabel('x-coordinate', 'FontSize', 16)
ylabel('The distribution of flux incident', 'FontSize', 16)
title('(Left_Bottom_part)_absorber tube on the x-z cross-section non-uniform
rays distribution', 'FontSize', 16)
%% Tonatiuh result Verification
The_Total_Power = length(Data_of_the_absorber_tube_x)*One_Ray_Power;
The_average_heat_flux = The_Total_Power / (2*L*r*pi)
```

```
if max(Count_array_strip_Eb_Right_Bottom) >=
max(Count_array_strip_Eb_Left_Bottom)
   Count_array_strip_Eb_max = Count_array_strip_Eb_Right_Bottom;
    else
      Count_array_strip_Eb_max = Count_array_strip_Eb_Left_Bottom;
end
Maximum_Heat_Flux = (max(Count_array_strip_Eb_max)*
One_Ray_Power)/(0.5*L*r*pi/(length(Count_array_strip_Eb_max)))
```

G. Zero-degree angle of incidence piecewise "Right-Upper" curve-fitting

The piecewise "Right-Upper" surface is described in detail in this APPENDIX for curve-fitting. Primarily, the highest-order polynomial is fitted to the distribution of heat flux on the "Right-Upper" surface. In this instance, the polynomial curve's greatest order is 4. Figure G 1 shows the fitted 4th-order polynomial for the whole "Right-Upper" surface.

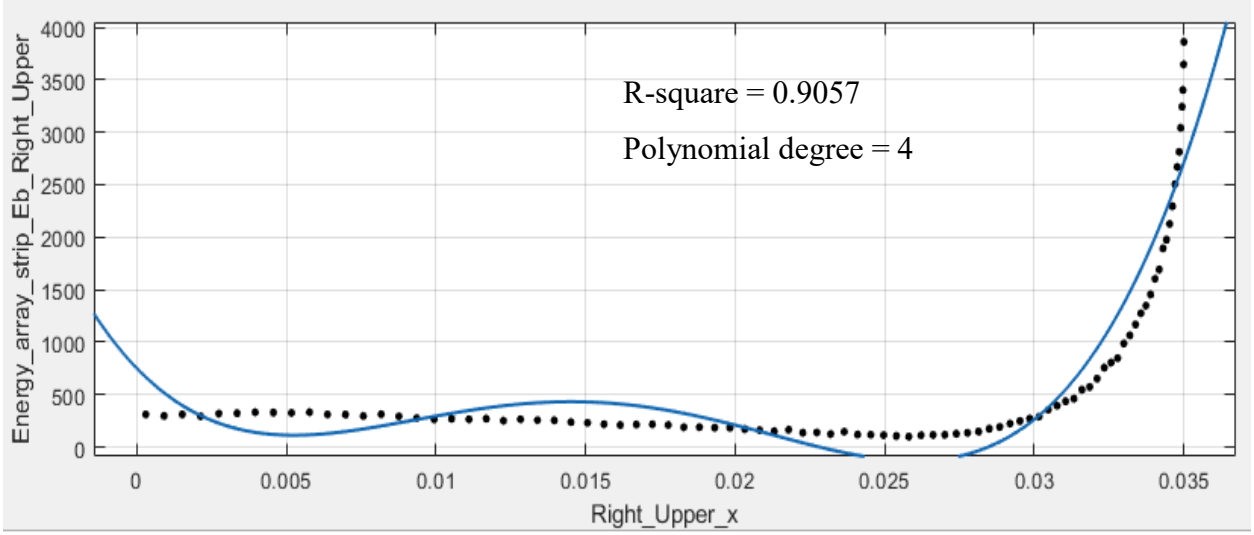

Figure G 1: "Right_Upper" surface 4th order polynomial fitted line.

Keep in mind that MATLAB displays the message "Equation is badly conditioned" if the polynomial order is higher than 4. Eliminate redundant data points or attempt scaling and centring, if possible. The 35 mm distance in the x-direction is split into three sub-intervals as follows after examining Figure G 1:

The highest-order polynomial curve is then fitted to each of these sub-intervals. In Figure G 2, a curve fit for $x \leq 0.02849$ m is shown.

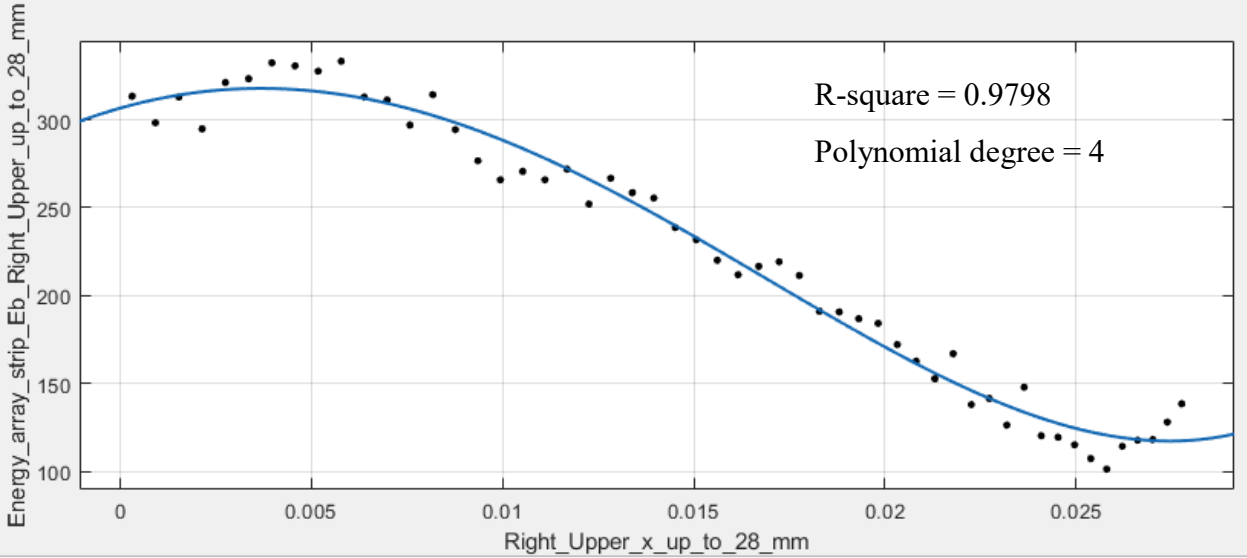

Figure G 2: $x \leq 0.02849$ m of picewise fitting curve.

Figure G 3 shows the curve fitting of $0.02849 < x \leq 0.03373\ m$.

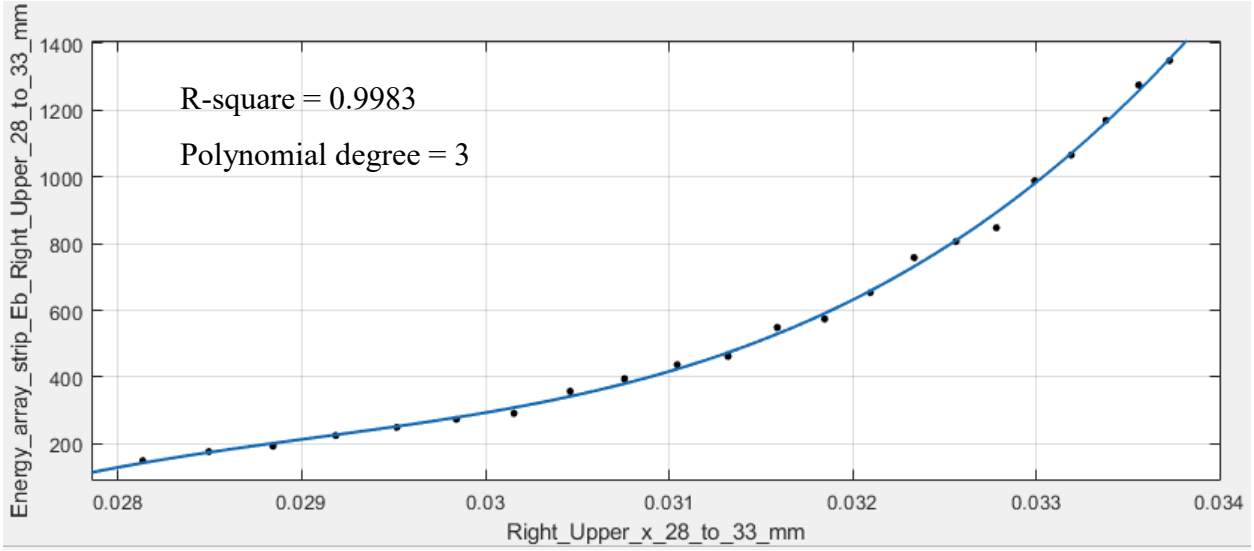

Figure G 3: $0.02849\ m \leq 0.03373\ m$ of piecewise fitting curve.

Figure G 4. Shows for $x > 0.03373\ m$ the curve fitting.

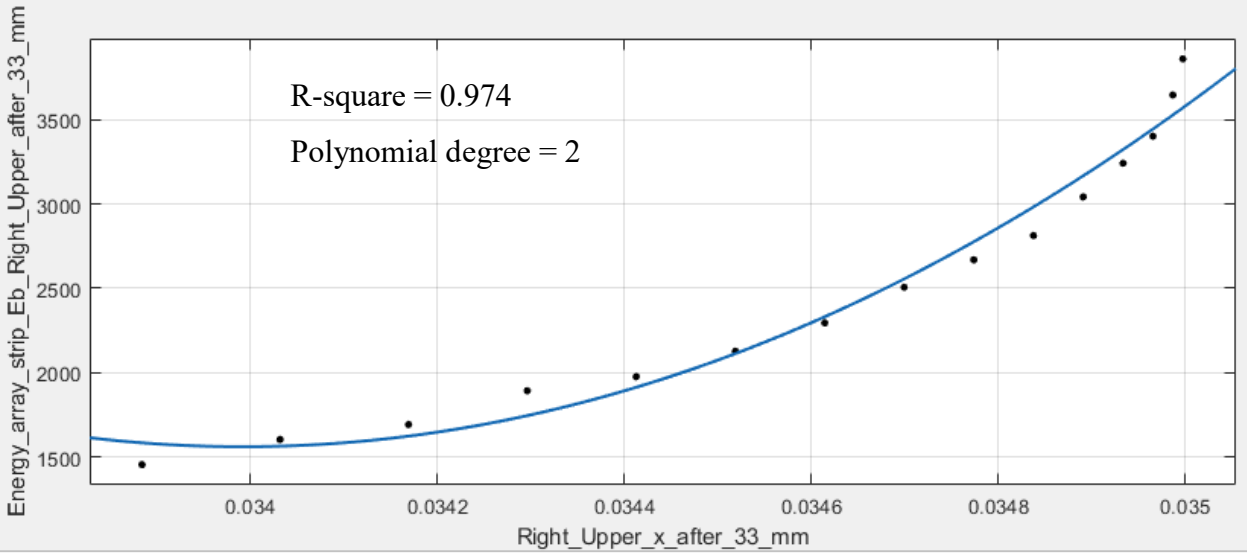

Figure G 4: $x > 0.03373\ m$ picewise fitting curve.

To resolve the distribution of the heat flux across the receiver tube as precisely as feasible, piecewise curve-fitting is used. In conclusion, rather than fitting the curve with a single polynomial equation for the boundary condition, the x-direction of the outer surface of the receiver tube is split into 3 sections. Each of these sub-intervals is fitted with the highest-order polynomial curve.

H. UDFs 2D discretization approach for PTSC and nanofluid

```
#include "udf.h"
#define phi 0.2
DEFINE_PROPERTY (viscosity_nf,c,t)
{
        real  munf;
        real temp = C_T(c,t);
        munf = 0.006147424 - 0.00001803 * temp + 0.000199429 * phi;
        return munf;
}
DEFINE_PROPERTY (thermal_nf,c,t)
{
        real knf;
        real temp = C_T(c,t);
        knf  = -0.19024 + 0.002655 * temp + 0.104057 * phi;
```

```
        return knf;
}
DEFINE_PROPERTY (density_nf,c,t)
{
        real dnf;
        real temp = C_T(c,t);
        dnf = 1091.057 - 0.31345 * temp + 46.871 * phi;
        return dnf;
}
DEFINE_PROPERTY (Specificheat_nf,c,t)
{
        real snf;
        real temp = C_T(c,t);
        snf = 4140.743 + 0.1244 * temp - 37.5937 * phi;
        return snf;
}
/ *  "Right_Upper" UDF Function *  /
DEFINE_PROFILE (Right_Upper_profile, t, i)
{
real x [ND_ND]; / *  this will hold the position vector  * /
real y;
face_t f;
begin_f_loop (f, t)
{
            F_CENTROID (x, f, t);
            y = x [0];
if (y <= 0.02813)
F_PROFILE (f, t, i) = 4.595e8 * y * y * y * y + 1.274e6 * y * y * y - 8.57e5 * y * y + 6153 * y +
306.8;
else if (y >  0.02813 && y <= 0.03373)
F_PROFILE (f, t, i) = 7.888e9 * y * y * y - 6.881e8 * y * y + 2.009e7 * y - 1.959e5;
```

```
else
F_PROFILE (f, t, i) = 1.986e9 * y * y - 1.35e8 * y + 2.296e6;
}
end_f_loop (f, t)
}
/ *  "Right_Bottom" UDF Function  * /
DEFINE_PROFILE (Right_Bottom_profile, t, i)
{
real x [ND_ND];
real y;
face_t f;
begin_f_loop (f, t)
{
            F_CENTROID (x, f, t);
         y = x [0];
        if (y <= 0.005)
F_PROFILE (f, t, i) = - 1.334e9 * y * y * y + 1.136e7 * y * y - 3144 * y + 2.076e4;
else if (y >  0.005 && y <= 0.02)
F_PROFILE (f, t, i) = 6.431e10 * y * y * y * y - 4.123e9 * y * y * y + 8.169e7 * y * y - 5.703e5 *
y + 2.226e4;
else
F_PROFILE (f, t, i) = -7.122e11 * y * y * y * y + 7.282e10 * y * y * y - 2.817e9 * y * y + 4.82e7
* y - 2.853e5;
}
end_f_loop (f, t)
}
/ *  "Left_Upper" UDF Function  * /
DEFINE_PROFILE (Left_Upper_profile, t, i)
{
real x [ND_ND];
real y;
```

```
face_t f;
 begin_f_loop (f, t)
{
            F_CENTROID (x, f, t);
            y = x [0];
if (y > = -0.02849
F_PROFILE (f, t, i) = 2.566e9 * y * y * y * y + 1.211e8 * y * y * y + 1.457e6 * y * y + 9265 * y
+ 328.7;
else if (y < -0.02849 && y > = -0.03373)
F_PROFILE (f, t, i) = -8.464e9 * y * y * y - 7.446e8 * y * y - 2.192e7 * y - 2.158e5;
else
F_PROFILE (f, t, i) = 2.072e9 * y * y + 1.409e8 * y + 2.397e6;
}
end_f_loop (f, t)
}
/ *  "Left_bottom" UDF Function  * /
DEFINE_PROFILE (Left_Bottom_profile, t, i)
{
real x [ND_ND];
real y;
face_t f;
 begin_f_loop (f, t)
{
            F_CENTROID (x, f, t);
             y = x [0];
if (y > = -0.005)
F_PROFILE (f, t, i) = 1.486e10 * y * y * y + 1.185e8 * y * y + 1.858e5 * y + 2.073e4;
else if (y < -0.005 && y > = -0.02)
F_PROFILE (f, t, i) = -9.135e10 * y * y * y * y - 4.194e9 * y * y * y - 7.489e7 * y * y - 6.406e5
* y + 1.909e4;
else
```

F_PROFILE (f, t, i) = -8.321e11 * y * y * y * y - 8.636e10 * y * y * y - 3.385e9 * y * y - 5.871e7 * y - 3.575e5;

}

end_f_loop (f, t)

}

I. Generate Tonatiuh curve of IAM

This section explains how to use Tonatiuh to obtain the IAM curve. Figure I 1 provides the analysis of the curve of IAM from the sunlight definition.

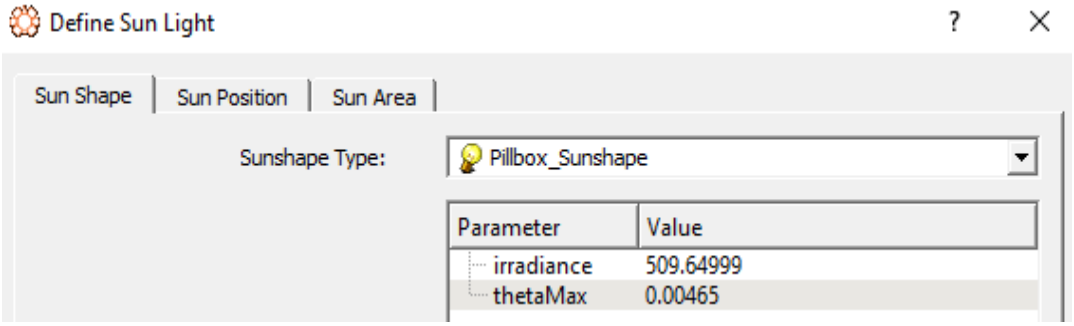

Figure I 1: Analysis of the curve of IAM from sun definition.

The IAM curve for the PTSC module is created using "Run Flux Analysis" Tonatiuh's program, see Figure I 2.

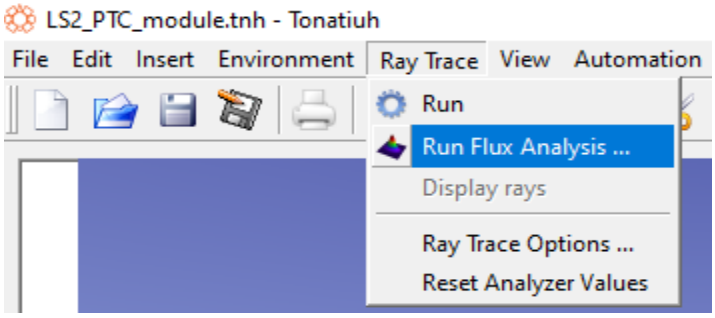

Figure I 2: Tonatiuh ray-trace function of “Run Flux Analysis”.

Function "Run Flux Analysis" for 0° angle of incidence, the process is described and illustrated below for a 0-degree incidence angle.

The "Surface URL" is chosen from the tree structure and is "ReceiverSurface". The word "OUTSIDE" is selected as the "Active side." "Width" denotes division in the radial direction (x-direction) in the "Grid divisions" section, while "Height" denotes division in the axial direction (z-direction). The initial step in flux analysis is to use $5x10^5$ rays. Once the "Horizontal Sector" and

"Vertical Sector" plots are smooth, that is, the graph's oscillations vanish, the "Append to previous simulation" option is selected and the number of rays is gradually raised. Figure I 3 explains this process for 10^6 rays.

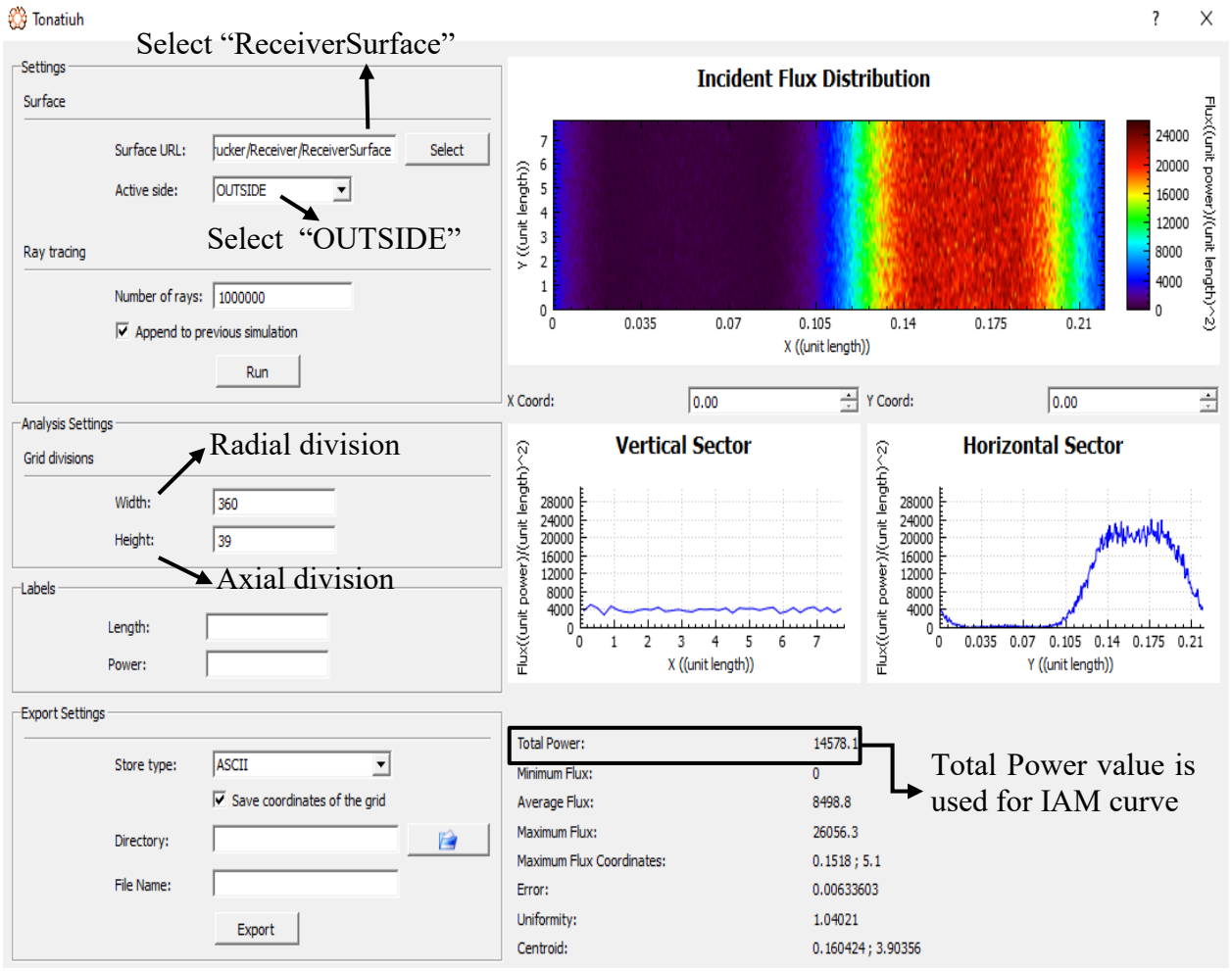

Figure I 3: PTSC module 10^6 rays for "Run Flux Analysis".

The "Horizontal Sector" plot's "Y Coord" value may be used to see the distribution heat flux in the radial direction, while the "Vertical Sector" plot's "X Coord" value can be used to visualize the distribution heat flux along the axial direction. Figure I 4 depicts a comprehensive view of the plots 10^6 rays and heat flux.

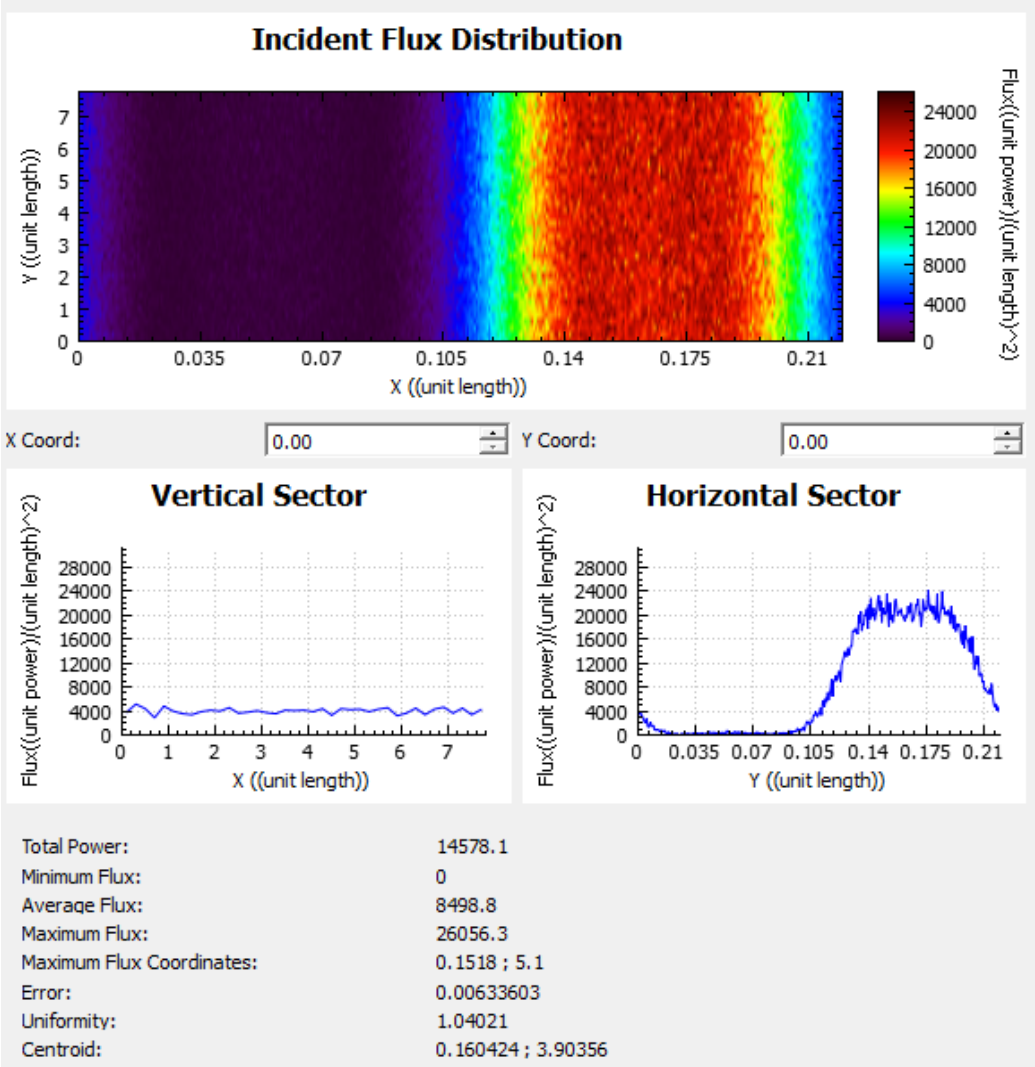

Figure I 4: PTSC module plots for 10^6 rays' view of heat flux of "Run Flux Analysis".

By adding 1 million, the number of rays increases from 10^6 to 10^7. Figure I 5 depicts a comprehensive view of the plots 10^7 rays and heat flux.

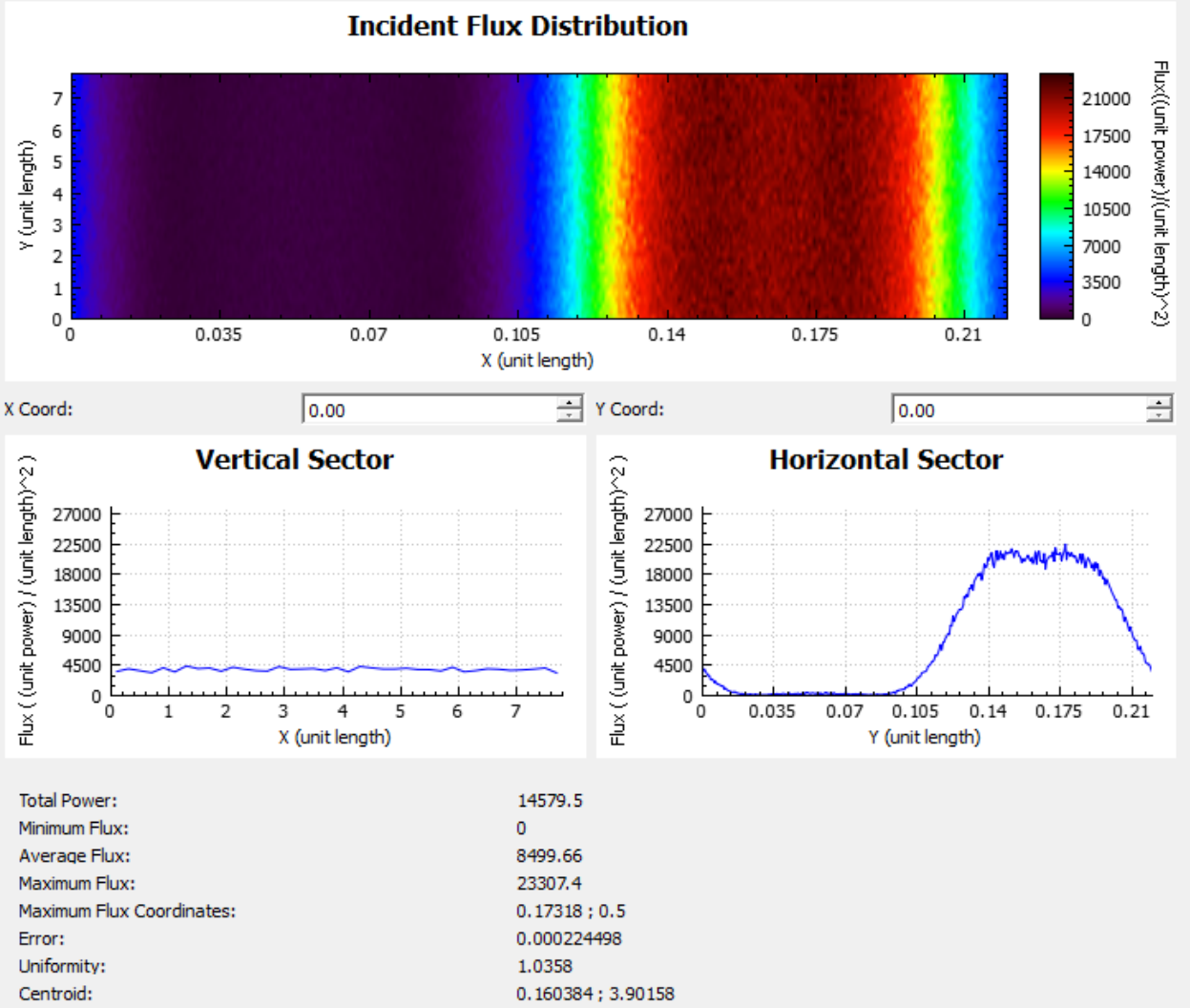

Figure I 5: PTSC module plots for 10^7 rays' view of heat flux of "Run Flux Analysis".

Checked the option of "Append to the previous simulation", for the impact of increasing the number of rays observed by contrasting Figures I 4 and I 5. For 10^7 rays, the plots are smooth "Horizontal Sector", and "Vertical Sector" but not for rays of 10^6. In other words, the heat flow map for 10^7 rays is more precise than for 10^6 rays.

J. Distribution of heat flux over the cross-section of the absorber tube

This section explains the distribution of heat flux in the receiver tube cross-section. An "Isosurface" is first generated. Figure J 1 shows the Results section where "Isosurface" should be included.

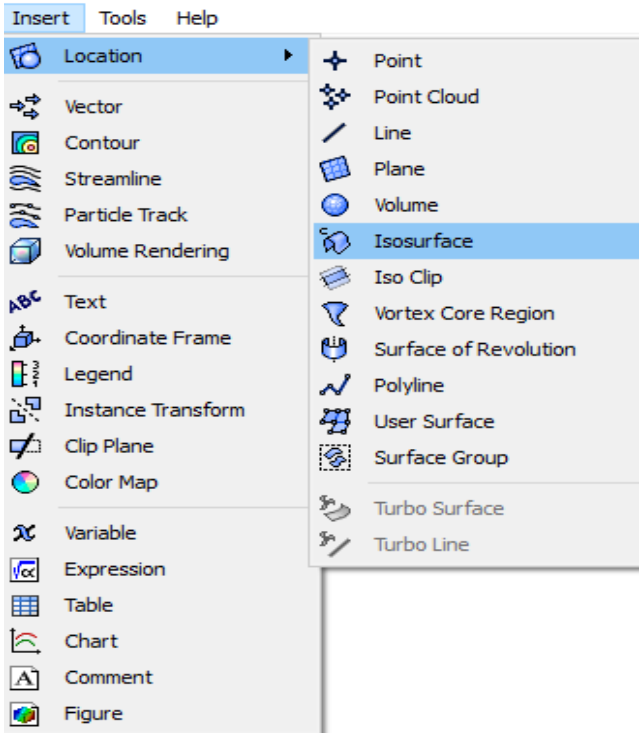

Figure J 1: Creating an “Isosurface”.

Select the variable "Z" for the isosurface. Figure J 2 provides details of the "Isosurface" function.

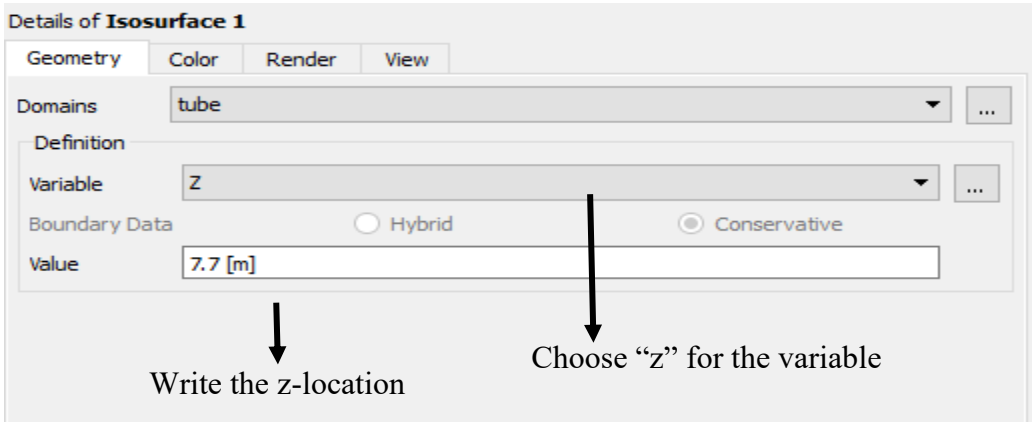

Figure J 2: “Isosurface” details.

Figure J 3 depicts z = 7.7 m of the developed "Isosurface".

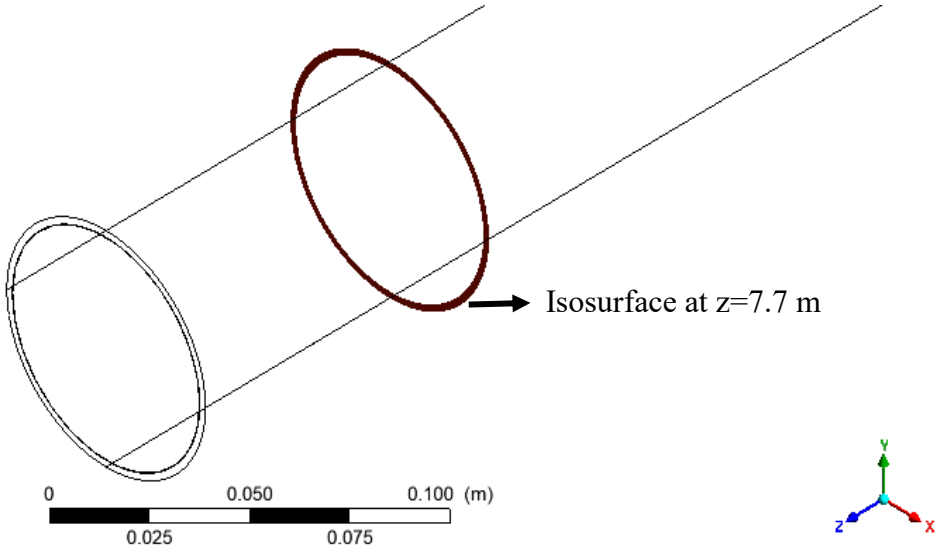

Figure J 3: Cross section at $z = 7.7\ m$ of "Isosurface".

Next, create a "Polyline". Figure J 4 shows the Results section where "Polyline" should be included.

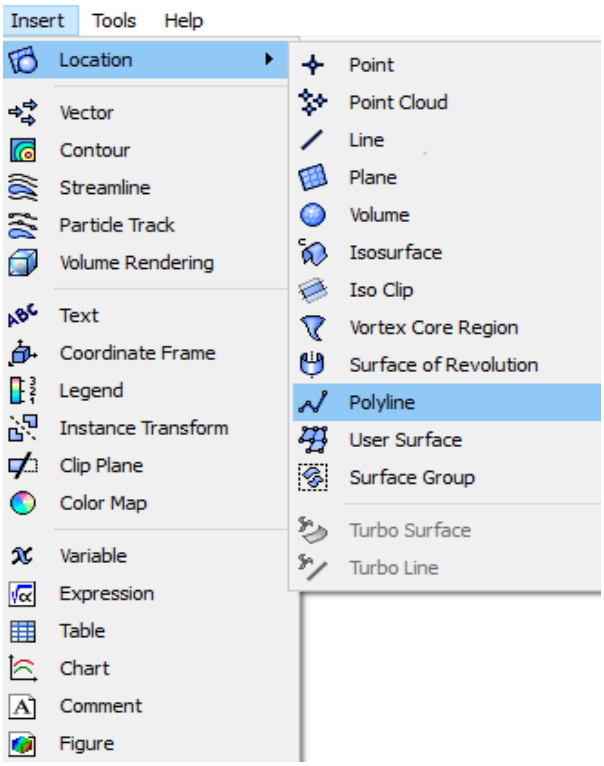

Figure J 4: Polyline insertion.

For this method select "Boundary Intersection". For the Boundary List, pick four of the absorber tube's outside sides. As shown in Figure J 5 the polyline intersects with Select "Isosurface 1". This is the name of the isosurface that was produced in the previous phase.

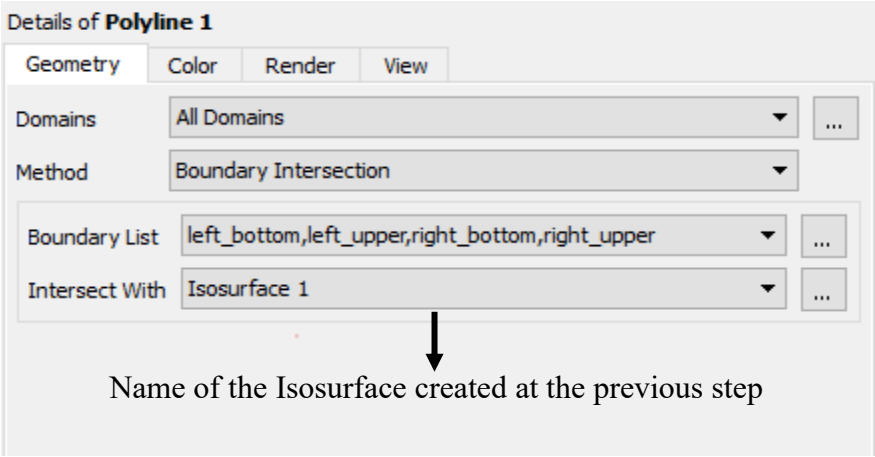

Figure J 5: “Polyline 1” detail section.

It needs to be highlighted that only the bottom surfaces of the tube nearest to the parabolic mirror can be used to estimate the distribution of heat flux.

The produced Polyline and Isosurface are displayed together in Figure J 6. The Polyline, which is depicted as the absorber tube's outer surface cross-section, is the green circular line.

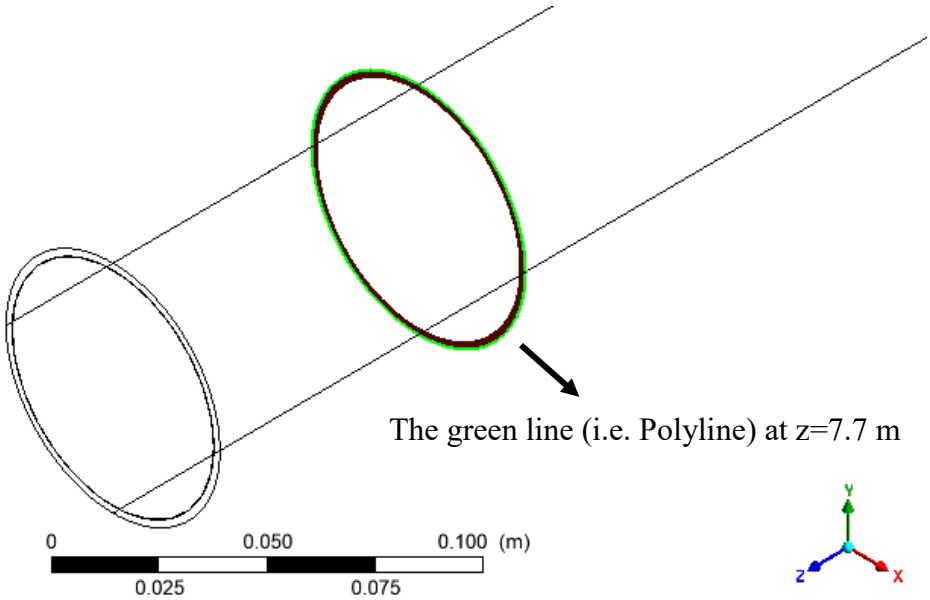

Figure J 6: At the cross-section of z = 7.7 m polyline.

Lastly, by using the "Chart" tool to display the heat flux values on the Polyline, it is possible to determine the heat flux distribution at a certain cross-section. Figure J 7 displays the Results part of the "Chart" section.

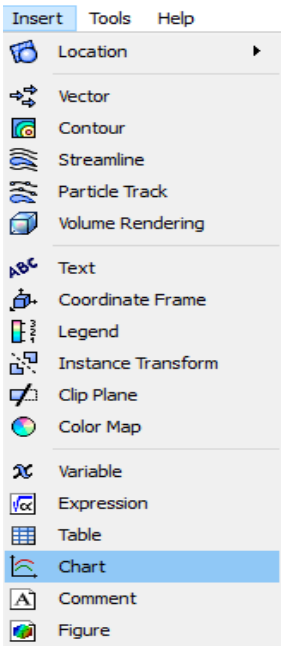

Figure J 7: “Chart” insertion.

For the general type chart select the “XY-Line”. As shown in Figure J 8.

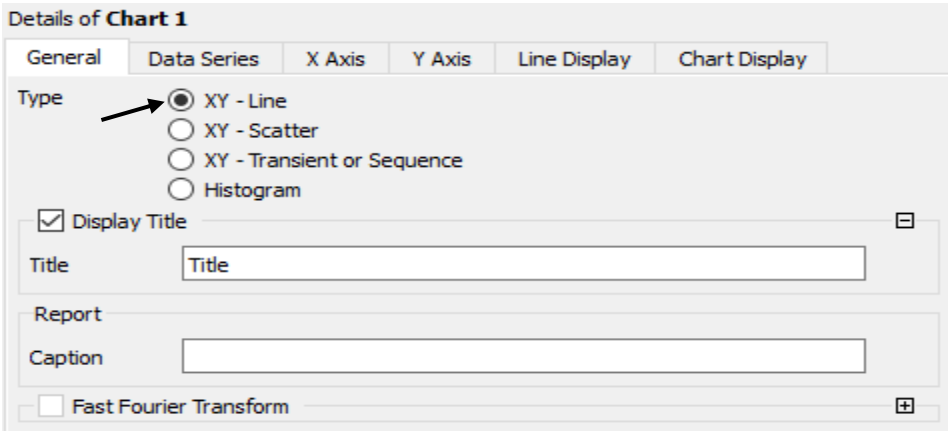

Figure J 8: General tab details of Chart 1.

For Location, choose the Polyline that was constructed in the previous stage. Look at Figure J 9.

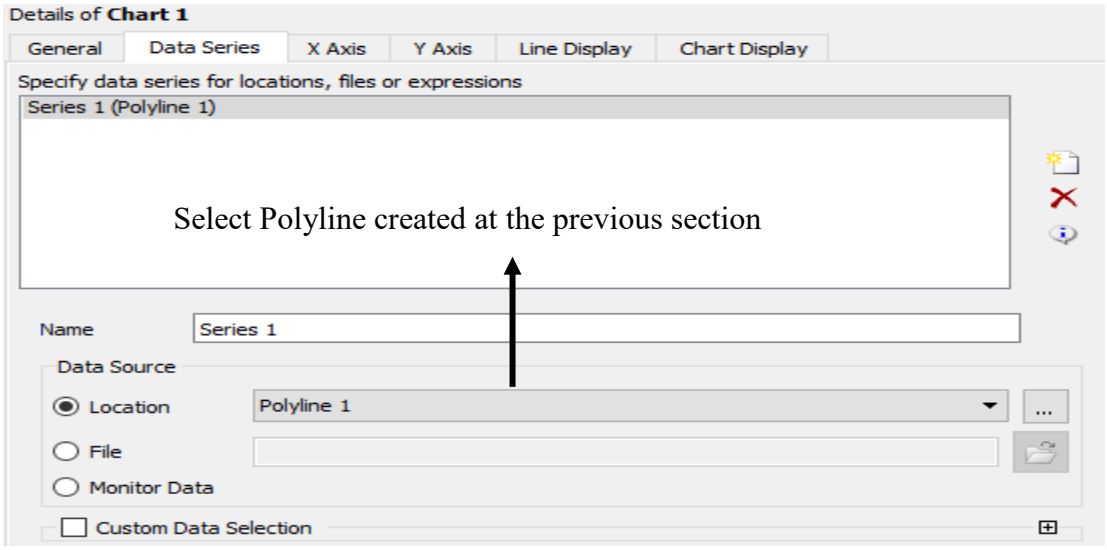

Figure J 9: Data Series chart details for the polyline.

As shown in Figure J 10 for the first parameter select "X".

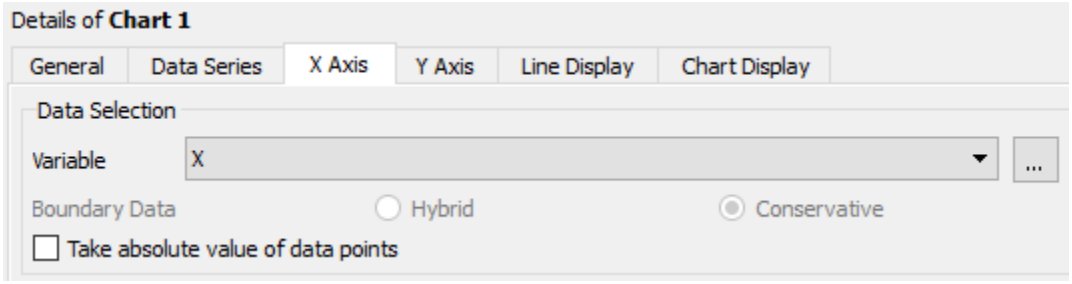

Figure J 10: Select “X” as the X-Axis for details of chart 1.

As shown in Figure J 11 for the second parameter select "wall heat flux".

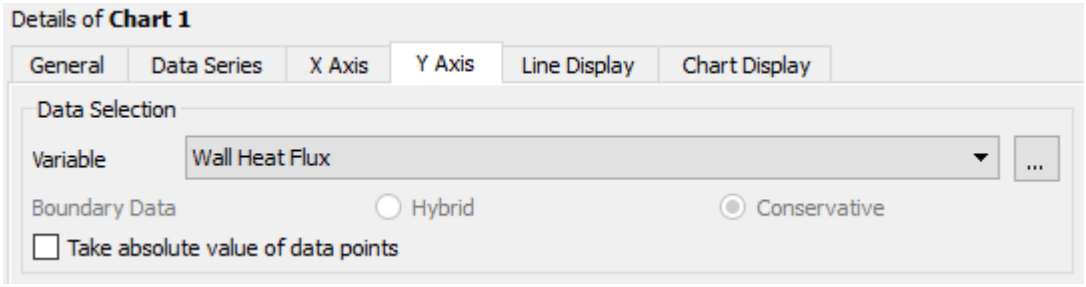

Figure J 11: Select “wall heat flux” as the Y-Axis for details of chart 1.

Once the graph has been obtained, the general pattern is analyzed. The overall sequence is appropriate. To create a more refined figure, export the data and save it as an a.csv file.